Automated Surgical Light Positioning System Using Thermal-imaging and Optical Techniques

by
Jarryd Michiel Burger

Thesis presented in partial fulfilment of the requirements for the degree of Master of Engineering (Mechatronic) in the Faculty of Engineering at Stellenbosch University

Supervisor: Dr Jacobus Hendrik Muller

April 2019

DECLARATION

By submitting this thesis electronically, I declare that the entirety of the work contained therein is my own, original work, that I am the sole author thereof (save to the extent explicitly otherwise stated), that reproduction and publication thereof by Stellenbosch University will not infringe any third party rights and that I have not previously, in its entirety or in part, submitted it for obtaining any qualification.

Date: **April 2019**

UNIVERSITEIT·STELLENBOSCH·UNIVERSITY
jou kennisvennoot • your knowledge partner

Plagiaatverklaring / *Plagiarism Declaration*

1. Plagiaat is die oorneem en gebruik van die idees, materiaal en ander intellektuele eiendom van ander persone asof dit jou eie werk is.
   Plagiarism is the use of ideas, material and other intellectual property of another's work and to present is as my own.

2. Ek erken dat die pleeg van plagiaat 'n strafbare oortreding is aangesien dit 'n vorm van diefstal is.
   I agree that plagiarism is a punishable offence because it constitutes theft.

3. Ek verstaan ook dat direkte vertalings plagiaat is.
   I also understand that direct translations are plagiarism.

4. Dienooreenkomstig is alle aanhalings en bydraes vanuit enige bron (ingesluit die internet) volledig verwys (erken). Ek erken dat die woordelikse aanhaal van teks sonder aanhalingstekens (selfs al word die bron volledig erken) plagiaat is.
   Accordingly, all quotations and contributions from any source whatsoever (including the internet) have been cited fully. I understand that the reproduction of text without quotation marks (even when the source is cited) is plagiarism.

5. Ek verklaar dat die werk in hierdie skryfstuk vervat, behalwe waar anders aangedui, my eie oorspronklike werk is en dat ek dit nie vantevore in die geheel of gedeeltelik ingehandig het vir bepunting in hierdie module/werkstuk of 'n ander module/werkstuk nie.
   I declare that the work contained in this assignment, except otherwise stated, is my original work and that I have not previously (in its entirety or in part) submitted it for grading in this module/assignment or another module/assignment.

17243912 Studentenommer / *Student number*	Handtekening / *Signature*
JM Burger Voorletters en van / *Initials and surname*	**06/03/2019** Datum / *Date*

ABSTRACT

Surgical light systems (SLS) are used to ensure optimal light conditions during surgical procedures. At present, these light sources are adjusted manually by the surgeon or other operating room (OR) personnel. Manual adjustment of the SLS is problematic due to the necessity for a sterile environment. Surgeons must either adjust the SLS themselves, or communicate their requirements so that the OR assistants can position the lights to ensure optimal surgical conditions. Other complications with current SLS include mechanical problems, collisions, inaccessibility and illumination issues. It would be beneficial if the SLS could be automated to illuminate the wound without input from the surgeon. Therefore, the aim of this project was to test whether it is possible to identify a heat source (simulating a surgical wound), track this heat source in real time, and adjust a laser indicator (simulating a surgical light beam) mounted on an articulating assembly (analogous to an SLS).

A system was developed that used an algorithm that identified and tracked a heat source and communicated to an automated articulating assembly to keep the laser indicator pointed at the heat source. The heat source was identified using thermal cameras and tracked using stereo optical cameras in three-dimensional space. The tracking accuracy and the manipulation accuracy were tested, and the results demonstrated that the combination of optical and thermal cameras with stereo image-processing techniques could be used to identify and track a heat source. This could further be used to guide an articulated assembly to keep a light beam pointed at the heat source with good accuracy. Therefore, this technology will contribute towards achieving full automation of SLS in the future. Following from the conclusions of this thesis, aspects have been identified and recommended for future research to achieve full automation and solve all SLS complications in the future.

OPSOMMING

Chirurgiese ligstelsels (CLS'e) word gebruik om optimale ligtoestande tydens chirurgiese prosedures te verseker. Tans word dit deur die chirurg of ander personeel in die operasiesaal (OS) verstel. Om die CLS met die hand te verstel, is problematies weens die vereistes van 'n steriele omgewing. Chirurge wat nie die CLS self verstel nie, moet hul vereistes so kommunikeer sodat die verstelling deur die OS-assistente voldoende is om optimale chirurgiese omstandighede te verseker. Ander komplikasies met die huidige CLS sluit in: meganiese probleme, botsings, ontoeganklikheid en beligtingskwessies. Dit sal dus voordelig wees as die CLS geoutomatiseer kan word om die wond te verlig sonder insette van die chirurg. Die doel van hierdie projek was dus om te toets of dit moontlik is om 'n hittebron (wat die chirurgiese wond voorstel) te identifiseer, hierdie hittebron te volg en 'n laseraanwyser (simulasie van die chirurgiese ligstraal) aan te pas met 'n ge-artikulerende arm (voorstelling van 'n CLS).

'n Stelsel is ontwikkel wat 'n algoritme gebruik om 'n hittebron te identifiseer en te volg. Die inligting is dan oorgedra na 'n gemotoriseerde artikulerende arm, om die laseraanwyser na die hittebron te rig. Termiese kameras het die hittebron geïdentifiseer terwyl stereo-optiese kameras gebruik is om die hittebron te volg soos wat dit beweeg het. Die akkuraatheid van die arm se beheer is getoets en die resultate het getoon dat die kombinasie van optiese en termiese kameras met stereobeeld-verwerkingstegnieke gebruik kan word om 'n hittebron te identifiseer en te volg. Dit kan verder gebruik word om 'n artikulerende arm aan te pas om 'n ligstraal te rig na die hittebron, met voldoende akkuraatheid. As gevolg van die akkuraatheid sal hierdie tegnologie in die toekoms bydra tot die volle outomatisering van CLS. Na aanleiding van die gevolgtrekkings van hierdie tesis, is daar sekere aspekte geïdentifiseer en aanbevelings gemaak vir toekomstige navorsing om volle outomatisering te bereik en alle SLS-komplikasies in die toekoms op te los.

ACKNOWLEDGEMENTS

I wish to express my sincere gratitude and appreciation to the following individuals and institutions:

Dr J.H. Muller, for acting as supervisor, and for his guidance and advice;

Dr S. Erasmus, for background information and allowing me to observe him during his surgical procedures;

Dr J. Joubert for allowing me to observe him during his surgical procedures;

Dr C.E. Basson, for insightful advice on how to present my work;

Mr C. Visser, for assistance with and advice on technical matters;

Lab colleagues, for discussions and the occasional help;

My family and friends, for their prayers, support, advice and encouragement;

Mediclinic Stellenbosch, for financial support;

Most importantly, my Lord and Saviour Jesus Christ, for all things have been created through Him and for Him.

Table of contents

List of figures

Page

List of tables

Page

Nomenclature

Abbreviations

2D	Two-dimensional
3D	Three-dimensional
AOA	Angle of arrival
BUT	Button
CCD	Charge-coupled device
DOF	Degrees of freedom
EM	Electromagnetic
GPS	Global positioning system
HEPA	High efficiency particulate absorbing
HSV	Hue, saturation and value
IMU	Inertial motion unit
LDS	Laminar downflow system
LA	Light adjustment
LED	Light-emitting diode
OS	Operating system
OR	Operation Room
PID	Proportional integral derivative
PWM	Pulse-width modulation
RC	Radio control
RF	Radio frequency
RFID	Radio frequency identification
RSS	Receiver signal strength
RGB	Red, green and blue
SLS	Surgical lighting system
TOA	Time of arrival
UWB	Ultrawide band

Notations

Θ	Light beam angle relative to surgical wound
b	Baseline
ƒ	Focal length
h	Height of SLS surrogate above workspace
C	Camera centre
F	Fundamental matrix
K	Calibration matrix
P	Camera projection matrix
R	Rotation matrix
X	Matrix
X_c , Y_c , Z_c	Camera axis
X_{image} , Y_{image}	Image axis
X_w , Y_w , Z_w	World axis
$X_c = [X_c , Y_c , Z_c]^T$	Point in camera coordinates
$P = \left[P_x , P_y\right]^T$	Principle point
$X_{image} = \left[X_{image} , Y_{image}\right]^T$	Point in image coordinates
$X_L = [X_L , Y_L]^T$	Point in image coordinates in left image
$X_R = [X_R , Y_R]^T$	Point in image coordinates in right image
$X_w = [X_w , Y_w , Z_w]^T$	Point in world coordinates

1 INTRODUCTION

1.1 Background

Today, operating rooms (ORs) are highly technical and complex working environments that contain many different types of apparatus, such as overhead lights, viewing screens and monitors. Light conditions are of paramount importance during surgery. Theatre lights or surgical light systems (SLSs) are used by OR personnel during surgical procedures and have been designed to illuminate, with high-intensity light, the area of interest [1]. This reduces shadows made by the heads and hands of the OR personnel. Other important aspects for an SLS include the quality and colour released by the light. These aspects are important for surgeons to perform visual tasks [2]. The SLS is designed to allow for great manoeuvrability to position it as required, which is currently done by hand using handles in the middle of the surgical light and handles that are situated around the surgical light. An illustration of a typical SLS can be seen in Figure 1. To maintain a sterile environment, surgeons are limited to using the central handle, while other OR personnel, like surgeon assistants, are limited to using those on the periphery.

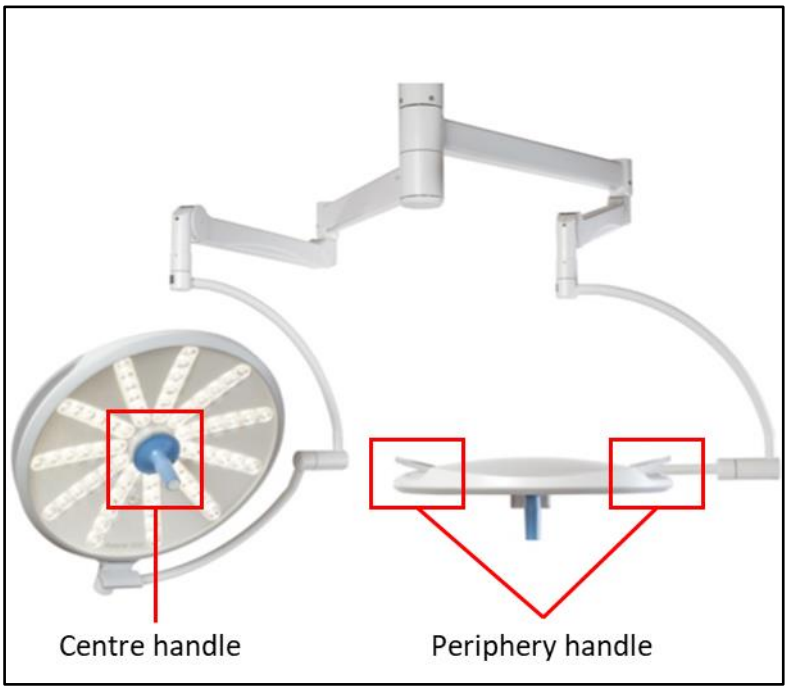

Figure 1: Example of the surgical light system in an OR [3]

Current OR SLSs make use of light-emitting diode (LED) lights instead of the old halogen light technology [2]. The advantage of LED lights is that they are energy efficient, meaning they consume a fraction of energy compared to other light sources such as incandescent, fluorescent or halogen lights. Other advantages include much greater durability and lifespan, and reduced heat emission [4].

Adjusting the SLS is often problematic due to the necessity for a sterile environment, so that surgeons must either adjust the SLS themselves (using only the central handle), or have to communicate their requirements regularly so that the OR assistants can position the lights to their satisfaction (using the peripheral handles). Other complications with current SLSs include:

- Mechanical problems – The excessive force required to move the SLS makes a one-hand light adjustment (LA) impossible and occasionally causes the SLS to seize. Therefore, surgeons may require help from other OR medical personnel, which can delay the completion of the LA [1]. A total of 44% of surgeons have reported difficulty when SLS arms became entangled, and 25% had difficulty with one-hand light adjustments [5].

- Collisions – At times, the SLS will collide with other OR equipment and against the heads of the OR medical personnel [1]. Fifty-five percent of surgeons had difficulty with SLS arms colliding with other OR equipment or with the medical personnel's heads [5].

- SLS inaccessibility - At times, surgeons had to stand up or move to perform an LA because the SLS was inaccessible/out of reach [1].

- SLS illumination issues - 71% of the surgeons had difficulties using the SLS during procedures, and 45% had difficulty with wound illumination during procedures (the wound was not well lit). Of all the instances of LA, 97% was attributed to repositioning the SLS, while the rest included refocusing the light beam or increasing illumination levels [5].

SLS lights have improved greatly over the years, with many competing companies manufacturing them. Development mostly entails the improvement of the light quality in terms of illumination strength, brightness and colour [6]. Not much of the development and research that has been published has focused on automated SLS [6, 7]. However, a few patents on automated SLS suggest that there is an interest in this field [8].

In this thesis, a tracking methodology is tested based on its ability to track a heat source (simulating an open wound) by using stereo and thermal vision principles. This is demonstrated on a surrogate model of an SLS. Stereo vision thermal and optical tracking are used to track the heat source and automatically adjust the surrogate SLS model. If this can be achieved, not only will most of the

complications and risks be overcome, but time spent in the OR can be optimised without interruptions due to LA.

1.2 Motivation

Current manual SLSs have limitations and complications. Surgeons perform 45% of all the LAs during a procedure, and 97% of these LAs interrupt the complex surgical workflow. The other 55% are done by OR medical personnel, of which 33% of the LAs interrupted their surgical tasks during the procedure [1]. Surgeons' assistants or other OR personnel can help perform LA, but this is often not ideal, since there is limited room in the workspace and communication can be challenging [7]. This is demonstrated by a report that 22% of LAs take more than double the average time (eight seconds) due to LA complications [1].

There is a great need to reduce the current complications and risks caused by manual SLS operation. Therefore, if the repositioning of the SLS can be done automatically using tracking technology, the complications highlighted above will be addressed and there would also be additional benefits. Benefits include:

- Improved hygiene: The risk of coming into contact with non-sterile surfaces will be mitigated by automating SLS [7].

- Theatre time and cost savings: It is estimated that one hour in surgical operation costs around R14 000 [9]. Automated SLS reduces time spent on adjustments [1], which would save on costs over time.

- Workflow optimisation: Automated SLS removes the need to interrupt a complicated workflow [1, 5, 7].

Although this project will be advantageous for surgeons, patients and hospitals will also benefit. Patients will benefit by having to endure shorter in-theatre time and therefore will face a reduced risk of infection. Hospitals will benefit by having a higher throughput in theatres. This thesis focuses exclusively on the movement of an SLS to achieve completely hands-free automation.

1.3 Objectives

The aim of this project was to test whether it is possible to identify a single heat source in the field of view (FOV) and to track this heat source in real time in order to automatically adjust a laser indicator mounted on an articulating assembly that is analogous to that of an SLS. The heat source was identified using thermal cameras, while the tracking was assisted by stereo optical cameras.

The following were the main objectives identified to achieve the project's aim:

1. Design an algorithm in which thermal imaging can be used to identify a single heat source and incorporate this into optical stereo vision to track a single heat source in three-dimensional (3D) space.

2. Design a scaled-down mechanical system (SLS surrogate) that is analogous to the articulating arms of a standard SLS.

3. Design a closed loop control system that integrates the algorithm design and the SLS surrogate. This control system must manipulate the actuators mounted on the SLS surrogate to enable target tracking of the heat source from the information received by the algorithm.

The expected outcome of this project is a working SLS surrogate that uses thermal imaging and optical stereo vision technology to accurately track a heat source and automatically adjust the SLS surrogate accordingly.

2 LITERATURE STUDY

The aim of this literature study is to discuss wound characteristics and existing SLSs that are relevant to this study. It also provides background information on camera technology (digital, infrared and thermal), on thermal technology, and on image processing, mainly relating to object tracking through computer vision, stereo vision and thermal stereo vision. Lastly, current solutions found in the literature will be discussed. This background information aided the decision making throughout this study.

2.1 Wound characteristics

Wound characteristics found during operations are widely varying and, because only a number of orthopaedic procedures could be observed, only the wound characteristics of orthopaedic procedures were considered for this project.

2.1.1 Common orthopaedic surgical procedures

Some of the most common orthopaedic surgical procedures include arthroscopy, soft tissue repair, total joint replacement, revision joint surgery and bone fracture repair. Arthroscopy is a surgical procedure that makes use of an arthroscope that is inserted into the problematic joint to remove damaged material such as cartilage fragments and/or calcium crystals. The aim of an arthroscopic surgical procedure is to eliminate interference within the joint and to minimise inflammation of the synovial membrane [10]. Soft tissue repair surgeries are mainly procedures aimed to strengthen joint stability. This is done by surgically repairing or reconstructing tendons, ligaments and muscles. Soft tissue surgeries can be achieved either through open or arthroscopic surgical procedures [11]. Total joint replacement (TJR) is the replacement of a natural synovial joint (e.g. hip, knee, etc.) with a new prosthetic joint through arthroplasty surgery. TJR procedures aim to relieve pain and improve joint mobility. Revision joint surgery is a procedure that replaces an old prosthetic joint with a new prosthetic joint [12]. Not all bone fractures require surgery, but surgery is required in the case of severe bone fractures like comminute fractures (bone shattering). With these types of surgeries, the bone fracture is repaired by adding either an external or internal fixation to realign the fractured bone while the bone heals. The difference between external and internal fixation is that the screws, pins and metal plate used to align the fractured bone are attached outside the skin (visible) or attached directly to the bone (not visible) [13].

2.1.2 Wound (incision) size

In this project, wound size refers to the size of the skin incision the surgeon makes during a surgical procedure. Depending on the type of orthopaedic procedure, the wound size required can range vastly. Therefore, only soft tissue repair and total joint replacement procedures were considered in this project. Arthroscopy, revision joint surgery and bone fracture repair procedures were not considered as viable procedures, because only keyhole skin incisions ($\leq$ 2 cm) are used in arthroscopy, and the incision size depends greatly on the severity of the injury in the case of revision joint surgery and bone fracture repair [10].

The table below summarises the mean wound sizes of the different surgical procedures considered in this project. These wound sizes were either observed or found in the literature. Most of these procedures are open surgery procedures, with the exception of hip replacement surgery. This is a minimally invasive surgery. Minimally invasive surgery is a favoured technique used by surgeons that results in a reduced wound size and assists in accelerated patient recovery [14]. This was also the type of hip replacement procedure that Dr Jan Joubert performed during the observation. With knee replacements, the wound size can be up 20 cm long, depending on the surgeon preforming the procedure. It is important to note that, because wound size can vary tremendously depending on the severity of the injury, only mean wound sizes were considered for the data.

Table 1: Wound sizes of different orthopaedic procedures

Orthopaedic procedure	Mean wound size
Soft tissue repair	
ACL reconstruction [15, 16]	3.3-4 cm
MCL reconstruction [17]	3 cm
Rotator cuff tear [18, 19]	5 cm
Achilles tendon rupture [20, 21]	9.5 cm
Distal clavicle excision [22, 23]	2-3 cm
Total joint replacement	
Hip replacement [14, 24, 25]	6-10 cm
Knee replacement [26, 27]	10.3-10.5 cm

2.1.3 Wound identification through computer vision

A thermal camera was used to identify the surgical wound. By combining a calibrated thermal image and a colour classification algorithm it is possible to track a desired object by its thermal radiation. The better the thermal resolution of the thermal camera, the smaller the temperature range that can be tracked.

There are numerous heat sources and other objects in the theatre that can have the same temperature as a surgical wound, and it is therefore crucial to combine colour classification algorithm with other identification algorithms. Two possible approaches are found in the literature that can be combined with thermal identification to accurately identify and track the surgical wound.

The first approach found in the literature makes use of an integrated tracking model that takes both texture and edge information into account when tracking a desired object in real time. These models are found to be accurate and robust to occlusions and textured backgrounds [28, 29]. The results of this method can be seen in Figure 2. Another approach used in the literature also makes use of an integrated tracking model, but takes texture and colour information into account when tracking a desired object in real time. These models are also found to be robust to complex backgrounds with similar targets and to textured backgrounds [30, 31]. The result of this method can be seen in Figure 3.

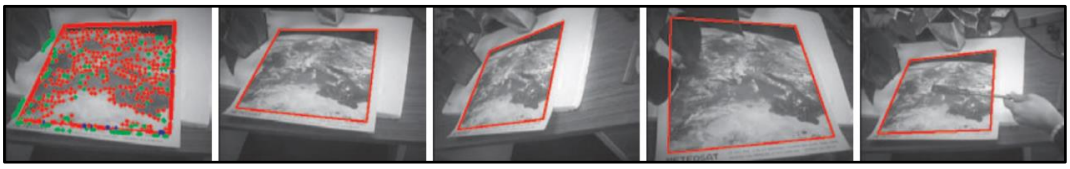

Figure 2: The integrating texture and silhouette (edge) base information model [29]

Figure 3: The integrating texture and colour base information model [31]

By combining any two of the above-mentioned approaches with thermal identification, wound identification and tracking can be achieved by computer vision in real time. Although this was not tested in this project, the focus was on tracking a single heat source in 3D space in order to identify it using the thermal cameras and to combine this with optical stereo vision to find the world coordinates of the heat source to adjust an articulating assembly accordingly.

2.2 Current surgical light systems

2.2.1 Current SLS used

Light conditions are of paramount importance during surgery. SLSs are used by orthopaedic surgeons during surgical procedures and have been designed to illuminate, with high-intensity lights, the area of interest [1]. SLS heads are designed in a dome shape to increase light intensity in order to reduce the shadows caused mainly by the hands of the orthopaedic surgeons at work [2]. In selecting SLSs for ORs, hospitals prefer to use smaller SLSs to reduce heat production and disruptions in laminar flow [2, 32]. SLSs come in many shapes and sizes, and Mr J. Herbert, a group procurement executive at Mediclinic South Africa [6], suggested considering the following SLSs: An HLED (Maquet, Orleans, France), an LED 5/LED 3 (Dr Mach, Ebersberg, Germany), a VOLISTA (Maquet, Orleans, France), a Luvis L200 (Dentis, Daegu, Korea) and a Polaris 600 (Drager, Lübeck, Germany). Table 2 highlights the importance of these SLSs. The HLED was measured physically and the size and dimensions of an LED 5/LED 3 light were found in a catalogue [33]. The other important technical data on the VOLISTA, Luvis L200 and Polaris 600 was also found in catalogues.

Table 2: Current SLSs used in ORs

Type of surgical light	Arm dimensions	Head dimensions	Light field size	Depth of illumination
Dr Mach – LED 5/LED 3 [33]	**Arm 1:** 1 000 mm **Arm 2:** 910 mm	**Length:** 720 mm **Breath:** 720 mm **Height:** 860 mm	**Diameter:** 200–320 mm	600–1 500 mm
Maquet – HLED 500 [34] (measured)	**Arm 1:** 900 mm **Arm 2:** 800 mm	**Length:** 700 mm **Breath:** 700 mm **Height:** 750 mm	**Diameter:** 240 mm	700–1 200 mm
Maquet – VOLISTA [35]	**None**	**None**	**Diameter:** 200–250 mm	500–1 000 mm
DENTIS - Luvis L200 [36]	**None**	**None**	**Diameter:** 200–300 mm	850–1 500 mm
Drager Polaris 600 [37]	**None**	**None**	**Diameter:** 190–280 mm	700–1 300 mm

2.2.2 Consultation and observation of the use of current SLSs

To further understand the current use of SLSs, an orthopaedic surgeon, Dr Spike Erasmus (a knee specialist [38]), was consulted and observed during three knee replacement operations and an ACL (anterior cruciate ligament) and MCL (medial collateral ligament) reconstruction operation. In addition, a hip replacement operation performed by Dr Jan Joubert (a hip specialist [39]) was observed. An example of these observation surveys used can be seen in Appendix B.1, and a photograph of one of the procedures can be seen in Figure 4. The outcome of this

investigation and what was found in the literature (discussed in section 1) are summarised in Table 3. Based on the consultation and surveys, the most important requirement found was that an LA should be performed quickly, since there can be as many as 17 LAs per procedure. Secondly, it was found that LAs must be performed after the wound has been adjusted or the light beam has been obstructed. Furthermore, it is important not to burden the surgeons with more equipment, since they already wear and use numerous pieces of equipment (see Figure 4).

Table 3: Summary of the literature and findings from the observations

	Literature	Observation
Time taken	78% took 8 seconds [1] 22% took > 8 seconds [1]	2-15 seconds, commonly ~6 seconds
Types of LA	30% rotation only [1] 4% translation only [1] 66% combination [1]	41% rotation only 24% translation only 35% combination
Complications (experienced by surgeons)	entangled SLS (63%) [5] badly lit wounds (64%) [5] one-handed LAs not possible (36%) [5] collisions (78%) [5] out of reach (71%) [5] workflow disruption [1, 5, 7]	collisions with OR equipment lack of mobility (high mechanical forces)
Assistance	surgeon performed 45% of the LAs [5]	surgeon performed 68% of the LAs

Hygiene is a key consideration because of the risk that surgeons could touch non-sterile parts of the SLS [7, 40]. Deep surgical wounds are particularly difficult to illuminate, thus surgeons have to perform LAs frequently [1].

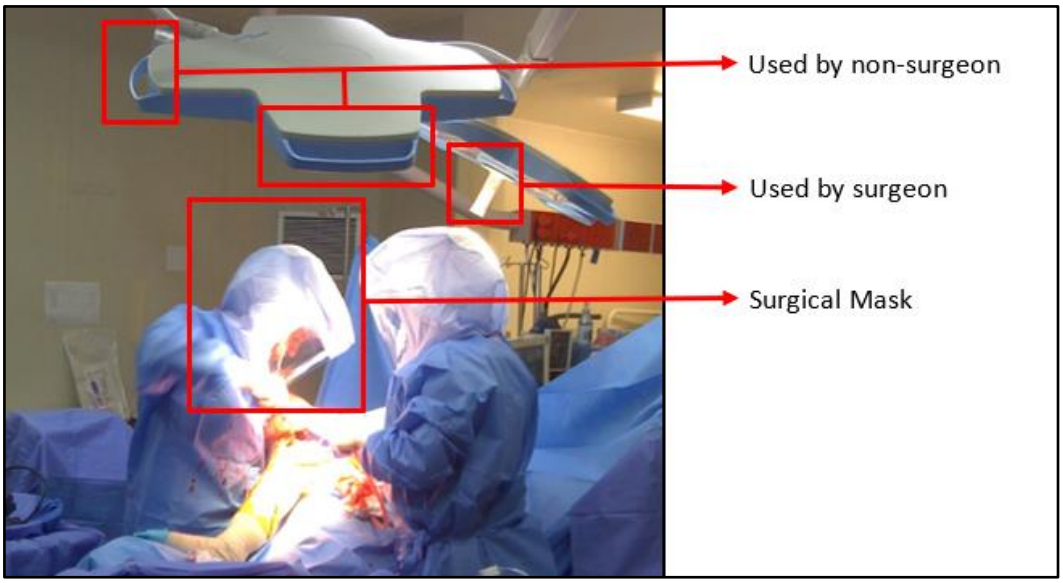

Figure 4: In-theatre knee replacement operation done by Dr Spike Erasmus showing the equipment worn by surgeons and the SLS (with handles indicated)

2.3 Camera technology

2.3.1 Digital optical camera

Digital optical cameras take light and focus it through lenses onto a sensor that consists of a grid of tiny pixels that are sensitive to light [41]. The greater the number of pixels, the greater the resolution of the image will be. The resolution is calculated using the width and height of an image. For example, if the resolution of an image is 1 080 x 1 600, it means that the image is 1 080 pixels wide and 1 600 pixels high, or vice versa, with a total number of 1 728 000 pixels or 1.7 megapixels [42].

Digital cameras can capture more of the electromagnetic (EM) spectrum than the human eye, especially in the near infrared (IR) region (0.75 to 4 µm wavelength, Figure 8). Digital cameras usually make use of a colour-filtered lens to block out any IR in order to create a clearer and sharper image with realistic colour. Therefore, an image taken by an optical camera in sunlight (without an IR-exclusion filter) will represent significant amounts of infrared light [43].

2.3.2 IR illumination camera

IR illumination cameras function much like digital cameras, but without an infrared filter, therefore allowing both IR and visible light to be captured by the camera. IR illumination cameras are mostly used in surveillance applications, since this camera can operate in daylight and at night, without the aid of visible light to illuminate the field of view at night. IR illumination cameras use IR to illuminate the field of view at night, and this is invisible to the human eye [44]. The image in Figure 5 shows the difference between images taken by cameras with and without IR illumination.

Figure 5: The effect of IR illumination on an image [45]

There are three main types of IR illumination methods. The first is an incandescent lamp covered with an infrared filter; this method is less common because it generates a lot of heat and uses a substantial amount of power. The second method is more common and makes use of infrared LEDs to illuminate the camera's field of view; this method is used when flooded infrared light is required at shorter distances. The third method is also fairly common and makes use of infrared laser diodes; this method produces less infrared light, but the light can be concentrated more to illuminate at greater distances [44].

2.3.3 Thermal camera

Thermal IR cameras work differently from standard colour cameras since they use special types of lenses that allow IR to pass through. Thermal IR cameras focus the thermal/infrared radiation emitted by all the objects within the field of view onto an IR detector. This detector measures very small temperature changes and converts invisible heat patterns into visible images that can be seen through a viewfinder or monitor. This visible image is known as a thermal image. Thermal cameras cannot pick up heat signatures through walls, glass or any other solid objects; they can only pick up heat that has been transferred to the surface of an object [46].

Thermal camera technology has changed over the last 30 years, especially with respect to the thermal camera's detector and the number of elements that can be detected. The detectors of the first thermal cameras could only detect a single pixel at a time and needed a 2D mechanical scanner to generate a two-dimensional thermal image. Currently, thermal cameras contain 2D array detectors that require no mechanical scanner to generate a 2D thermal image [46].

Thermal cameras do not use normal glass lenses, but rather special lenses made either of germanium (Ge), chalcogenide glass, zinc selenide (ZnSe) or zinc sulphide (ZnS). The reason for using these materials is that they transmit IR in the wavelength range of 8 to 15 µm [47]. These types of lenses, as well as the sensor required by thermal cameras, makes these cameras expensive compared to standard optical cameras.

2.3.4 Combining thermal and optical cameras

FLIR is a company known for producing and selling thermal cameras. This company has patented a technological feature known as Multi-Spectral Dynamic Imaging (MSX). This feature combines a thermal image with an optical image to enhance the details of the thermal image in real time (see Figure 6) [48]. Therefore, most FLIR cameras will have a thermal and an optical camera side by side. Figure 7 demonstrates this side-by-side camera setup. This is also the camera that was used in the research done for this thesis.

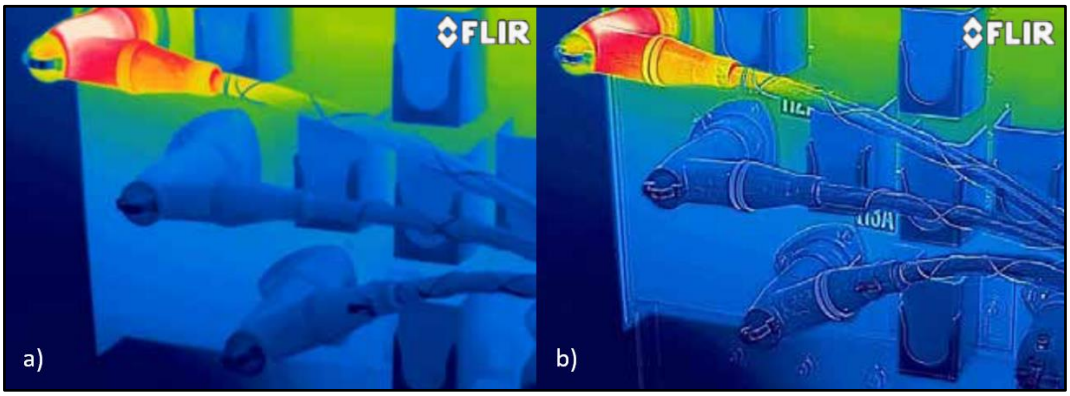

Figure 6: a) Normal thermal image and b) MSX enhanced thermal image [48]

Figure 7: FlirOne Gen 2 thermal camera [49]

2.4 Infrared technology

2.4.1 Infrared radiation

Radiation that is visible to the human eye includes EM waves within the 0.4 to 0.75 µm wavelength band (Figure 8). Infrared (IR) wavelengths span 0.75 µm to 1 000 µm on the electromagnetic spectrum [50]. The light frequency of IR is higher than that of visible light and consequently is not visible to the human eye [44].

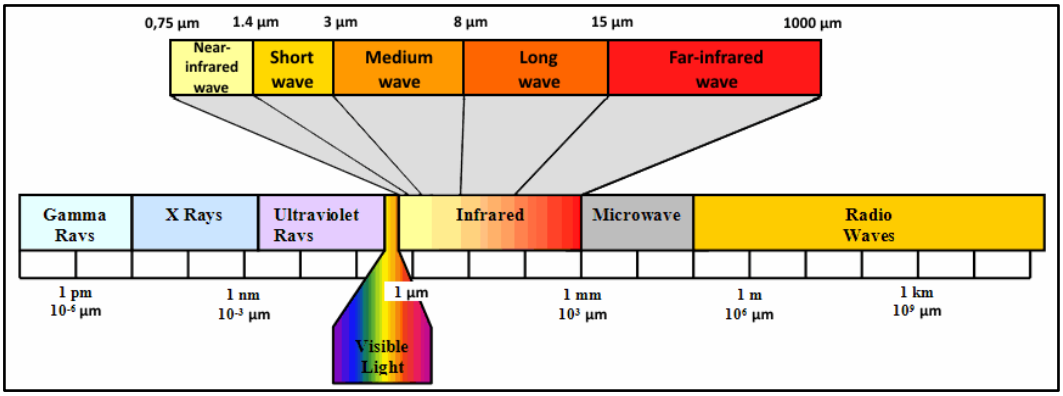

Figure 8: Electromagnetic spectrum with visible light and infrared radiation [50]

The intensity of the IR emitted by an object depends on its temperature. The higher the temperature, the greater the IR emitted. The spectral radiance is the amount of IR radiated from the surface of the object per unit wavelength. Figure 9 demonstrates the increase in spectral radiance with an increase in temperature [50].

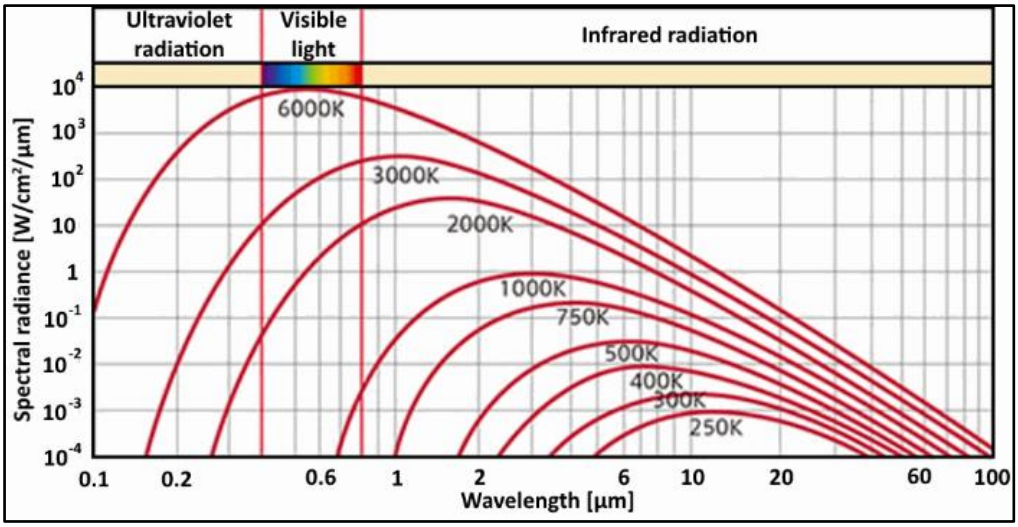

Figure 9: Spectral radiance emitted per increase in temperature [50]

2.4.2 Thermal radiation

Radiation is energy emitted by matter through EM waves caused by the changes in the electron configurations of the atom/molecules. Thermal radiation is heat transferred by EM radiation, with wavelengths spanning 0.1 µm to 100 µm on the electromagnetic spectrum (Figure 8). The transfer of heat caused by radiation is extremely fast and requires no intervening substance. Thermal radiation is a form of radiation emitted by a heat source because of its temperature. All matter with a temperature above absolute zero emits thermal radiation. This matter includes all solids, liquids and gases that either emit, transmit and/or receive radiation to some extent [51].

2.4.3 Thermal imaging

Thermal imaging depicts the heat signature emitted by any object and can be presented as still images or videos. Since all matter that has a temperature greater than absolute zero emits thermal radiation, it is possible to view an environment using IR without the need for visible light (Figure 10).

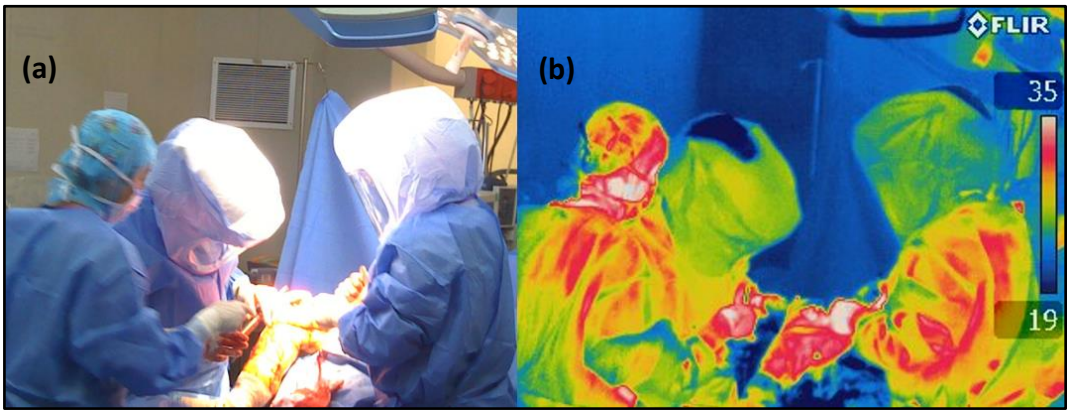

Figure 10: In-theatre knee replacement done by Dr Spike Erasmus. Digital (a) and thermal (b) images of the same view

In a thermal image, the different colours showcase a map of the temperatures based on the temperature range. The colours in a calibrated thermal image can be assigned to a specific temperature and therefore display the different temperatures in the thermal image. The temperature legend in a thermal image is a colour map that corresponds to the number of colours used to visualise different temperatures. There are many kinds of colour maps, for example the standard 16-colour map (Figure 10b), the grey-scale colour map and the red-green-blue colour map.

2.5 Image processing

Image processing is a method used to extract information from or enhance digital images. This method can be used to identify objects within images and to track these objects within video sequences (object tracking). It can also be used to construct a 3D environment from two or more two-dimensional (2D) views of the same environment (stereo vision). Image processing can be highly accurate, but can be expensive because of the camera used and can have a high computational load depending on image complexity [52].

2.5.1 Object tracking through computer vision

An object can be any entity of interest that requires tracking and is defined by its shape and size [53]. Object tracking through computer vision entails following the path of an object in a video sequence by detecting its position within this video sequence (frame by frame) in real time [54]. There are three basic steps used in the literature to describe object tracking in a video sequence using image processing. These steps are object detection, object classification and object tracking.

Object detection

The goal of object detection is to identify objects in motion and bundle pixels of these objects. Since motion within a video sequence is typically the main source of information, the initial focus is on identifying these objects in motion [55]. The identified region within the frame is known as the detection region. Three commonly used methods to detect objects are summarised in Table 4 below.

Table 4: Comparing the different object-detecting methods [55]

Methods	Accuracy	Computational time
Frame differencing	Moderate	Moderate
Optical flow	Low-moderate	High
Background subtraction	High	Low-moderate

Frame differencing

Frame differencing uses the difference of one frame from another, consecutive frame to detect the objects in motion [53]. To implement this method, the calculation is considerably less complicated than the optical flow method and it can therefore be used for real-time applications [55]. The method is very adaptive and can be implemented in various environments, but the limitation is that the complete shape of the object is difficult to detect, making the method inaccurate [53].

Optical flow

Optical flow is a method that uses vectors to estimate motion within a video by pairing identical points on objects from frame to frame. These vectors describe the velocity of the pixels in motion in a video [53]. This optical flow method distinguishes moving objects from the background within a video sequence, as well as describes the full movement information of these objects. This method requires large computational capability and is very sensitive to noise, therefore it is not suitable for real-time applications [55].

Background subtraction

Background subtraction detects objects in motion by finding the difference between the current frame and the background frame or reference frame in a video sequence. Background subtraction can use recursive or non-recursive techniques [53]. Firstly, background modelling must be done to yield the reference model, but also must be sensitive enough to recognise moving objects. In background subtraction, the reference model is compared to the current frame to detect any differences between the frames, and these differences are objects in motion [55].

Non-recursive techniques store a buffer of video frames and use this buffer to estimate the background image, while recursive techniques do not use this stored buffer but rather recursively update the estimated background image from the previous input frames. The non-recursive method is highly adaptive, but requires storage space that varies depending on the buffer size. Using the recursive technique, the background model can be susceptible to error caused by a bad estimation of the background image [55].

Object classification

Once the various objects in motion (detection regions) have been identified, the objects need to be classified [55]. Objects have unique visual features, including their shape, texture, colour and motion. These unique features are ideal for identifying specific objects and can be used to classify these objects [55, 56]. The object classification methods are summarised in Table 5.

Table 5: Comparing the difference object classification methods [55]

Methods	Accuracy	Computational time
Shape-based classification	Moderate	Low
Motion-based classification	Moderate	High
Texture-based classification	High	High
Colour-based classification	High	Low

Shape-based classification

Shape-based classification depends on the geometry of the detected region in motion to classify the objects. Shape-based classification requires less computational resources compared to the other classification methods and is moderately accurate [53]. Different geometrical descriptions of objects in motion can be represented as points, boxes and/or blobs, which can be used in the classification of objects [55].

Motion-based classification

Motion classification is a very robust and adaptive method. Since this method does not use any predefined pattern or template, it struggles to detect stationary objects. Motion classification is computationally expensive but moderately accurate [53, 55]. Non-rigid objects in motion (like humans) mostly have a periodic property, which is helpful in motion-based classification [55].

Texture-based classification

The texture-based classification method can be divided into two phases: the learning phase and the recognition phase. In the learning phase, known features

are extracted from initially introduced textured images. In the recognition phase, these features are used to detect the desired object from frame to frame. Texture-based classification accuracy can be good, but has a high computational load [53].

Colour-based classification

Colour-based classification makes use of an object's unique colour pattern to classify the object within the detected region. Colour features are easy to acquire and remain quite constant under changes in viewpoint and therefore have a low computational load. Colour classification is highly accurate [53, 55].

Object tracking

Object tracking can be defined as the approximation of the path travelled by a target object within a video sequence by locating the object's real-time position in every frame within a video sequence. The target object must be extracted, then recognised and finally tracked. Three commonly used object-tracking methods are point tracking, kernel tracking and silhouette tracking [55]. These methods are summarised in Figure 11.

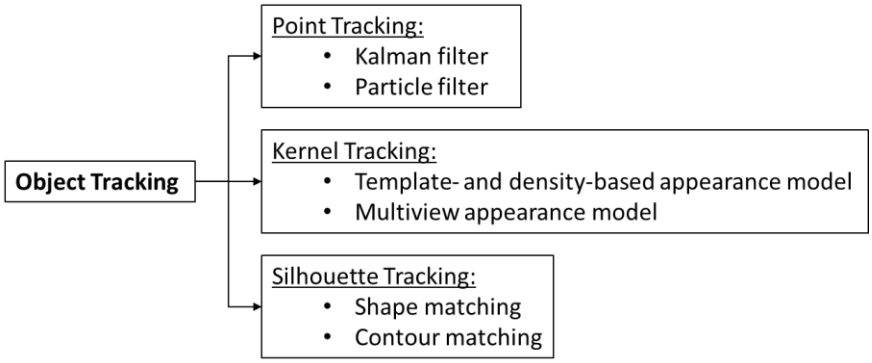

Figure 11: Object-tracking methods [55]

Point tracking

In point tracking, moving objects are represented by their feature points and these points are tracked throughout a video sequence [55]. The challenge with point tracking is finding the correspondence of the points between the frames. Errors are mainly caused by occlusions, false detection of objects, and entries and exits of the object [54, 55]. The correspondence issue can be improved using tracking filters. Commonly used tracking filters are the Kalman filter and the particle filter [55].

Kernel tracking

Kernel tracking is based on the motion of an object. It works by computing the motion of the desired object and presents an object region from one frame to the next [56]. The motion of the object is usually a form of parametric motion (like translation, affine transformation, etc.) [55, 56]. The kernel-based tracking algorithms differ in terms of the presence representation used, the required number of objects being tracked, and the object motion approximation method used [54, 55, 56]. Geometric shapes are often used to represent objects (detected regions) in real-time tracking. This can be a problem in rigid and non-rigid objects because parts of the desired object or background can be left outside or exist inside of the geometric shape [55]. Kernel tracking can be divided into two subcategory models, namely the template- and density-based appearance models and the multi-view appearance models [56].

Template- and density-based appearance models

Template- and density-based appearance models are widely implemented because of their relatively simple algorithms and low computational requirements. These models can be used to track an individual object or multiple objects [56].

To track individual objects, the most common model is the template matching-based appearance model. This model searches (within a video sequence) the current image frame for an object region similar to the object template defined in the previous image frame. In creating the image template, mostly colour features and image intensity are used. To reduce computational requirements, the detection region can be reduced to the region of the position of the object in the previous image frame. Instead of templates, colour histograms can be implemented as object representations within the detection region [56].

Only modelling a single object does not consider interactions between different objects and between the objects and the background as these objects are being tracked. To track multiple objects using this approach, the entire image is modelled as a set of layers: a layer for the background and a layer for each object [56].

Multi-view appearance models

If the tracked object changes dramatically during tracking, the template/density appearance model is likely to be invalid and may lead to losing track of the object. The multi-view appearance model can overcome this issue. In this model, different views of the desired object can be modelled before tracking. This modelling is done using various images of different viewpoints of the object, and as an initial object-learning phase before the tracking phase starts [56].

Silhouette tracking

Silhouette tracking is used when an accurate shape description of the object is required for tracking. Therefore, to achieve the tracking of objects with complex shapes (like hands, heads and so on), silhouette-based models are used [54, 56]. The aim of silhouette-based models is to locate the desired object's region in the current frame by using the object model generated in the previous frames. Colour histograms, object contours or object edges can be used in forming the object model [56]. The two main categories of silhouette tracking are shape matching and contour tracking [54, 56].

Shape matching

Shape matching searches for the desired object's silhouette in the current image frame. This shape-matching approach has equivalent performance to template matching. The search for the desired object in the current image frame is performed by computing the similarity of the object compared to the model generated from the presumed object silhouette derived from the previous image frame [54, 56].

Contour tracking

The contour-tracking approach starts from an initial contour to its new detection region in the current image frame. The contour then evolves as it progresses from frame to frame [56]. This evolving contour tracking requires the object's area in the previous frame to overlap with the object's area in the present frame. An evolving contour can be achieved by either using state-space models to model the contour shape and motion, or by directly evolving the contour. To achieving direct evolution of the contour, energy must be minimised by minimising algorithms such as steepest descent [54, 56].

2.5.2 Optical stereo vision

Optical stereo vision is the construction of a 3D environment developed from two or more 2D views of the same environment. It is used in various applications such as drone and robot navigation and can be used to calculate the actual distance to objects of interest. Digital/video cameras are used to capture these 2D views or images of the environment [57]. One major advantage of stereo vision is that it operates from the information received by the camera's FOV, therefore multiple stereo vision systems can work in a single environment without interfering with one another. A disadvantage of optical stereo vision systems is that the desired objects that lack texture can cause an error in the image-matching accuracy between stereo-paired cameras [58].

A basic stereo vision setup contains two optical cameras with overlapping FOV (see Figure 12). The first step in the stereo vision setup is to capture the calibration images for both cameras that would be used in the camera calibration process. These calibration images can be of any object with a known geometry; a black and white chessboard image is usually used (see Figure 14a). These images are captured at various distances and orientations. The known geometry of the images at various distances is used to calculate the camera matrix. The calibration process includes calibrating each camera in the stereo pair and then calibrating the cameras as a stereo pair. The main reason for single camera calibration is to determine each camera's matrix, which is then used in the stereo camera calibration to determine the projection matrixes of the stereo-paired cameras. These projection matrixes are then used in triangulation to determine information about the depth.

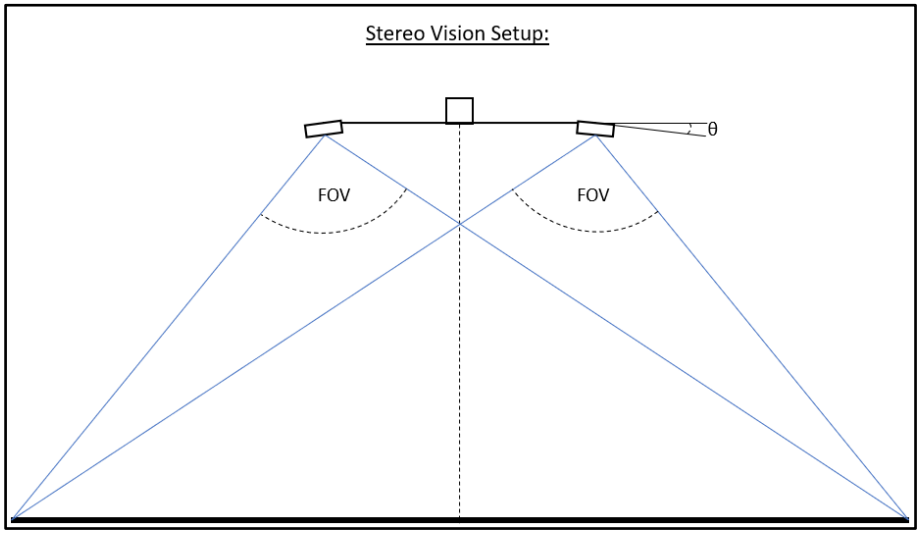

Figure 12: Stereo vision camera setup

The stereo vision system can be described by using mathematical equations. These equations, derived from the image, can then be used to calculate the distance of the object of interest relative to the cameras. A detailed background to these mathematical equations used to describe stereo vision, based on work done by Hartley and Zisserman [57], can be found in Appendix A.2.

2.5.3 Thermal stereo vision

Optical stereo vision is a known type of technology with a large area of research and has been used for more than 20 years [58, 59]. However, thermal stereo vision has recently been introduced into the literature and has been used in systems like human tracking, medical equipment and guided robots [58]. The advantages of thermal stereo vision over optical stereo vision include being more visually robust

in poor lighting, in conditions with changing light, and in conditions of smoke, fog and dust [58, 60]. Another advantage of the thermal stereo vision system in image processing is that it can extract the desired information based on thermal radiation. Figure 13a is a person as seen from a thermal camera and Figure 13b demonstrates how that person can be extracted based on the person's thermal radiation [58].

Figure 13: a) Thermal image of person and b) extracted desirable information [58]

Thermal and optical stereo vision are modelled in the same way, but there is one major difference – calibrating the cameras. Thermal cameras require much more work, because thermal cameras operate at a different wavelength range than optical cameras [58].

To calibrate a simple optical stereo vision system, calibration images (like the black and white chessboard) are captured at various distances and orientations. These images are processed to determine the projection matrixes of each camera in the stereo pair [58]. Capturing 2D calibration images (like the chessboard) to calibrate the thermal cameras is not straightforward. The thermal camera requires a heat chessboard-like grid (see Figure 14b) [58, 60, 61].

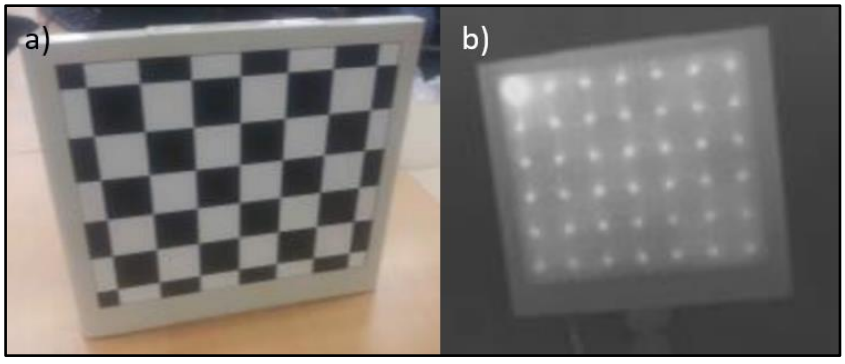

Figure 14: a) Black and white chessboard and b) thermal image of heat chessboard [61]

This heat chessboard can be created by using heat resistors in a grid formation, or by using a warm radiation source with a cold steel grid over it, or a printed chessboard-type printed circuit board (PCB) [58, 60]. The clearer the gird pattern, as seen from the thermal image, the better the calibration will be. This can be problematic with thermal cameras with low resolution [58]. However, this can be improved with a different calibration process [60]. The higher the thermal resolution of the camera, the higher the price of the camera will be.

2.6 Work done by others

In this section, previous work done and patents concerning SLS automation are discussed.

2.6.1 Touchless control of SLS

A study was done in 2013 to test whether it is feasible to automate an SLS using gesture tracking-based touchless control. The study made use of an experimental setup mainly containing an articulating arm with a laser pointer (mimicking automated SLS), an RGBD (red green blue depth) camera setup for depth estimation, and the controlling software (see Figure 15). The articulated arm and RGBD camera setup are off-the-shelf components, namely an Adept Viper 850s and a Microsoft Xbox Kinect respectively [7]. The control system was developed inhouse to manage communication between the Kinect and the articulating arm. This software was written in C and made up mostly of image processing using OpenNI API libraries [7, 62]. The Kinect makes uses of structured lighting to estimate depth information, which yields an RGBD image. Three tracking methods are used in the control system to manipulate the articulating arm. The tracking algorithms that are used in the control system will track either the user's one- or two-hand gestures, or the user's skeleton movement, with algorithms available in OpenNI [62].

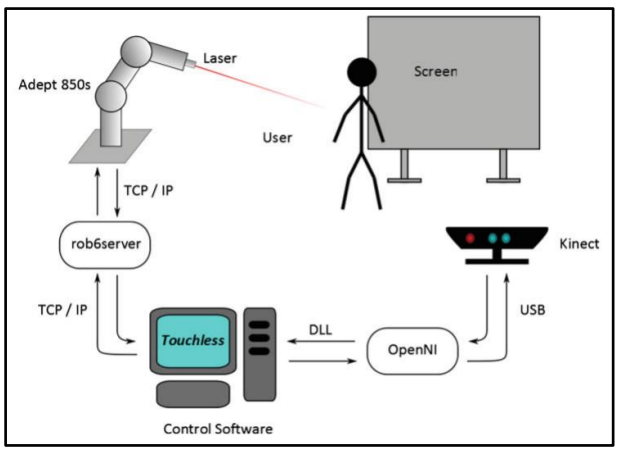

Figure 15: Experimental setup of the study [7]

The results of testing the hand-tracking capabilities of this setup showed a standard deviation tracking error (direction-dependent) of 1 mm and up to 3.5 mm depending on the orientation of the hand. The average speed of the hand tracking was 0.15 m/s and it took up to two seconds for the system to initiate control from hand gestures.

This study concluded that this is a feasible approach to adjust an automatic SLS using gesture control. However, one major drawback of this system is that it still requires user input and therefore will still disrupt the surgeon's complex workflow.

2.6.2 Automated SLS patents

Lamp and plenum for laminar air flow ceiling (Telstar Technologies) is a patent that was first active in 2010 and was still active at the time of this study. This is an SLS that is built into a laminar flow ceiling [63]. This system is not like standard lighting systems and therefore does not have any articulating arms. Instead, this system is part of the laminar flow system that is mounted on the ceiling (see Figure 16). To control the lighting system, a pointing device is used as a remote control to position the surgical light where the surgeon requires light. The major advantage of this system is that it there are no articulating arms to disrupt laminar flow or cause collisions. The major disadvantage of this system is that it still requires user input from the surgeons and therefore can interrupt the complex workflow in the theatre [64, 65].

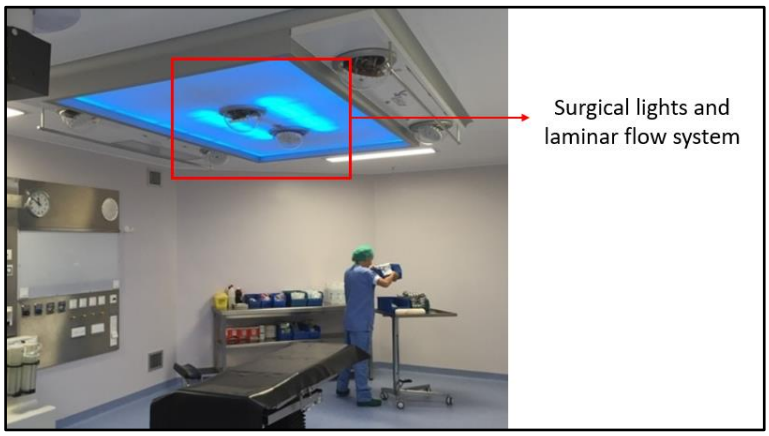

Figure 16: Surgical light and laminar flow system [65]

Automated surgical illumination system is a patent that was first active in 2012 and is still active to this day. This system makes use of an optical tracking system that is designed to automatically track an optical marker on the surgeon's surgical glove. The optical marker on the glove is an IR light emitter that can be switched on/off by the user. Here the automated SLS tracks the surgeon's glove with the optical marker attached to it. The SLS does not move when the optical marker is

switch off, and when the optical marker is switched on the SLS moves towards the surgeon's glove and starts tracking it [8]. The main drawback of this system is that the surgeon must keep track of when the optical marker is on/off, otherwise the light will follow when the surgeon moves away from the table or adjusts his hand.

Lighting system for medical procedures and *surgical lighting system* are two patents that rely on remote control to manipulate the surgical lighting systems [66, 67].

2.6.3 Discussion

In considering the abovementioned work and research done by others, the conclusion can be drawn that all the attempts at automation of surgical lights require some form of user input, whether it is hand gestures or remote control. There was nothing that could be found on adjusting the surgical light automatically without any user input. Therefore, tracking the surgical wound (main point of interest) without the surgeon needing to worry about the surgical light would be an ideal option. Other 3D position-tracking technologies were also considered (see appendix A.2), but these were quickly abandoned because all the technology required placing a transmitter/receiver at the surgical wound. Therefore, by combining thermal tracking with other tracking algorithms (section 2.4.3), it is believed that it will be possible to track a surgical wound through computer vision, although this will require further investigation. In this thesis, the focus is on achieving thermal identification of a single heat source, locating its 3D position through optical stereo vision and manipulating an articulating arm (analogous to an SLS) accordingly.

2.7 Conclusion

To conclude, the literature shows that there is technology available to achieve an automated SLS using thermal and optical cameras combined with image processing to track a surgical wound. However, it was decided to rather focus on achieving thermal identification of a single heat source and to combine this with optical stereo vision to track the 3D position of the heat source. To achieve the tracking of a surgical wound in a theatre, this identification algorithm will need to be improved.

3 CONCEPT GENERATION

3.1 Introduction

The need has been identified to automate SLS and technology is available to achieve this. In this chapter, the requirements to achieve this automation of the SLS will be discussed and from this, the engineering requirements will be defined.

3.2 Requirements

3.2.1 Allowed tracking error

The following describes the process used to find the allowed tracking error. Ideally, the centre of an SLS's light beam should be pointing at the centre of the surgical wound. SLSs come in various shapes and sizes, as do surgical wounds. Therefore, to determine the allowed tracking error, the data in Table 1 and Table 2 was considered. In selecting the wound size, the largest rounded incision size of the different orthopaedic surgeries was selected (10 cm). In selecting the light field size, an average light field diameter of 24 cm was selected. The light intensity (lux) of an SLS remains constant over the entire light field diameter that the light projects. The wound size and light field size were then used to calculate the allowed tracking error of 7 cm (Figure 17).

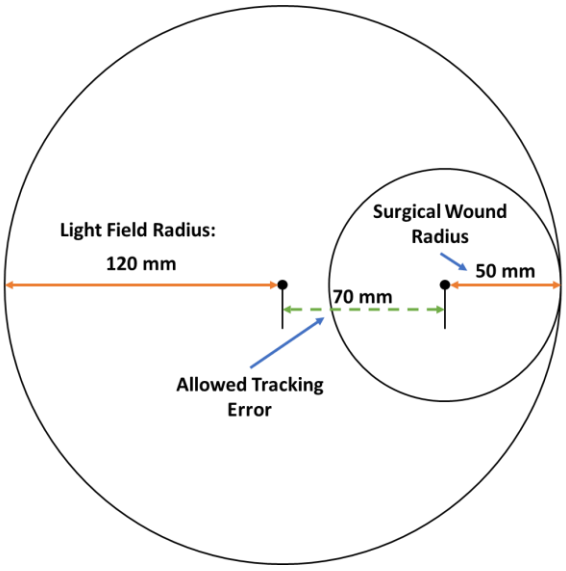

Figure 17: Allowed tracking error for SLS

3.2.2 SLS movements

In the literature, SLS movement is broken up into rotational and translational movement [5]. On the basis of this, it was decided to divide the SLS movement for this project into two primary movements and one secondary movement. The two primary movements are the arm translation and head rotation; these movements happen in the horizontal plane (Figure 18b). The secondary movement is the height adjustment of the surgical light; this happens in the vertical plane. In the design of the surgical light, it was decided to automate the two primary movements and leave the secondary movement to be manually adjusted. The main reason for this decision was that, during the observation survey done while shadowing Dr Erasmus, most light adjustments were done in the horizontal plane (86%).

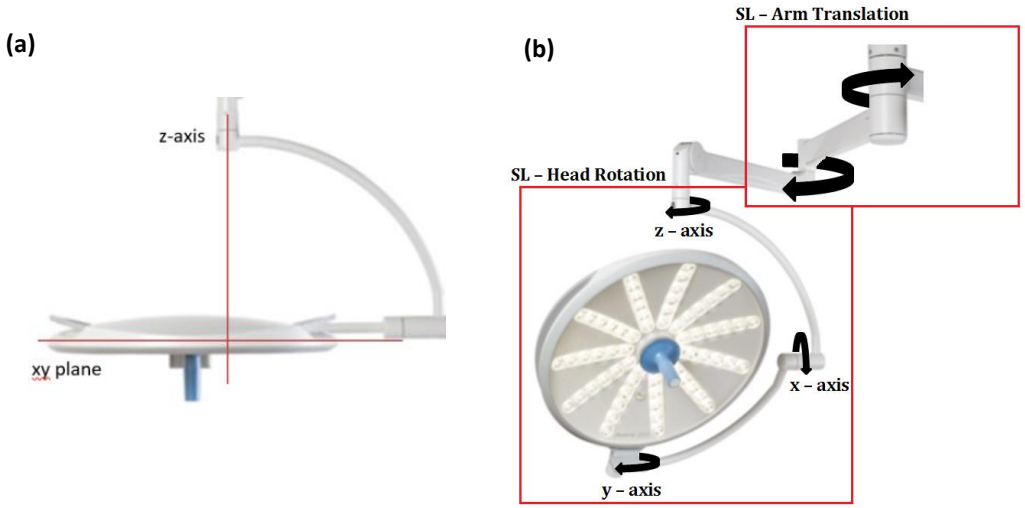

Figure 18: Surgical light head (a) in the home position and (b) the division of the primary SLS movements [3]

Arm translation or head rotation movement

If the surgical wound is adjusted, an LA is required to ensure that the surgical wound remains well illuminated. This LA could be accomplished by either head rotation or by arm translation. In head rotation, adjusting the pitch and roll axis of the light head would keep the beam of the SLS on the wound as it is adjusted from the home position. In arm translation, the arm's stepper motors would be activated to ensure that the light head remains above the wound during LA, with the light head remaining in its home position (Figure 18a). The drawback of using either arm translation or head rotation is that, if the light beam were at too great an angle (θ) relative to the surgical wound (Figure 19), the chance of shadows over

the wound increase, as surgeons and OR personnel can move between the wound and light head.

Combining arm translation and head rotation movement

The design/shape of the SLS compensates for situations in which the light beam is obstructed by hands or operating utensils. In addition, surgeons tend to avoid leaning over open surgical wounds during procedures to decrease the chances of wound infection. Therefore, to reduce the chance of causing a shadow over the wound, the light head must remain directly above the wound at all times; the light beam would always be pointing vertically downwards into the wound.

Given this, the main drawback of an adjustment using only translation is that each time the wound is moved even slightly the entire SLS would have to be adjusted to ensure that the surgical light head remains above the wound. It was decided to combine the movement with head rotation to reduce these drawbacks so that, if the wound is adjusted only slightly, only the surgical head will rotate and not the entire SLS. To combine the two movements, a grid of 4 x 4 square blocks was drawn on the workspace, as seen in Figure 20. Each block represented a different position, with A1 being position 1, A2 being position 2, …, D4 being position 16. The positions were situated in the centre of each block on the workspace. If the wound moved to a different block, the SLS assembly would adjust using arm translation until the light head was directly above the position of that square block, after which the surgical light head would take over and adjust to follow the wound within that block. As the wound moves out of the current block to a new block, the assembly would adjust to its new position and so the process would be repeated.

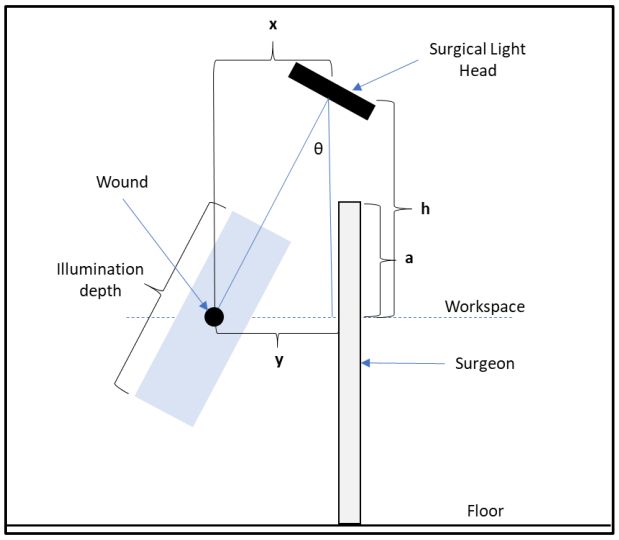

Figure 19: Surgical light and workspace setup

The square grid size and block size can be adjusted by increasing or decreasing the number of blocks. Increasing the number of blocks increases arm translation and decreases head rotation. The opposite is true when decreasing the number of blocks. Many factors influence the selection of the right grid and block size, but the main factors include the height of the surgical light from the workspace, the distance the surgeon stands from the wound, the height of the surgeon and the illumination depth (depth of focused light).

A 1 Position 1	2 Position 2	3 Position 3	4 Position 4
B Position 5	Position 6	Position 7	Position 8
C Position 9	Position 10	Position 11	Position 12
D Position 13	Position 14	Position 15	Position 16

Figure 20: Block grid on workspace indicating the different positions

A worst-case scenario was used to calculate the grid and block size, on the assumption that the light was directed at the edge of the block and the surgeon was standing directly between the surgical light and the wound (Figure 19). Also, it was assumed that the surgeon was as tall as an average male (1.76 m [68]) and standing more or less 150 mm (this was observed) away from the wound. An average illumination depth was used; this average was calculated from Table 2. This gave a maximum theta angle of 5.7 degrees of the light beam relative to the surgical wound (Figure 19). These calculations can be seen in Appendix E.1.

3.3 Engineering requirements

The following engineering requirements were formulated.

- To fully automate the SLS, LA should happen automatically when required. This will reduce mechanical challenges, prevent the surgeon's surgical workflow from being interrupted, and the surgeon will not be required to come into contact with the SLS, thereby making the surgery more hygienic.

- The SLS must not take longer than six to eight seconds to perform an LA. LA must be accomplished as the surgical wound changes.

- To reduce shadows over the surgical wound, the head of the SLS should remain above the surgical wound and not exceed an angle greater than 6° relative to the surgical wound.

- The tracking error after an LA was performed should not exceed 70 mm.

- To perform an LA every time the surgical wound is adjusted, the surgical wound must be tracked, and the wound's location must be known in 3D space in real time (a data-receiving rate of 1 Hz).

- The automated SLS must be fully functional without any human interaction for the performance of an LA during surgeries to ensure the surgeons' workflow remains uninterrupted.

- Surgeons must not be required to wear any extra equipment.

3.4 Concept

This concept makes use of an identification and tracking algorithm, first to identify the surgical wound and then to track the wound in 3D space. A thermal camera is used to identify the surgical wound; this makes it possible to identify the wound through the thermal radiation emitted from it. The thermal camera is used to display the thermal image of the wound, and this is combined with a colour classification algorithm to identify the wound within a temperature range. The major disadvantage of this concept is the price of thermal cameras, but because the camera is only used for identification purposes, it will probably not be required to produce an image of excellent quality. Seek [69] and FLIR [70] are thermal imaging companies that produce small thermal imaging cameras for smartphones, namely the Seek thermal and the FLIRONE. These thermal imaging cameras are small and affordable compared to other thermal imaging cameras, with one drawback being the thermal image quality. Another drawback of this concept is that it is not sufficient to identify the surgical wound by temperature alone, leading to the need for the process to be combined with other identification algorithms, as mentioned in section 2.4.3.

To track a surgical wound's 3D position in real time, the concept of stereo vision is used. The idea here is to use a digital camera and a thermal camera and to mesh their images to allow for thermal identification and digital tracking through optical stereo vision. The drawback is that using both a digital camera and a thermal camera is very expensive; however, the thermal imaging company FLIR produces a thermal imaging product that incorporates an optical camera and thermal

camera side by side. Therefore, the FLIRONE Generation 2 (F1G2) was selected due to its functionality and cost (see Figure 7). The optical camera was used for the stereo vision algorithm (wound tracking), and the thermal camera was used for the thermal object identification algorithm (wound identification).

The major reasons for using the thermal and digital camera concept were because wound identification and 3D tracking in real time could be achieved without the need for an external device/feature to be added/placed near the surgical wound, and surgeons would not be required to wear extra equipment.

The thermal and optical cameras were mounted on an SLS surrogate, designed and built as part of this project. The SLS surrogate was scaled down from a standard SLS to simplify building and testing. A standard SLS has seven degrees of freedom (DOF), and most of these DOF were adjusted using actuators on the SLS surrogate. A heat source was made from ceramic resistors to simulate the thermal radiation emitted from a surgical wound. The identification and tracking algorithm communicated via serial communication to the SLS surrogate, which was controlled by a microcontroller.

4 SYSTEM DESIGN

4.1 Introduction

The system used to achieve the expected outcomes and satisfy the engineering requirements was divided into two subsystems, namely the control system and the mechatronic system. The diagram in Figure 21 describes the systems' basic components.

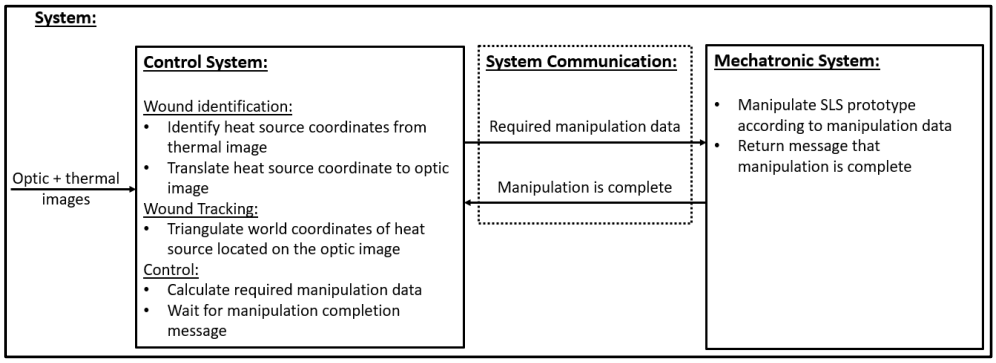

Figure 21: System components

4.2 Control system design

4.2.1 Introduction

The control system consists of an algorithm that identifies and tracks a heat source (simulating a surgical wound, see Figure 10). It does this by retrieving both optical and thermal images (frame by frame from a video sequence) and processing these images in real time. The wound-identification section describes the process of identifying, representing and tracking the heat source by a single camera (in 2D), and the wound tracking section describes the process of using stereo vision to track the heat source in 3D space by using two cameras. This process was packaged in a graphic user interface (GUI). The algorithm was developed in Visual Studio Code, which is a source code editor [71]. Python [72] was the programming language used. OpenCV is an open source computer vision software library and was used in compiling the identification and tracking algorithms [73]. OpenCV version 3 was used [74].

4.2.2 Wound identification

The process to identify, represent and track the heat source is explained for both an optical and a thermal camera. This wound-identification algorithm was designed to identify the desired object through a colour-filtration process and to

then classify the object based on its colour. The wound-identification algorithm can be divided into three sub-algorithms: the image-filtering algorithm (optical camera), the thermal image-filtering algorithm, and the object-tracking algorithm.

The reason for first using the images captured by the optical camera before applying it to the images captured by the thermal camera was to test the wound-identification algorithm. While testing the optical camera, the target was a small blue ball (see Figure 27). When using the thermal camera, the target was the heat source (see Figure 29). The identified objects were then tracked from frame to frame by their colour. The functions used in the wound-identification algorithms were from the OpenCV library [74].

Optical object identification

To identify the desired object by its colour, the following image-filtration algorithm was used. The optical camera was read frame by frame. The frame's red, green and blue (RGB) colour space was then converted to the hue, saturation and value (HSV) colour space, known as the HSV image. This conversion was done using the cvtColour function [75]. The reason for the conversion of colour spaces was that it enhances the image's colours to make it easier to distinguish between them [76].

The lower and upper HSV colour space limits were defined using values from 0 to 255 respectively. The algorithm displayed a taskbar on which the lower and upper HSV limits could be adjusted. This must be done manually by the user to identify the desired object (through its colour) before the tracking can take place. The inRange function [75] uses the HSV image with the adjusted lower and upper HSV limits to display a binary representation of where the desired colour was detected. This binary representation is defined as the threshold image. Therefore, by adjusting the taskbars, a desired colour can be identified (detected region), which is displayed on the threshold image in white; the black represents the undesired colour(s) in the image.

Once the lower and upper HSV limits of the target's colour were found on the desired object, the values were stored and later used to track the object from frame to frame (see Figure 26).

Thermal object identification

To identify the surgical wound by its temperature range, the following thermal image-filtering algorithm was used. This thermal image-filtering algorithm was based on the image-filtering algorithm mentioned above, with the only difference being that the thermal image was used. The desired colour range for the thermal image could be identified by adjusting the HSV limits and to track a certain temperature range on the thermal image.

The lower and upper HSV limits of the thermal image were also stored once they were found and were used in the object tracking algorithm (see Figure 28).

Object representation and tracking

Once the object had been identified, the object was represented by way of a geometric shape as a visual aid and tracked from frame to frame. A frame is equivalent to an image plane.

The object tracking algorithm used the stored HSV limits (optical/thermal, depending on the object tracking selected by the user; Figure 23) to identify the object on the image plane – this was defined as the detected region. The algorithm then drew a circle of best fit around the detected region, found the circle's centre and represented this centre by a cross drawn on the image plane. This cross therefore represents the object's position, namely its x and y coordinates on the image plane. This process was repeated from frame to frame each time the object's position was updated. The object was tracked from frame to frame in real time, at ± 8.7 frames per second (fps). This was the maximum frame rate of the thermal and optical cameras used [77].

The object tracking algorithm was performed simultaneously for the left and right image frame, finding the image coordinates (x_L, y_L and x_R, y_R) of the object on both planes (see appendix A.1). These image coordinates were later triangulated to find the object's world coordinates (x_w, y_w, z_w) (see appendix A.1). In the thermal object tracking, the image coordinates were first translated from the thermal image to the optical image before triangulation. OpenCV library functions [75] were used in the object tracking algorithm.

4.2.3 Wound tracking

Wound tracking required triangulating the object's world coordinates from a pair of image coordinates. When optical object tracking is selected, the identified object's coordinates in the optical images are triangulated, but when thermal object tracking is selected, the identified object's coordinates in the thermal image plane are first translated into the optical image plane and then triangulated (optical/thermal, see Figure 27 and Figure 29). This was repeated from frame to frame so that the object's position in 3D space would be updated each time its position changed. This tracking was performed in real time at ± 8.7 fps. A TriangulateDLT function [78] was used to triangulate the world coordinates. The TriangulateDLT function is a robust function coded by Schreve [79]. The left and right image coordinates and projection matrices were entered into the triangulation function, returning the world coordinates of the object. This was repeated from frame to frame so that, each time the object's position in 3D space changed, the world coordinates were updated, therefore tracking the object. This

was all done in real time at ± 8.7 fps, based on the available frame rate of the thermal cameras.

4.2.4 Control GUI design

Figure 22 shows the outline of how the GUI algorithm interacted with the main control algorithm.

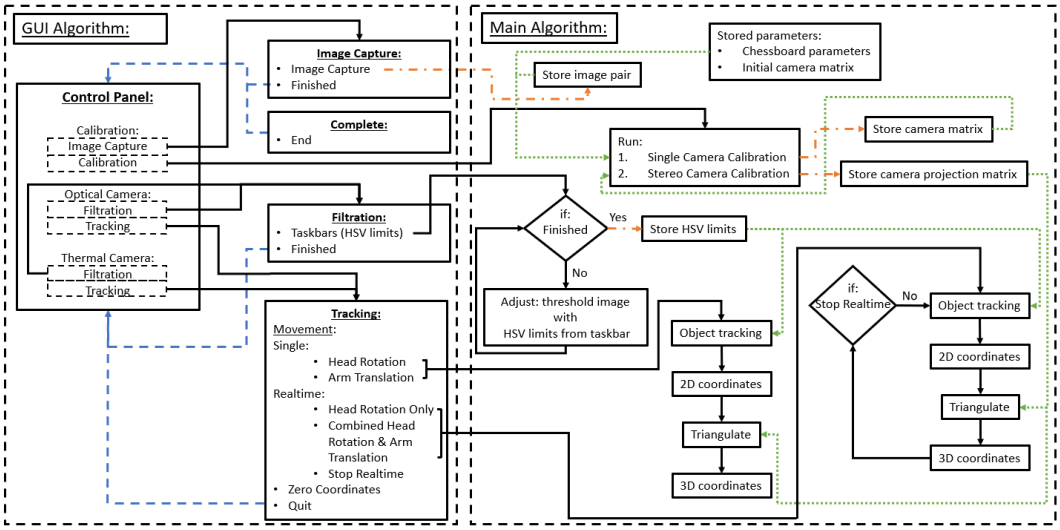

Figure 22: Algorithm outline

The following subsection describes the GUI algorithm. Italicised text represents the text seen on the GUI. TkInter [80] is a GUI toolkit for Python and was used for the GUI design. Figure 23 displays the *Control Panel* window when the code is run (Figure 23).

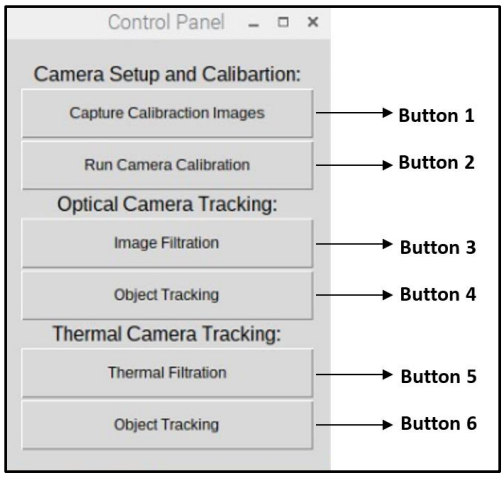

Figure 23: GUI control panel window

The *Control Panel* window was the main control panel and contained three main operations: *Camera Setup and Calibration*, *Optical Camera Tracking* and *Thermal Camera Tracking.* Each operation contained two functions (six buttons in total), (Figure 23). The *Camera Setup and Calibration* functions only needed to be run once because the camera and projection matrices were stored for later use. If the cameras were physically adjusted, the *Camera Setup and Calibration* had to be run again.

Camera Setup and Calibration:

When **button 1** (*Capture Calibration Images*) was pressed, the *Capture Image Pairs* window was displayed (Figure 24).

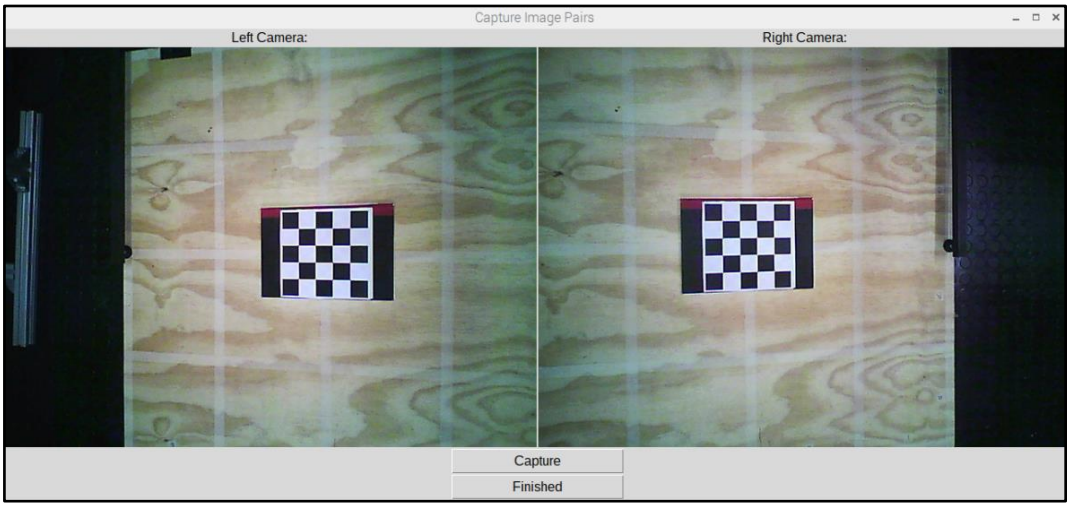

Figure 24: GUI window "capture image pairs"

The *Capture Image Pairs* window ran the algorithm using the optical camera to capture stereo image pairs. The GUI window displayed the views of both the left and right cameras and had two buttons: one to *Capture* the image pairs, and another (*Finished*) to return to the *Control Panel* window after image capture. These image pairs were stored and later used for the calibration of the camera.

Button 2 (*Run Camera Calibration*) ran the camera calibration algorithm as described in section 4.5.3. This calibration routine mainly uses OpenCV functions. First, the single-camera calibration algorithm ran for both the right and left cameras, after which the stereo camera calibration algorithm was run. After the calibration was complete, the necessary parameters were stored, and then a GUI window opened that displayed "Calibration complete" (Figure 25). The *End* button triggered a return to the *Control Panel* window.

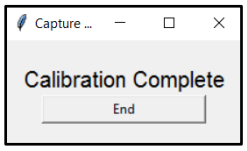

Figure 25: GUI window "calibration complete"

Optical camera tracking

When **button 3** (*Image Filtering*) was pressed, the *Image Filtering* window was displayed (Figure 26).

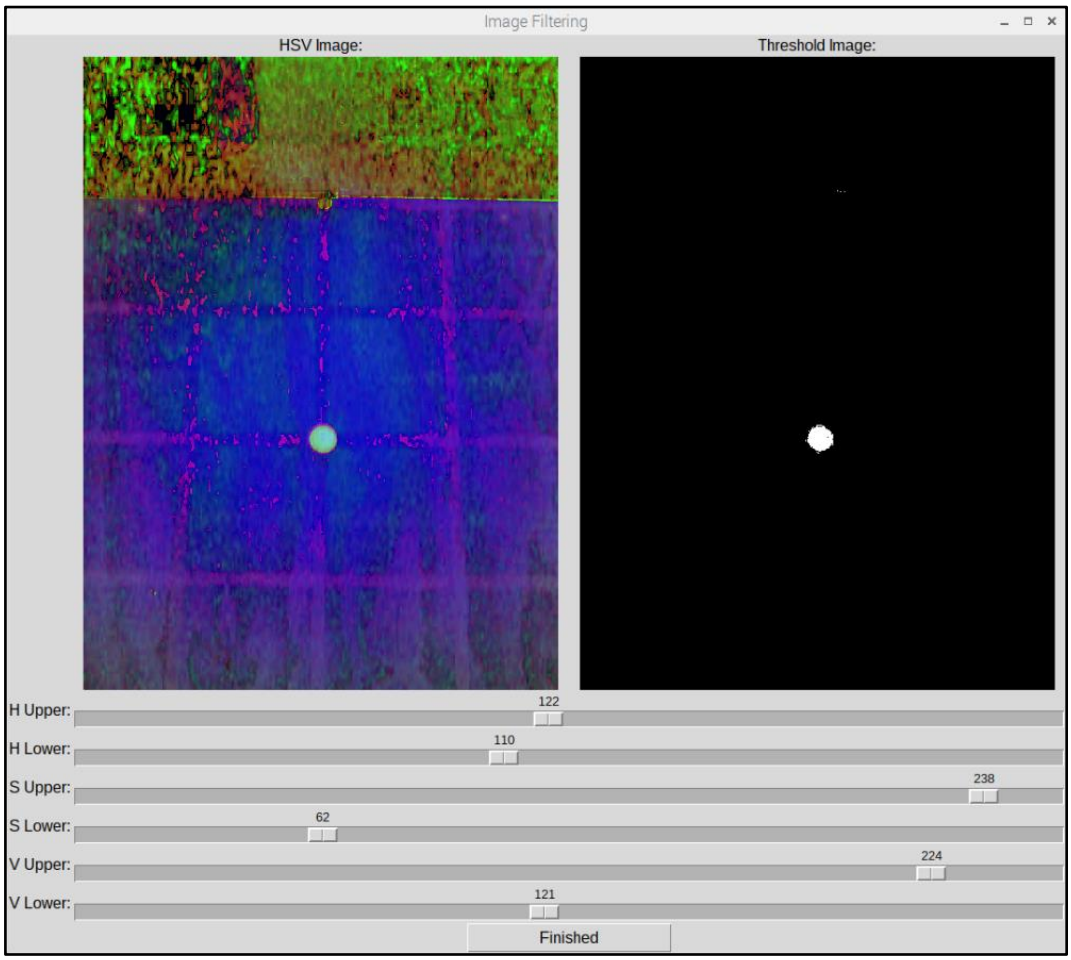

Figure 26: GUI window "image filtering"

The *Image Filtering* window displays the HSV image and the threshold image. This window includes a *Finished* button and taskbars that adjust the upper and lower HSV bounds so that the target can be identified. The user must initially set these values each time a new target is introduced. Ideally, only the target must be

displayed on the threshold image in white, and the black should represent the rest of the image. This will be an indication that the right HSV limits were selected. The upper and lower HSV values are stored once the *Finished* button is pressed and then one returns to the *Control Panel* window. The stored HSV values were later used in *Object Tracking* (**button 4**).

When **button 4** (*Object Tracking*) was pressed, the *Object Tracking* window was displayed (Figure 27).

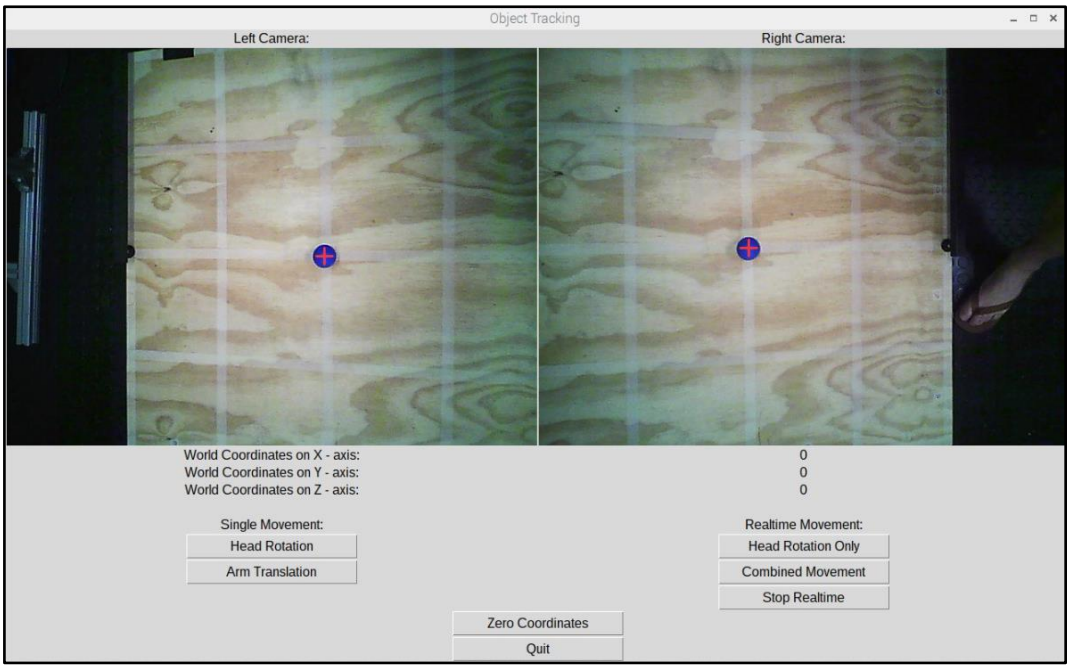

Figure 27: GUI window "object tracking"

The *Object Tracking* window displays the views from the left and right cameras and indicates the desired object with a red cross on the image frame of both cameras. The window also displays the object's 3D coordinates and included single and real-time movement buttons, as well as a *Zero Coordinates* button to zero the coordinates and a *Quit* button to return to the *Control Panel*.

Two buttons are available under "Single Movement": one for (single) *Head Rotation* and another for (single) *Arm Translation*. Here the prototype performed a single adjustment each time the button was pushed. Under "Real-time Movement", the prototype adjusted automatically each time the object being tracked moved. The automatic movement was divided into two types of movement: (real-time) *Head Rotation* and (real-time) *Combined Movement* (arm translation with head rotation). The combined movement is discussed in more detail in section 5.1.4. The *Stop Realtime* button stops the tracking process and stops the prototype.

Thermal camera tracking

When **button 5** (*Thermal Filtering*) is pressed, the *Thermal Filtering* window is displayed (Figure 28).

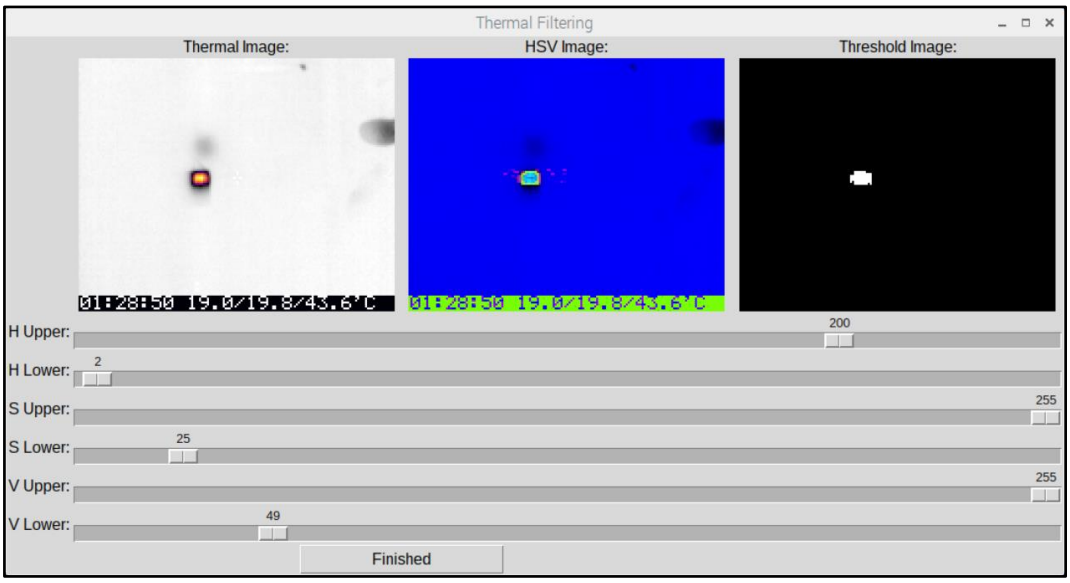

Figure 28: GUI window "thermal filtering"

The *Thermal Filtering* window contains the same information, buttons and taskbars as the *Image Filtering* window (Figure 26), but the main difference is that the thermal image is used instead of the optical image. The thermal image is also included on the GUI window.

Lastly, when **button 6** (*Object Tracking*) is pressed, the *Thermal Tracking* window is displayed (Figure 29).

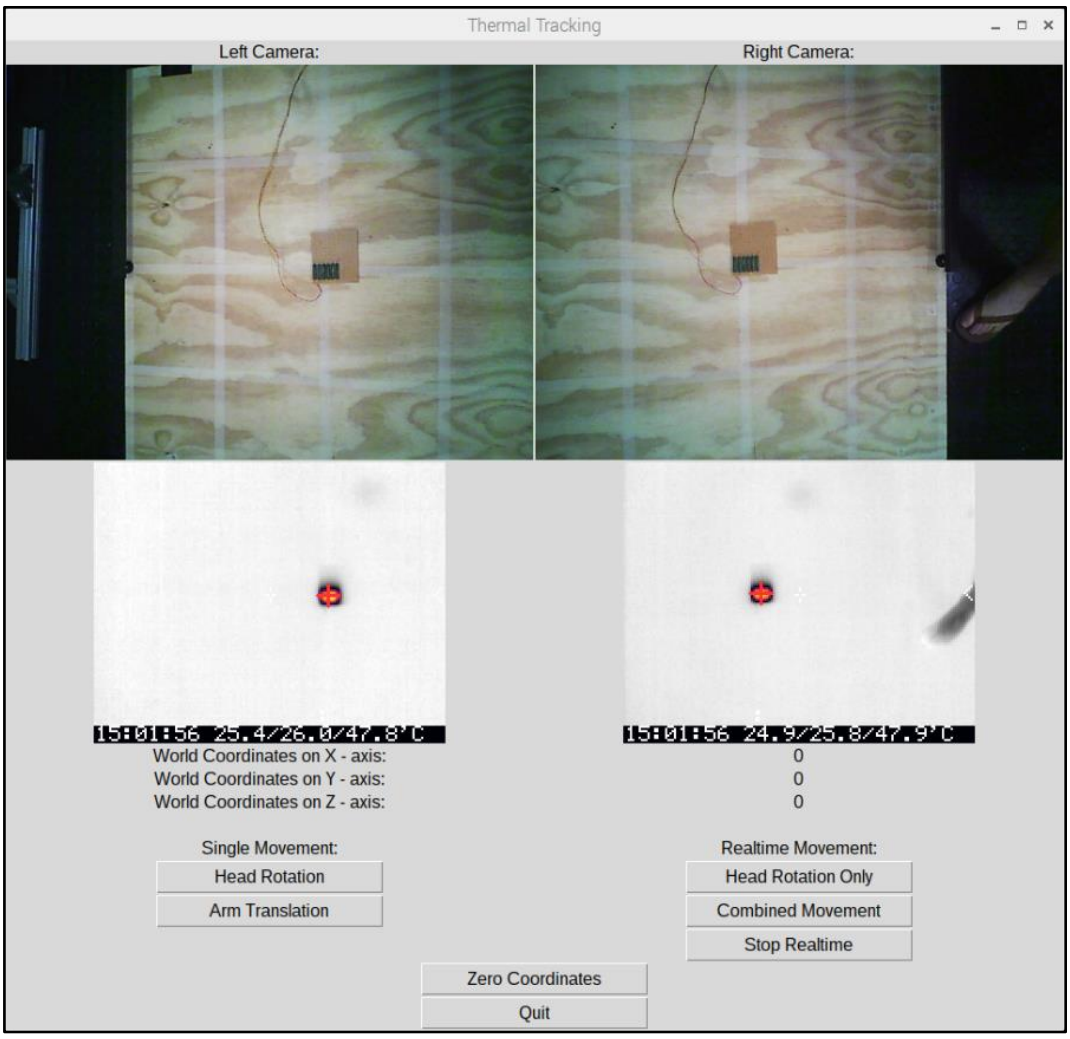

Figure 29: GUI window "thermal tracking"

The *Thermal Tracking* window is nearly identical (in terms of layout and functionality) to the *Object Tracking* window (Figure 27), except that the thermal images for both the left and right cameras are displayed.

4.3 Mechatronic system design

4.3.1 Introduction

The mechatronic system was the system that contained the design of the automated SLS surrogate as well as the software design that was used to manipulate the SLS surrogate, as communicated by the control system (Figure 21).

SLSs are large, overhead lighting systems used to illuminate the area of interest or the surgical wound within the OR. These overhead SLSs are purely mechanical systems that are adjusted by hand. To simplify the testing of the wound-identification and tracking algorithms, a scaled prototype of the SLS needed to be designed and built. In this section, the detailed design of the SLS surrogate is described. The description includes the entire mechanical design, motor selection and software design.

In designing the SLS surrogate for automation, only a single light head and its arms were considered (Figure 18). Since the SLS surrogate was designed mainly for testing purposes, using the available facilities was preferred for saving time and keeping costs low. The following were important aspects considered in the design of the SLS surrogate:

- The SLS surrogate must be small enough to test, and lightweight enough to move around as needed.
- The SLS surrogate must simulate the same functions as a conventional surgical light.
- The SLS surrogate must be adaptable so that hardware can be added or removed. Therefore, the SLS surrogate must also be strong and sturdy enough to function with extra hardware.

4.3.2 Mechanical design of SLS surrogate

The dimensions of standard SLS models were used to determine the average head size and arm lengths (Table 2). These SLSs have multiple light heads on separate articulating arms. One of these has seven DOF, as seen in Figure 18: two DOF for arm translation, two DOF for height adjustment, and three DOF for head rotation.

Taking this information into consideration, the following engineering requirements were selected to aid the design of the SLS surrogate:

- The SLS surrogate had to be scaled down to around a third of the original SLS size; this made the SLS surrogate small enough to test and lightweight enough for relocation if necessary.
- The SLS surrogate had to have seven DOF – two DOF for the arm translation and three DOF for the head rotation that was automated, while the height adjustment with two DOF remained manually operated.

The physical design of the surgical light surrogate was done using CAD software (Autodesk AUTOCAD 2016) [81]. The CAD design of the surrogate can be seen in

Figure 30 and in Figure 31. The home positions of the arms and light head are indicated in Figure 30 and Figure 32 respectively.

Arm translation design

Automation of the arms of the surgical light to achieve arm translation required that the two rotating joints indicated in Figure 18 be driven by motors. The surrogate arms would have two DOF because only the primary movements (xy plane), and not the secondary movement (z-axis), were considered, since surrogate arms would only translate in the horizontal plane.

The following points were the specifications considered in designing the surrogate arms:

- The SLS surrogate arms must have two DOF and the position of each arm must be controllable.
- The SLS surrogate arms must be as light as possible to reduce the effect of inertia and to reduce strain on the motor. The use of lightweight materials like aluminium and acrylonitrile butadiene styrene (ABS) plastic was preferred.
- The lengths of the surrogate arms had to be scaled down to about a 1:3 of that of a standard SLS's arms.

In the following subsections, *italicised text* is used to indicate parts of the surrogate annotated in Figure 30 and Figure 31. The primary movement was controlled by two motors fastened to *bracket 1*. The shaft extruding from *bracket 1* was attached to the ceiling. The first motor drives the spur *gears* that rotate *arm 1* and the second motor drives the *timing belt* that rotates *bracket 3*, thereby driving *arm 2*. The head of the SLS surrogate is attached to *bracket 4* to achieve head rotation. The motor selection and calculations are presented in section 5.3. The reasons for concentrating both stepper motors on a single bracket (*bracket 1*) at the rotating centre of the surrogate was to reduce the effect of inertia on the surrogate assembly. The secondary movement was designed to be adjusted manually (Figure 30).

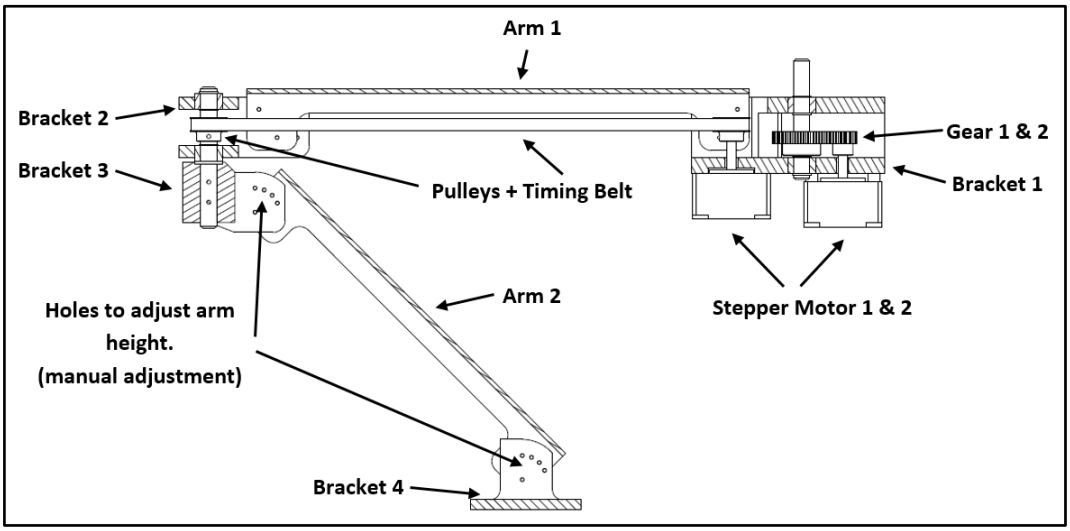

Figure 30: A sectioned image of the SLS surrogate [82]

Aluminium was chosen as material when designing the surrogate's *arm 1* and *arm 2* because it is lightweight, strong and affordable, compared to other materials like steel. The tops of the arms were slotted to reduce weight. *Arm 1* and *arm 2* were designed to approximate a third of the length of a standard SLS's arms (Table 2). These *arms*, as seen in Figure 30 and Figure 31, were designed using Autodesk inventor [81]. The detailed drawings and assemblies used in manufacturing the SLS's surrogate can be found in Appendix D.1.

The *arms* were manufactured by a local steel fabrication company (FABRINOX, Stellenbosch, South Africa). Arms were manufactured by laser-cutting the design from an aluminium sheet (material grade – 1050 A) and bending it as specified. Brackets, shafts and bushings were manufactured in the Mechanical and Mechatronics Engineering Workshop of Stellenbosch University. The *brackets (1-4)* were manufactured from ABS plastic by 3D printing using an M200 (Zortrax, Olztyn, Poland). The shafts were produced using stainless steel (material grade – 304), and the bushings were made from brass. Pre-made components (sourced from RS Components, Corby, United Kingdom) included aluminium pulleys, a wear-resistant polyurethane timing belt from stainless steel (material grade – EN8), spur gears, fasteners and circlips. More detailed descriptions of these components can be found in Appendix D.2, along with the calculations that defined their specifications. The manufactured surrogate assembly was found to satisfy the specifications.

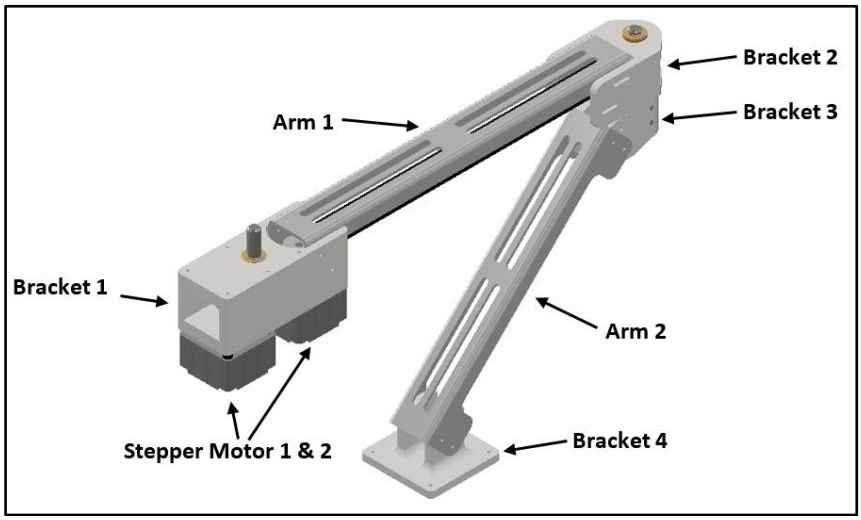

Figure 31: CAD image of surrogate [82]

Head rotation design

To achieve an equivalent automated head rotation in the SLS surrogate, each rotating joint on the x, y and z-axis must be driven by motors; these rotating joints are indicated in Figure 18. Because the light heads of the SLS are situated at the end of the articulated assembly, the surrogate's inertia would be influenced by the weight of the head.

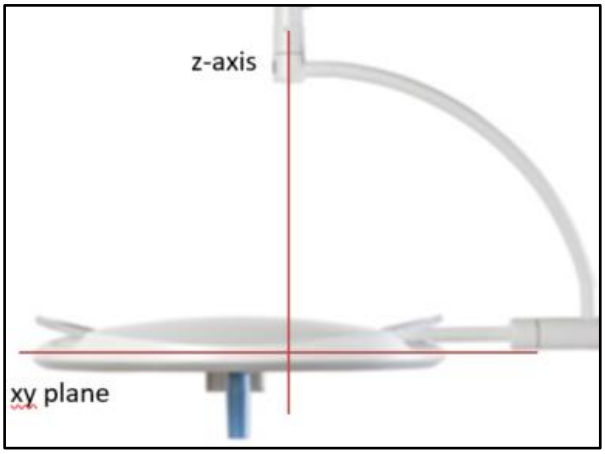

Figure 32: Orientation of standard surgical light head [3]

Therefore, these were the specifications considered when designing the SLS surrogate head:

- The SLS surrogate head must have three DOF and have position control on each axis, namely the x-, y- and z-axis.
- The SLS surrogate head must be as light as possible, at most 300 g.
- The head size of the SLS surrogate must be scaled down to about a third of a standard SLS's light head.

Rather than design and build a three-axis rotating head for the surrogate, it was decided to use a pre-made gimbal, namely the STorM32 three-axis gimbal (Figure 33). The gimbal fulfilled all the specifications described above and was more cost-effective (in terms of time and money) than building a custom surrogate. Its dimensions were 80 mm wide by 80 mm deep by 100 mm high, it weighed less than 200 g and the frame was made from aluminium. The gimbal had three DOF and each axis was driven independently by brushless motors.

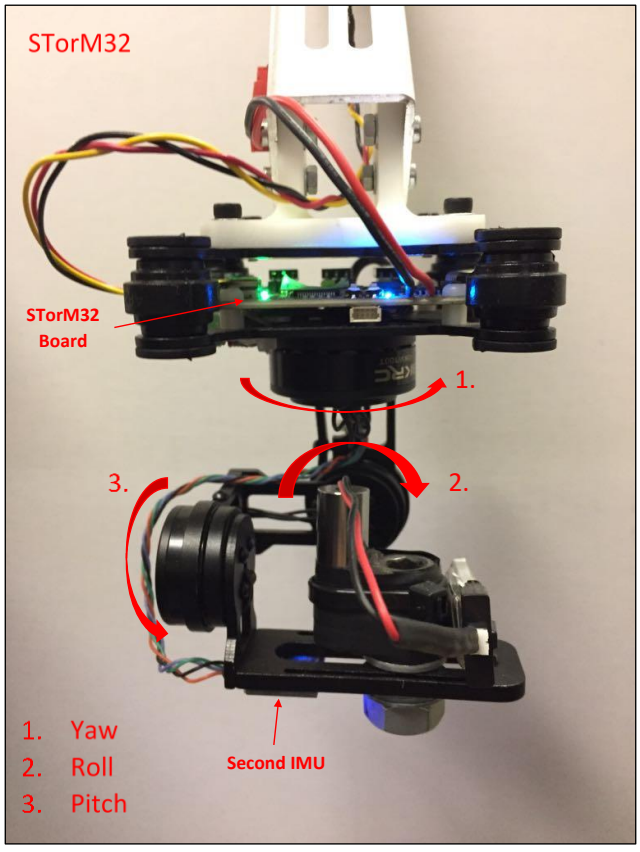

Figure 33: STorM32 gimbal in its home position, with brushless motors indicated

4.3.3 Motor selection for SLS surrogate

Head rotation

The x- and y-axis of the STorM32 three-axis gimbal were controlled by two 2206/100T brushless motors, and the z-axis was controlled by a 2804/100T brushless motor. These motors produced the required torque to achieve position control of the gimbal.

Arm translation

In the process of designing the surrogate, light materials were selected to keep the inertia of the surrogate as low as possible. The total mass of the assembly, which included the entire arm assembly and the gimbal, was 1.9 kg. The inertia and required torque were calculated. A safety factor of 1.5 was added to the torque to overcome uncertainties such as friction. The torque required to rotate *arm 1* was equal to 0.338 Nm and for *arm 2* it was equal to 0.255 Nm. The torque calculations can be found in appendix D.2.

The motor selected to rotate *arm 1* was a NEMA 17 stepper motor (17HS3001-20B) with a holding torque of 0.4 Nm, which was higher than the required torque needed to rotate *arm 1*. The motor selected to rotate *arm 2* was a NEVA 17 stepper motor (17HS1011-20B) with a holding torque of 0.28 Nm, which was higher than the torque needed to rotate *arm 2*. These stepper motors were ideal for this application, since the motors rotate in steps and therefore the position of the motor can easily be controlled by controlling the number of steps driven by each motor.

4.3.4 Software design of SLS surrogate

Microcontroller algorithm

The Arduino Nano microcontroller was programmed in its own Arduino programming language, which is based on C/C++ functions [83]. The microcontroller algorithm was programmed using the Arduino Software (IDE) platform and loaded onto the microcontroller through this platform. The outline of the microcontroller algorithm that was used to control the SLS surrogate can be seen in Figure 34.

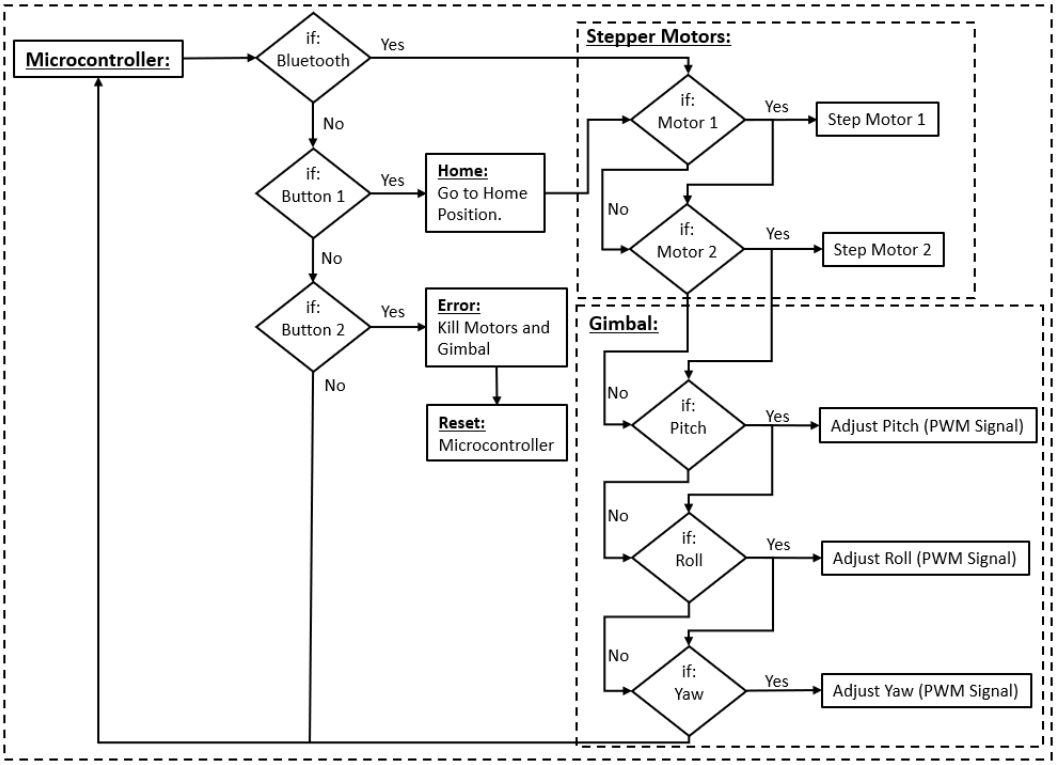

Figure 34: Outline of microcontroller algorithm

The function of the microcontroller algorithm was to wait for data input from serial communication via Bluetooth. This data input contained the number of steps and direction of each stepper motor, used for the arm translation, and the angles required for the gimbal, used for the head rotation. This data input was then used to adjust the SLS surrogate accordingly, and then returned a message through serial communication (Bluetooth) to indicate that the adjustment of the SLS surrogate had been completed.

Arm translation – Stepper motor communication

As mentioned above, an A4988 stepper driver was used to control the stepper motor. The microcontroller (Arduino Nano) communicated with the driver, and the driver communicated with the stepper motor. The microcontroller algorithm uses the "A4988.h" library [84] to adjusts the stepper motors. This library was designed to work with the stepper driver used and made use of the motor angle and direction to step the stepper motor in the position required.

Head rotation – Gimbal communication

After the gimbal had been calibrated (section 4.5.4), the next step was to direct the position of each motor to control the pitch, roll and yaw axes. These can be

controlled by generating a pulse-width modulating (PWM) signal that is input to the RC ports of the gimbal. The PWM signal frequency was set to a constant value and the duty cycle was varied. The duty cycle was the fraction of time the digital signal was active [85]. The PWM signal output was generated by the microcontroller. RC pins were configured by adjusting the input pulse lengths (duty cycle) to 1 to 2 ms. This was converted by the gimbal to a value in the range of -500 to 500. These values were used to control the different positions of each motor on the gimbal. Each motor was controlled by its own RC pin. The pulse frequency could be varied, up to a maximum of 430 Hz [86].

The Arduino Nano microcontroller made use of an ATmega328 chip, which contains three PWM timers controlling six PWM signal outputs; the clock speed of these timers was 16 MHz. The PWM signal frequency could be set and duty cycles could be adjusted by directly adjusting the chip's timer registers [85]. These registers for the PWM timers can be found in the AVR ATmega328 datasheet [87, pp. 144-165].

To achieve a PWM signal using the Arduino Nano microcontroller, the PWM timer2 was selected, and therefore PWM signals were outputted on pins 3 and 11 of the microcontroller. Next, the timer registers were set. First, the mode of PWM was set to fast PWM, and this was done by setting the waveform generation mode bit (WGM) to 011. Fast PWM is the simplest PWM mode, where the timer repeatedly counts from 0 to 255 [85]. Next, the COM2A bits and COM2B bits were set to 10 to ensure the PWM was non-inverted for output A (pin 3) and output B (pin 11). The clock speed (CS) bits were set to 110, which sets the prescaler to divide the clock by 256. This gave an output frequency of ± 244 Hz (16 MHz / 256 / 256) for both output A and B. After these registers were set, the output-compare registers (OCR) could be adjusted to determine the duty cycle of the PWM [85]. The microcontroller algorithm used the angles sent via Bluetooth to calculate the required OCR value. This changed the PWM signal to adjust the gimbal's pitch, roll or yaw axis, as required.

4.4 Hardware design

4.4.1 Control system hardware

FlirOne Gen 2

The FlirOne Gen 2 camera contains both an optical and a thermal imaging camera side by side on the device. The optical camera was required for two main reasons – firstly for the stereo vision calibration process, because the OpenCV calibration libraries were compiled for optical images and not thermal images; and secondly because the optical camera has a higher resolution, therefore the higher quality

calibration images led to higher stereo accuracy. The image resolution of the optical camera was 640 x 480 pixels with a frame rate of 8.7 Hz [77].

The thermal camera was then used for object identification to aid in the tracking process. The image resolution of the thermal camera was 160 x 120 pixels, with a frame rate of 8.7 Hz and a temperature range of -20 to 120°C, with a resolution of 0.1°C [77].

Raspberry Pi 3 Model B microcomputer

The Raspberry Pi 3 Model B is the microcomputer used, with Raspbian as the main operating system (OS). Raspbian is based on Debian, which is a Linux distribution [88]. The main programming languages for Raspbian are Python and Scratch [89].

The F1G2 is an Android device developed to run through a smartphone application. A driver is required to access both the optical and thermal camera of the F1G2 android device through another OS. Due to the complexity and time constraints, it was not possible to write a driver to operate on a Windows 10 OS. A driver to access the F1G2 devices that operates on a Linux OS [90] was found online. Therefore, the main reason for selecting the Raspberry Pi 3 as the microcomputer was because it had a Linux OS and the Linux driver found could be used to access the F1G2 device. Other reasons include that the Raspberry Pi would have sufficient processing power, enough USB ports and Bluetooth. The USB ports were required for both the stereo paired cameras (2 x F1G2) and a mouse and keyboard. Bluetooth was required to communicate with the SLS surrogate.

4.4.2 Mechatronic system

Arduino Nano microcontroller

For the SLS surrogate, it was decided to use a single microcontroller to control both the arm translation and the head rotation. This SLS surrogate required 12 digital outputs, three PWM outputs and serial pins (receive – RX and transmit – TX) for Bluetooth communication, two digital pins for two push buttons, two digital pins for two LEDs (green and red), two digital pins for each stepper motor (one pin for steps and one pin for direction), one digital pin to enable or disable the motors, and lastly three PWM pins to control each axis of the gimbal (pitch, roll and yaw). The Arduino Nano microcontroller was regarded as ideal for this application, since it has 22 digital pins of which six can be used to generate PWM signals [91]. The Arduino Nano is affordable, readily available, small and fast, and has low power consumption, which made it the ideal microcontroller for the SLS surrogate. The wiring of the microcontroller is illustrated in Figure 35. The wire connection diagram and schematic were designed using fritzing version 0.9.3b [92].

A4988 stepper motor drives – Arm translation

The aim was to develop a way to control the position of the stepper motors as quickly and accurately as possible. As seen in the motor calculations, when the speed of the stepper motors increases, the required torque of the motor also increases. If the required torque of the arm is not met, the stepper motor will start to miss steps, thereby losing accuracy. Therefore, to find the ideal speed of the stepper motor, tests were done by incrementing the speed of each motor until the stepper motor started to miss steps.

It was decided to use A4988 stepper motor drivers because they have an operating voltage of between 8 and 35 V and a maximum phase current of two amps. This maximum current output of the driver can be set with a potentiometer to allow for higher step rates and to ensure steps were not missed. The driver also has micro-stepping capabilities with five different step resolutions, namely full-step, half-step, quarter-step, eighth-step, and sixteenth-step. This means that, if the motor driver is set to half-step and the motor steps 200 steps per revolution, it would allow for 400 steps per revolution [93]. The Arduino, motor drivers and stepper motor wiring diagram can be seen in Figure 35. The maximum current output was set according to a reference voltage of 0.48 V for *motor 1* and 0.4 V for *motor 2*, as calculated in the datasheet [93].

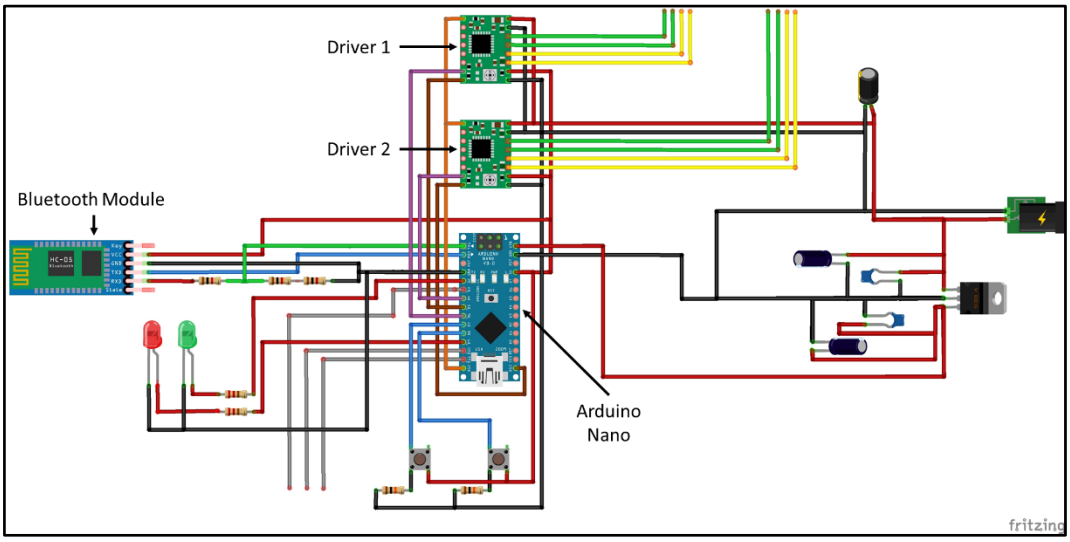

Figure 35: Surrogate wiring connection diagram of the SLS [92]

STorM32 gimbal – Head rotation

The gimbal's brushless motors were controlled by the STorM32 v1.32 controller board. This controller board supported three motor drivers (DRV8313), Bluetooth, two 6DOF inertial motion units (IMUs) – one onboard (MPU6050) and another

additional I^2C port for a second IMU (MPU6050), the PWM signal input/output ports and other various ports. These various ports included a two-axis joystick (POT) port, button (BUT) port and three auxiliary ports [94].

One IMU was onboard the STorM32 board and the second was an I^2C-based IMU connected under the gimbal on the pitch axis (Figure 33). The Arduino-Gimbal wire connecting diagram can be seen in Figure 35.

Miscellaneous

Other miscellaneous hardware included two LEDs, two push buttons and a Bluetooth module (HC-05), which were connected as in Figure 35. One button was used to send the surrogate back to the home position, one button was used to kill the stepper motors in case of an error occurring, one green LED indicated that the motor was in motion, and one red LED indicated that the "kill button" had been pushed. The Bluetooth module was used for wireless communication between the tracking/wound-identification algorithms and the SLS surrogate.

4.5 System design

4.5.1 System communication

System communication is the serial communication between the control system and the mechatronic system (Figure 36). The control system's algorithm used the position of the wound-simulating heat source on the workspace (world coordinates) relative to the origin to calculate (1) the required angles of each stepper motor for the required arm translation, and (2) the pitch, roll and yaw angles of the gimbal for the required head rotation. The home position was defined as the starting position of the surrogate, and this starting position can be seen in Figure 40c. A key consideration was that a period of time was required to stabilise the gimbal after it had been switched on. The completion of this stabilisation period was indicated by a beep sound. The stepper motors and gimbal angles were always calculated relative to the home position. These angles were then sent to the SLS surrogate through serial communication via Bluetooth.

On start-up, the microcontroller stored the home position of the surrogate arms and the gimbal stabilised to its home position, as shown in Figure 40. Each time a new LA was received by the microcontroller algorithm, the microcontroller algorithm calculated the required new position by using the SLS surrogate home position, the desired position relative to the home position and the current position to calculate the shortest distance from the current position to the desired position. This new position was then redefined as the current position. Once the surrogate had finished performing the desired adjustment for both arm translation and head rotation, the microcontroller alerted the tracking algorithm

via Bluetooth that the movement had been completed, and the process was then repeated (Figure 36).

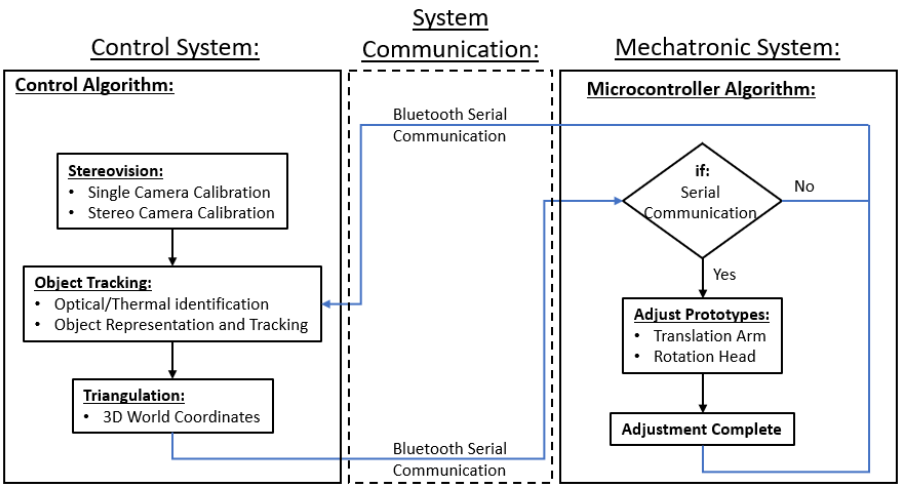

Figure 36: **Communication in control and mechatronic system**

4.5.2 System setup

The entire setup is broken down in **Figure 37**. It is important to take note that the thermal and optical cameras are part of the control system and not of the mechatronic system. The control system consists of the microcomputer, thermal and optical cameras, monitor, keyboard and mouse (see Figure 39). The mechatronic system consists of the articulating arms, gimbal, and the control hardware for the mechatronic system (see Figure 38).

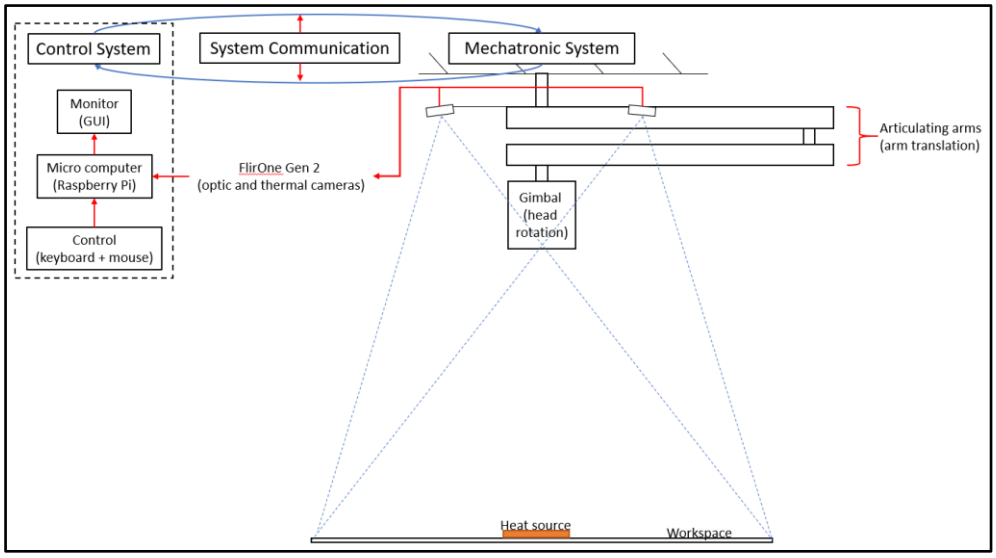

Figure 37: System setup

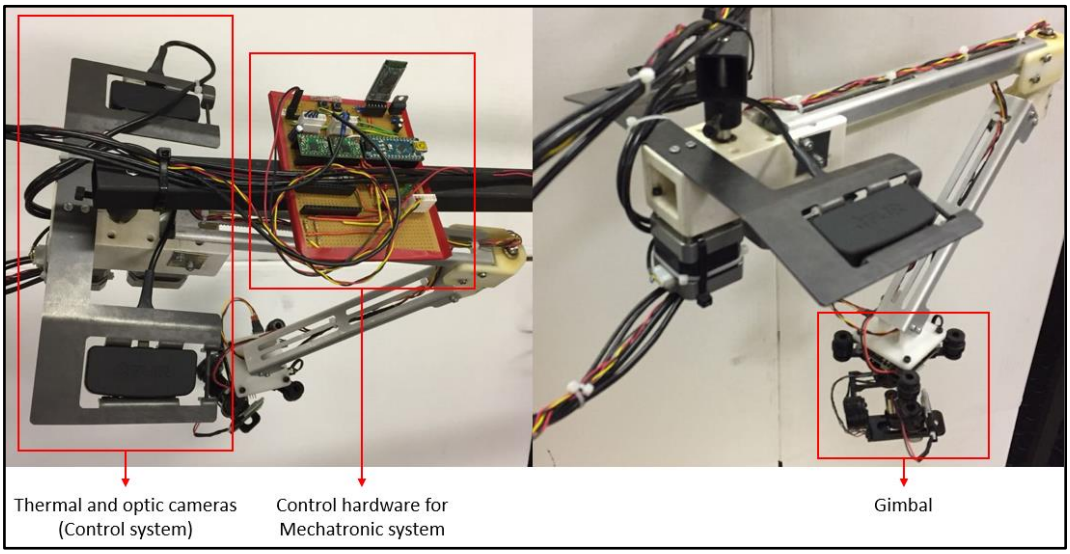

Figure 38: Mechatronic system

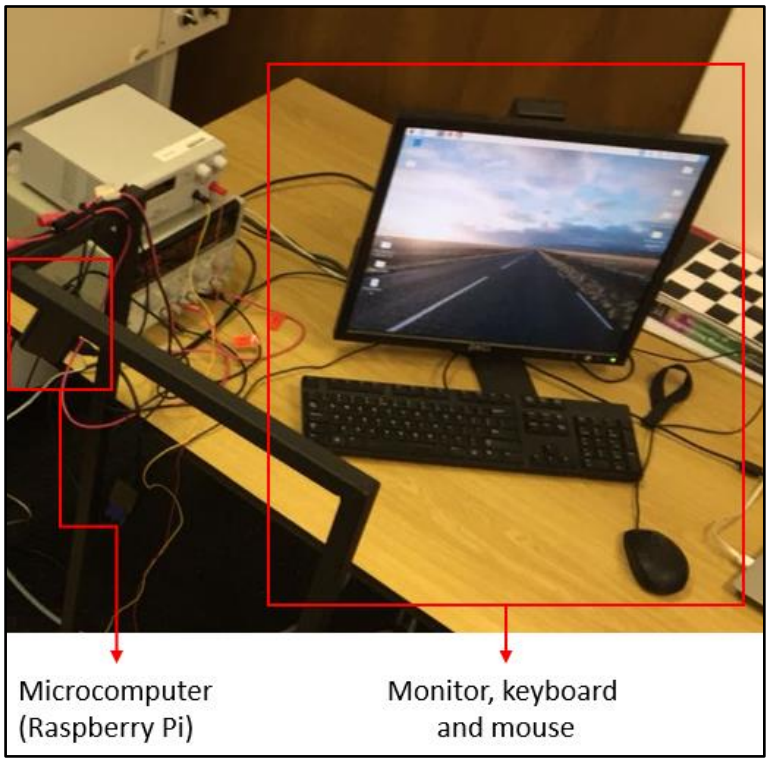

Figure 39: Control system

Figure 40 depicts the entire system setup with all the components labelled, the 3D coordinate system and the home position that represents the starting position of both the head rotation and the arm translation. The workspace in the test setup was represented by a wooden board with positions (Figure 40)marked out on it.

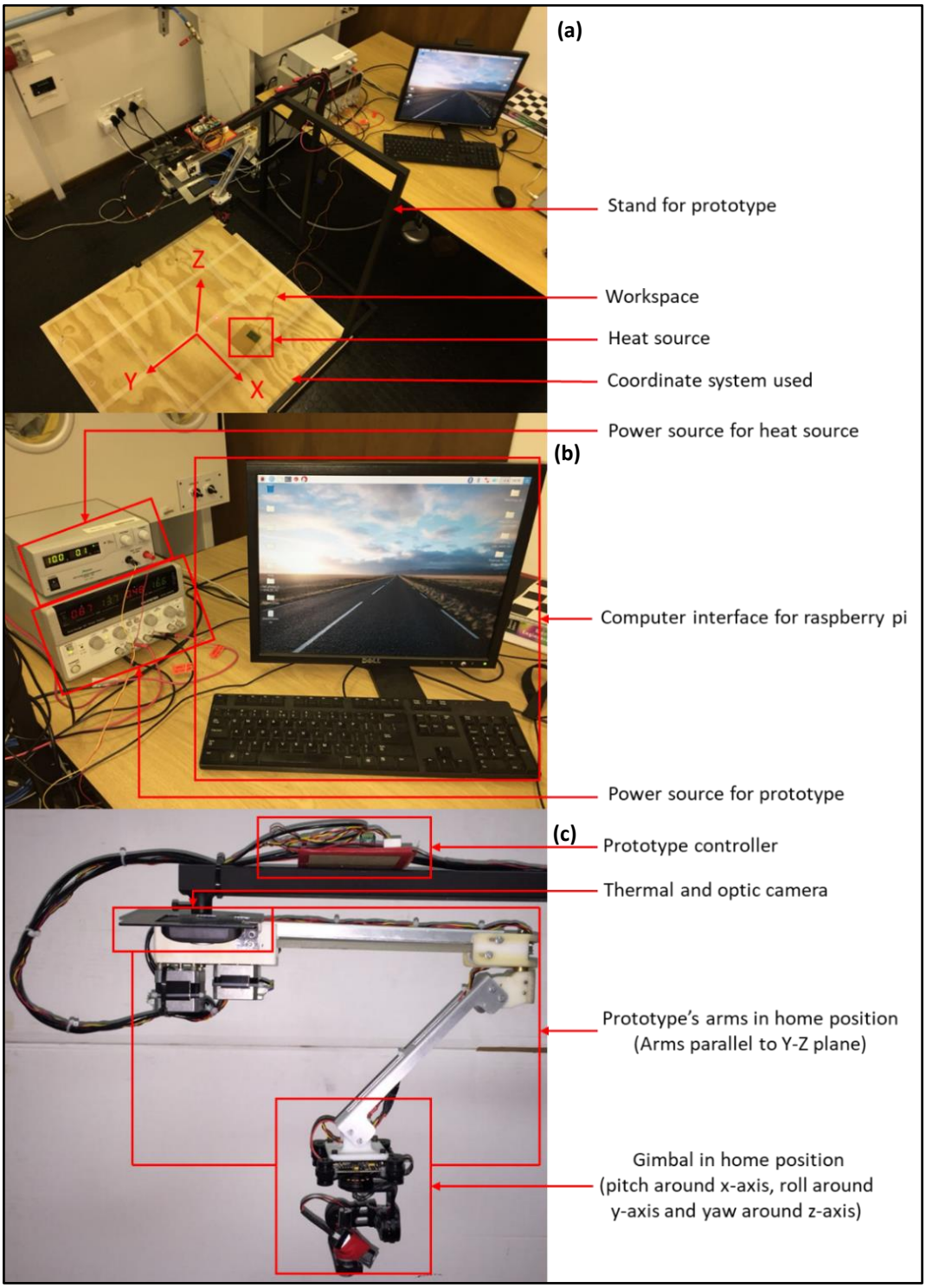

Figure 40: System setup. (a) View from above the workspace, stand and surrogate; (b) Computer and power source; (c) Surrogate attached to stand in its home position

Stand for surrogate

To test the SLS surrogate, a stand had to be designed and built to hold the surrogate above the workspace, thereby simulating an SLS suspended from the ceiling over the surgical bed (workspace), as would be found in an OR. The SLS surrogate stand was designed using Autodesk Inventor [81] and manufactured in the Mechanical and Mechatronics Engineering Workshop at Stellenbosch University. The surrogate stand was made from mild steel and the engineering drawings of the stand can be found in Appendix D.3.

Laser beam

To simulate a light beam shining from an SLS, a 3.3 V laser beam was attached to the gimbal's pitch axis and powered by an external rechargeable lithium polymer battery.

Workspace

The workspace size was calculated to be 1 x 1 m^2, with a final grid size of four by four and each block measuring 250 mm by 250 mm. This was calculated as described in section 3.2.2, with a theta angle of less than six degrees and scaled down a third. These calculations can be seen in Appendix E.1.

Stereo vision setup

One of the engineering requirements in designing the surrogate arms was that the surrogate assembly length (*arm 1* + *arm 2* = 560 mm) should be a third of that of a surgical light; therefore, it was decided to make the work area equal to $1\ m^2$ and the height (h) equal to $1\ m$. To ensure the camera's FOV was on the workspace, it was calculated that tilting the cameras by $5°$ (θ) towards the centre with a distance of $100\ mm$ (X) from the centre was required (Figure 41). The equations used to calculate the camera tilt and distance from the centre are provided in Appendix C.1.

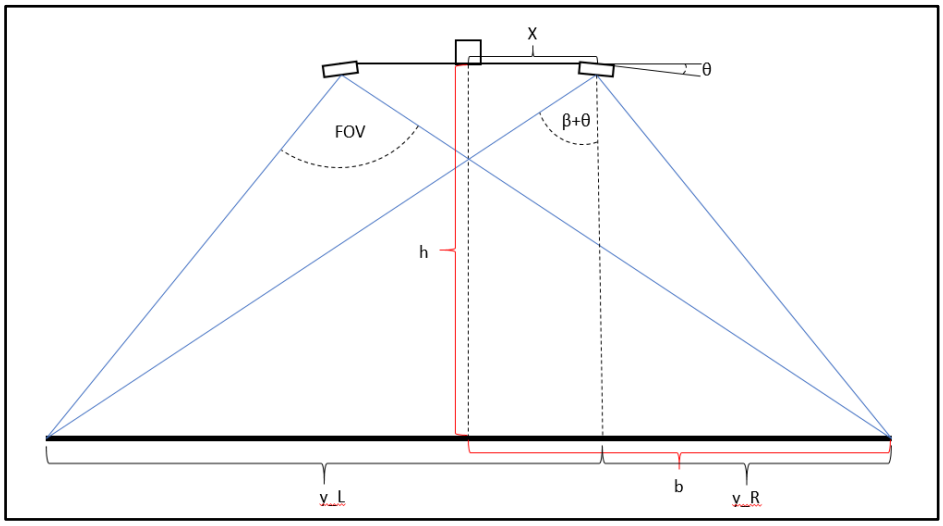

Figure 41: Setup of thermal and optical stereo cameras

After the camera setup calculations were complete, a bracket was designed and manufactured to hold the two F1G2 devices in place. The engineering drawing of this bracket was designed using Autodesk Inventor [81], and this drawing can be found in Appendix C.2. The engineering drawing was sent to FABRINOX to manufacture the bracket by laser-cutting the part out of sheet metal and bending it as needed. The bracket was made from 2 mm thick mild steel. This bracket, with the pair of F1G2 cameras, was attached to the SLS surrogate (Figure 42).

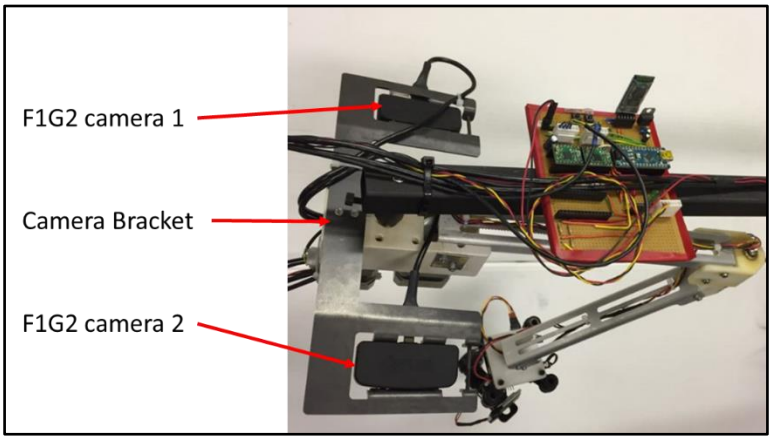

Figure 42: Bracket for the thermal and optical cameras

Initially, the cameras were attached to the surrogate stand above the centre of the workspace. However, this caused problems when the arms of the surrogate moved between one of the cameras and the object being tracked and caused the tracking algorithm to lose track of the object. This led to the decision to attach the

cameras to *bracket 1* of the SLS surrogate. Only the rotating x-axis had to be considered, because the cameras were attached to the rotating centre of *arm 1* (Figure 42). This eliminated the possibility of the assembly moving in between the cameras and the object.

A heat source for wound simulation

A heat source was required to simulate a surgical wound that could be followed by the tracking algorithm. The system cannot distinguish between similar heat sources and therefore a single heat source was used in the FOV of the cameras during testing. The required heat source used while testing the object tracking was identified during the thermal object identification process (Section 4.2.2). The normal body temperature of a human can vary from 36.1 °C to 37.2 °C [95]. The heat source was built using high-power CGS-type C10 resistors [96]. Six of these resistors were connected in series and 10 volts were run through them (Figure 43a); this caused the resistors to slowly heat up to 35 to 38°C.

During testing, a target (Figure 43b) was placed on top of the heat source, ensuring that the centre of the target was centred on the heat source. This target was required to measure the error in both the x- and y-directions. Figure 43b demonstrates the target used in the testing phase. However, this target is not to scale, as each block measures 1 x 1 cm. Therefore, this target can measure an error of up to ± 70 mm on both the x- and y-axes.

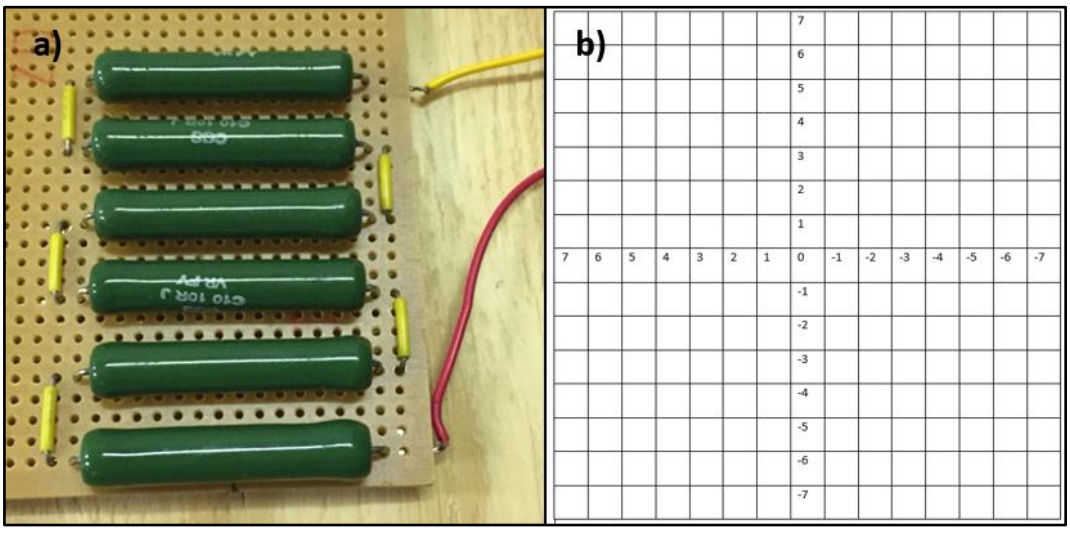

Figure 43: (a) Wound-simulating heat source and (b) target used to test SLS surrogate

4.5.3 Calibration of control system

Capture calibration images

The first step in compiling the stereo vision calibration algorithm was to capture stereo-paired images that would be used in the camera calibration process. This calibration process included calibrating each camera in the stereo pair and then calibrating the cameras as a stereo pair. The main reason for single-camera calibration was to determine each camera's matrix, which was then used in the stereo camera calibration to determine the projection matrix of the stereo-paired cameras. This projection matrix was later used in the triangulation algorithm. The image captured was a field containing a black and white chessboard grid with known parameters – the number of blocks $(4 \text{ x } 4 = 16)$ and block size $(42 \text{ mm x } 42 \text{ mm})$. An example of the chessboard used can be seen in Figure 44. Images of the chessboard were simultaneously captured by both the left and right cameras at different positions, distances and angles within the FOV of each camera. The images were stored as a joint photographic experts group (.jpg) file, and then later used in the single-camera calibration algorithm; an example of a captured stereo image pair can be seen in Figure 44.

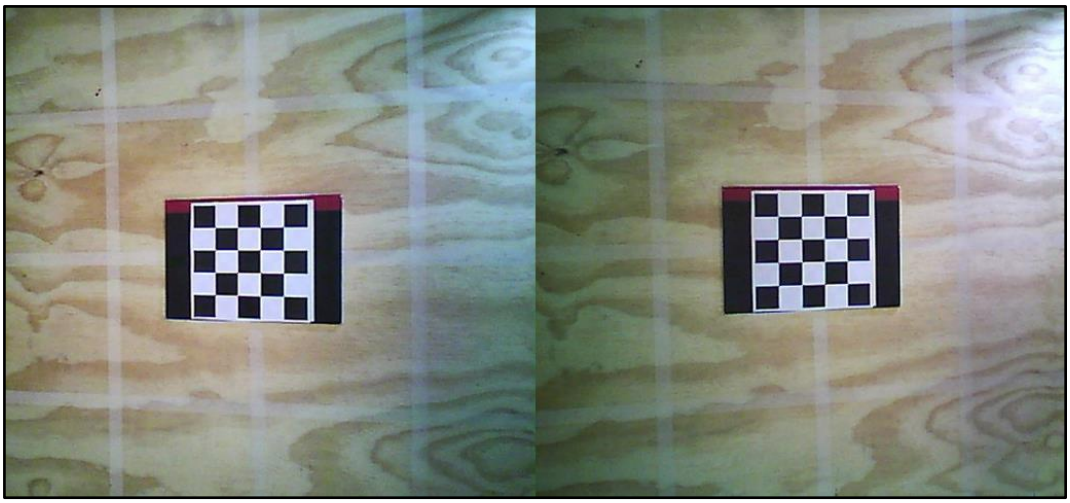

Figure 44: Left and right image pair of the chessboard captured simultaneously by the stereo-paired cameras

Single-camera calibration

In the single-camera calibration process, the captured chessboard images and the initial camera matrix were used to compute the extrinsic parameters and radial distortion coefficient and to further refine the initial camera matrix. The intrinsic parameters included the camera matrix and the radial distortion coefficient. The camera matrix, as described in section 2.3.1.1, included focal length (f) and the

principal point (P_x, P_y) (optical centre) of the camera used. The extrinsic parameters included the rotation vector and the translation vector.

The optical camera on the F1G2 has a fixed focal length (f) of $15\ cm$ ($1\ mm = 0.37795\ pixels\ \therefore 1500\ mm = 566.9\ pixels$) and an optical centre at 320 x 240 (optical/visual resolution: 640 x 480). With this information, the initial camera matrix can be described as follows:

$$K = \begin{bmatrix} 566.9 & 0 & 320 \\ 0 & 566.9 & 240 \\ 0 & 0 & 1 \end{bmatrix} \quad (4.1)$$

For camera calibration (section 2.5.2), a set of 2D image coordinates had to be known, along with their corresponding 3D world coordinates. For this reason, several images of a chessboard with known block size (3D world coordinates – object points) were captured. The function findChessboardCorners [75], from the OpenCV library, was used to locate the image points by finding the chessboard's corners. To improve the accuracy of these image points, the cornerSubPix function [75] was used. The located corners of the chessboard can be seen in Figure 45. The initial camera matrix, along with all the object points and their corresponding image points, was entered into the calibrateCamera [75] function, which returned the extrinsic parameters, radial distortion coefficients and the refined camera matrix (intrinsic parameters). Although the relative 3D position of the chessboard was not known, the calibrateCamera function [75] made use of an optimisation algorithm to minimise the re-projection error of the board's position and the intrinsic parameters ([97], [98]. Therefore, the more calibration images used, the higher the accuracy becomes; according to the literature, more than 40 images are sufficient [98]. Eighty calibration images were used in calibrating each camera. This camera calibration was done for both the left and right stereo-paired cameras. Equations 4.2 and 4.3 show the calibrated results (Camera Matrix K) for the right and left camera respectively.

Figure 45: Located corners on chessboard

$$K_R = \begin{bmatrix} 526.2 & 0 & 313.8 \\ 0 & 527.2 & 229.4 \\ 0 & 0 & 1 \end{bmatrix} \quad (4.2)$$

$$K_L = \begin{bmatrix} 533.4 & 0 & 315.7 \\ 0 & 535.0 & 221.5 \\ 0 & 0 & 1 \end{bmatrix} \quad (4.3)$$

Camera calibration improves as the re-projection error approaches zero (Equation 4.4 and 4.5 for right-and left cameras respectively) [99].

Re-projection error right = 0.368 pixels (4.4)

Re-projection error left = 0.239 pixels (4.5)

The detailed results of the camera calibration can be seen in Appendix C.3. The image points and their corresponding object points were stored, as well as the camera matrix and distortion coefficients for both the left and right camera. These were then later used in the stereo camera calibration algorithm, which is explained in the next subsection.

Calibration of stereo camera

The main purpose of this calibration process was to compute the projection matrix for both the left and right cameras for later use in the triangulation algorithm.

The object points with their corresponding left and right image points, as well as the intrinsic parameters obtained in the single-camera calibration, were entered into the stereoCalibrate function [75]. This function returned the intrinsic parameters, rotation matrix, translation vector between the coordinate systems of the left and right cameras, and the essential and fundamental matrices. This function can also perform a full-camera calibration and return the intrinsic parameters, but by using the calibrateCamera function [75], the intrinsic parameters are computed with greater accuracy [98]. Therefore, the stereoCalibrate function [75] was flagged to fix the intrinsic parameters, since they were already known. The returned parameters of the stereoCalibrate function [75] were entered into the stereoRectify function [75], which returned the projection matrices for both the left and right camera [98].

When the stereo calibration process was complete, the projection matrix for both the left and right camera was stored and later used in the triangulation algorithm. Equations 4.6 and 4.7 represent the calibrated results for right and left cameras of the stereo camera respectively.

Camera projection matrix:

$$P_R = \begin{bmatrix} 527.2 & 0 & 271.1 & 0 \\ 0 & 527.2 & 220.7 & 0 \\ 0 & 0 & 1 & 0 \end{bmatrix} \quad (4.6)$$

$$P_L = \begin{bmatrix} 527.2 & 0 & 271.1 & 143.0 \\ 0 & 527.2 & 220.7 & 0 \\ 0 & 0 & 1 & 0 \end{bmatrix} \quad (4.7)$$

The detailed results of the stereo camera calibration can be seen in Appendix C. After the stereo vision setup was complete and the stereo vision calibration algorithm had run with no major errors, the calibration was complete. The required parameters were stored and used later. The camera calibration only needed to be done whenever the cameras had been adjusted physically.

4.5.4 Mechatronic system (gimbal) calibration

To set up the STorM32 gimbal, the newest version of firmware (v0.96) was flashed onto the controller board. This firmware was the latest version available for the STorM32 boards that made use of I^2C IMU modules, and this firmware was written by OlliW [100]. The next step was to ensure that the controller board connected with the STorM32 GUI, either through USB or Bluetooth [101]. The GUI was provided online with the firmware for the controller board [102]. Lastly, the hardware setup was confirmed and a basic controller configuration setup was run. The basic controller configuration setup set the gimbal IMU orientation and the motor parameter values. The software process followed was based on online documentation [101].

After this step, the gimbal IMU's modules needed to be calibrated for optimal performance. The GUI directed the calibration process and stored the calibration values onboard the STorM32 controller board. The IMU calibration process was also based on online documentation [103]. The controller board made use of PID control to control the motors and stabilise the gimbal. During the basic controller setup, rough PID values were generated. Therefore, the next step was to finetune the PID values for better stabilisation and position control of the gimbal. Again, the GUI system directed the PID tuning, and the tuning procedure was based on online documentation [104].

5 TESTING

5.1 Data collection method

Data was collected to test the accuracy of the stereo vision, the arm translation, the head rotation and the combination of the arm translation and head rotation. Table 6 summarises how the data was collected for the different tests in terms of what was mobile, what remained stationary (at home position), what repetitions there were and what parameters were measured. Before any tests were conducted, the articulating assembly with its laser indicator was physically put in the same position, ensuring that the laser pointed to the same spot at the start of each test.

Table 6: Summary of data collection

Test	Mobile	Stationary at home position	Repetitions	Parameters measured
Stereo vision accuracy	Heat source	Surrogate arms and head	10	x, y and z, distance error
Arm translation accuracy	Surrogate arms	Surrogate head	10	x- and y-distance error, the time taken to adjust
Head rotation accuracy	Surrogate head	Surrogate arms	10	x- and y-distance error
Combined accuracy	Surrogate arms first, then head	n/a	3	x- and y-distance error, the time taken to adjust

5.1.1 Stereo vision accuracy

To test the accuracy of the stereo vision algorithm in 3D space with the stereo camera setup, its positioning at various distances was measured and compared to the actual distance; this was done on each axis in 3D space (x, y, z). To test repeatability, this process was repeated 10 times. The stereo cameras were attached to the surrogate directly above the centre of the workspace at a height of 1 m.

The measurements were taken every 50 mm, from 300 mm to -300 mm, on both the x- and y-axes, and from 0 mm to 300 mm on the z-axis. See Figure 40 for the coordinate system direction used. Initially, the target (Figure 43b) was placed in the centre of the workspace and the coordinates (x, y, z) were zeroed to mark the origin of the coordinate system. The heat source was then adjusted and measured by the stereo vision algorithm at each 50 mm interval along all the axes. Individual data points can be seen in Appendix F.1. The actual distance was measured using a ruler.

5.1.2 Arm translation accuracy

To test the accuracy and repeatability of arm translation, the arms were adjusted several times to the different positions on the workspace. The aim of testing the arm translation in isolation was to perform arm adjustments in the horizontal plane to the desired positions so that the light head would be directly above these positions. As mentioned above, these positions are the centre of the grid blocks marked out on the workspace (Figure 20). No head rotation adjustment was made, therefore the head remained in its home position (Figure 33) as the arms translated. When the light head was in its home position, the laser beam pointed perpendicularly downwards in the direction the surgical light beam would point. A target was placed at a position on the workspace to which the assembly had to translate, and this target was used to measure the accuracy in the x- and y-direction. The laser beam should ideally point to the centre of the target when the arm translation had completed by moving to the required position.

To test its accuracy, the assembly was automatically adjusted to different positions from the home position (Figure 40). This was done after one, three and five consecutive adjustments from the home position. When the adjustments were complete and the assembly was at the required position, the x and y error measurements were taken from the target (Figure 43b). This process was repeated three times to test for repeatability. The time was also recorded for one adjustment from the home position to the different positions on the workspace. Individual data points can be seen in Appendix F.2. Positions 1, 4, 13 and 16 were not recorded, since the assembly could not reach these positions. The reason for this is that the SLS surrogate could only rotate in a circular pattern and a square workspace was used.

5.1.3 Head rotation accuracy

To test head rotation in isolation, head adjustments were performed by adjusting the target while the assembly remained stationary in the home position (Figure 40). The head was adjusted to ensure the laser beam pointed at the target. The same protocol used for arm translation was used to test head rotation; however, the target was adjusted to random positions on the workspace, and this after one, three and five consecutive adjustments from the home position. In this case, the time taken to make the adjustment was not recorded. Individual data points can be seen in Appendix F.3.

5.1.4 Combined arm translation and head rotation accuracy

To test the combined head rotation and arm translation, both movements were initiated from the home position. First, the assembly translated to the required position and then the head rotated to track the heat source within the boundaries

of this position on the workspace. The same basic protocol used for arm translation was used to test head rotation; however, the target was placed randomly within the block at the various positions on the workspace. The assembly was required to translate to this position and then remain stationary while the head rotated to place the laser beam on the target. Unlike the previous tests, this process was repeated three times to test for repeatability, and the time was recorded for one adjustment from the home position. The individual data points can be seen in Appendix F.4.

5.2 Results

5.2.1 Wound tracking with stereo vision

The accuracy of a stereo camera pair tracking a moving heat source was tested on the x-, y- and z-axes. Figure 46 shows the error distribution on each axis, where the maximum error is 17 mm on the x-axis (Figure 46a) and 13 mm on both the y-axis (Figure 46b) and the z-axis (Figure 46c). Figure 47a shows the standard deviation of all the errors measured over the various measurements taken every 50 mm from 300 mm to -300 mm, and Figure 47b shows the mean error measured over the various measurements taken every 50 mm from 300 mm to -300 mm.

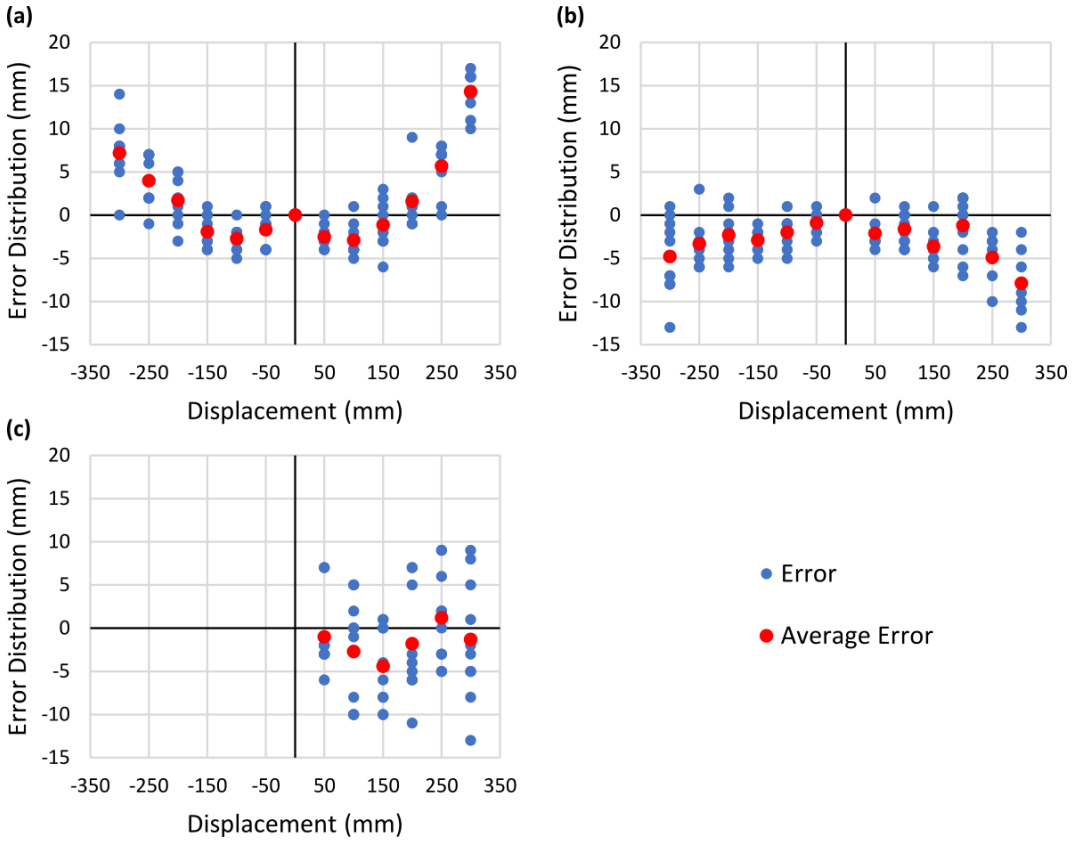

Figure 46: Accuracy of stereo vision camera pair on the (a) x-axis, (b) y-axis and (c) z-axis

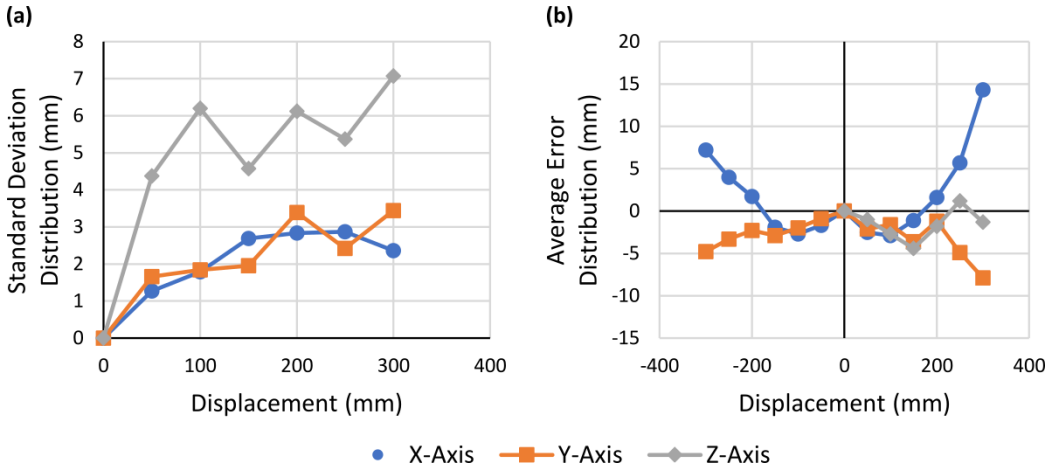

Figure 47: Results of stereo vision precision test with (a) standard deviation and (b) average error on each axis

5.2.2 Arm translation

The test of the accuracy of the arm translation revealed that most of the distortion error was found between -10 mm and +10 mm on the x-axis and between -15 mm and +10 mm on the y-axis (Figure 48), with the maximum outliers being -16 mm and -20 mm for the x- and y-axes respectively. The distribution varied depending on the number of movements; however, the negative x and negative y quadrants generally contained most of the data points. The repeatability between the three tests was acceptable, with most LA falling between -10 mm and 10 mm on the x-axis and between -15 mm and 10 mm on the y-axis.

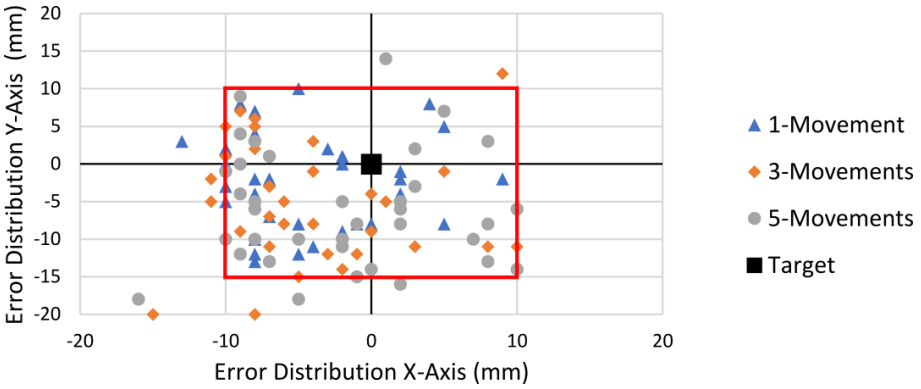

Figure 48: Accuracy of arm translation

Table 7 shows the average time it took to complete an LA from the home position to the different positions. Position 2 represented the longest average time taken to complete an LA (9.6 seconds) with only arm translation from home, while the shortest average time was position 11, with a time of 1.9 seconds. Overall, the average time was 5.7 seconds.

Table 7: Average time taken to complete an LA from arm translation

Position	Average time (s)
2	9.6
3	8.1
5	7.6
6	5.8
7	5.2
8	6.3
9	6.4
10	3.8
11	1.9
12	5.3
14	4.1
15	3.9
Average	5.7

5.2.3 Head rotation

The test of head rotation accuracy revealed that most of the distortion error was found between -10 mm and +10 mm on the x-axis and between -15 mm and +15 mm on the y-axis (Figure 49), with the maximum outliers being -15 mm and 19 mm for the x- and y-axes respectively. Figure 49 also shows the error distribution between the different consecutive adjustments from the home position.

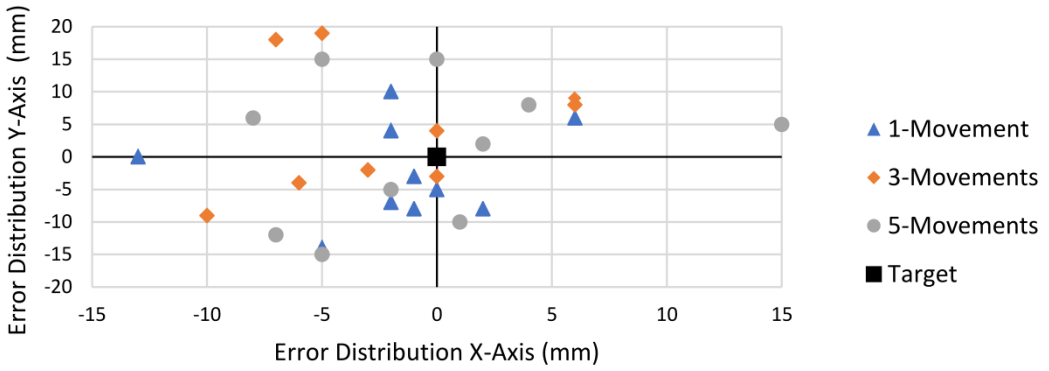

Figure 49: Accuracy of head rotation

5.2.4 Combined arm translation and head rotation

The test of the accuracy of the arm translation combined with the head rotation revealed that most of the error distortion was found between -25 mm and 25 mm in both the x- and y-directions, with no outliers (Figure 50). The maximum point in the x-direction was 22 mm, and in the y-direction it was 24 mm. The repeatability between the three tests was acceptable, with most LA falling between -15 mm and 15 mm on the x-axis and between -20 mm and 20 mm on the y-axis.

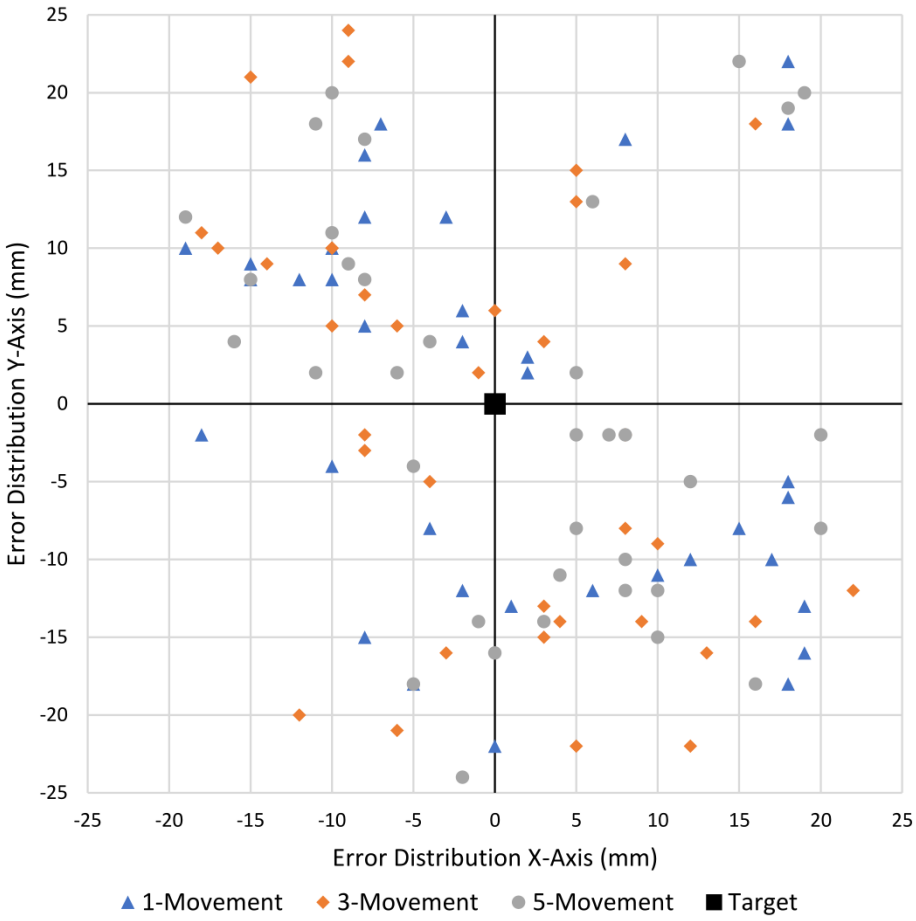

Figure 50: Combined accuracy of arm translation and head rotation

Table 8 shows the average time it took to complete an LA from the home position to the different positions, using both arm translation and head rotation. Position 2 represented the longest average time taken to complete LA (12.6 seconds), while the shortest average time was at position 11, with a time of 3.3 seconds. Overall, the average time was 8.9 seconds.

Table 8: Average time to complete an LA combining head rotation and arm translation

Position	Average time
2	12.6
3	11.3
5	12.3
6	7.9
7	9.4
8	9.1
9	9.7
10	7.1
11	3.3
12	8.5
14	8.2
15	7.2
Average	8.9

5.3 Discussion

5.3.1 Improving wound tracking with stereo vision accuracy

Testing the accuracy using the stereo vision algorithm showed that there was an error ranging from -10 mm to 15 mm at 8.7 fps; however, the surrogate and test setups were built on a smaller scale than a standard SLS. The distance from the stereo camera to the workspace in the test setup was 1 m, while in an actual OR setup the distance can range from 2.5 m to 3 m. Therefore, the potential error can be extrapolated to the real-world context (assuming it extrapolates linearly) by showing that the maximum error would be 51 mm on the x-axis and 39 mm on both the y-axis and the z-axis. Linear extrapolation was chosen because, as the distance increases, the baseline (distance between stereo pair cameras) can be physically increased (ensuring that both FOV are still overlapping at the point of interest), and this will improve depth estimation over longer distances [105]. Since the light field size (light beam) of the SLS has an average minimum diameter of 210 mm (Table 4), even the maximum error would still ensure that the light will illuminate the surgical wound (with a surgical wound being no larger than 100 mm in diameter). In addition, the standard deviation revealed that the error in depth estimation is more likely to be problematic than the error on the x- or y-axis. Therefore, the current camera setup and tracking algorithm provided sufficient accuracy to be used in an OR as a method to track the 3D position of a surgical wound in real time.

In order to improve accuracy, cameras with a higher resolution and with better quality lenses would improve the input data, while a greater FOV would allow a greater distance between the cameras. This increase in distance is helpful because it would increase the accuracy of depth estimation [105]. The stereo algorithm

could also be improved by trying to minimise the reprojection error during the calibration process.

5.3.2 Improving accuracy of arm translation

Arm translation was sufficiently accurate and generally within the time limit, but would be improved by using stepper motors with greater torque. The test results indicate that the accuracy and repeatability of arm translation were very good, even when correcting for the difference in scale between the surrogate and the actual SLS. At worst, the error would be -48 mm on the x-axis and -60 mm on the y-axis, but the surgical light would still illuminate the surgical wound because these errors were still smaller than the maximum allowed tracking error of less than 70 mm (section 3.2.1). This accuracy could be improved, however, by micro-stepping the stepper motors. Due to the torque limitation on the motors selected for the test, this was not possible in this study.

The longest time taken to complete an LA is 9.6 seconds, which is 1.8 seconds longer than the design requirements of the SLS. On the other hand, only two positions required more than the allowed time, and the overall average of 5.7 seconds is well below eight seconds. To improve on this, stepper motors with higher effective torque would be required to prevent missed steps.

5.3.3 Improving accuracy of head rotation

Head rotation was accurate, but could be improved by using another gimbal. It was evident from the testing that accuracy and repeatability of the head rotation were good because the extrapolated error for the full-size system was at most 45 mm on the x-axis and 57 mm on the y-axis. Once again, the surgical light would still illuminate the wound, since the extrapolated error was still less than the maximum allowed tracking error of below 70 mm. This accuracy can be improved by using another gimbal with better position control accuracy on each axis.

5.3.4 Combined arm translation and head rotation

The results of the accuracy tests showed that the combined movement of the assembly and head provided sufficiently accurate and repeatable results. This combined movement, however, was even slower than arm translation and would also benefit from motors with higher allowable torque. Despite this, the average time to LA was 8.7 seconds, making it only slightly slower than the requirement of 8 seconds. The scaled-up error, namely 66 mm on the x-axis and -72 mm on the y-axis, would still allow the surgical light to illuminate the wound because it is only slightly above the required allowed tracking error of 70 mm. Should the improvement suggested above be implemented, the time for LA and the error would be reduced for the combined movement as well.

6 CONCLUSION

From the literature study on the current complications with SLSs, it is quite clear that a viable solution must be found for OR SLSs. As mentioned before, an OR is a highly technical and complex working environment containing numerous items of OR equipment. The only solution found to this issue was to find a way to fully automate current SLSs. The benefits of this solution include making procedures more time efficient and hygienic, and facilitating an uninterrupted workflow for surgeons.

The main purpose of an SLS is to illuminate the surgeons' working area, which is mainly the surgical wound. From this, the objectives of the automated SLS were determined. The definitions of these objectives can be found in section 1.3.

6.1 The automated SLS surrogate was able to meet the three main objectives

To achieve full automation of the SLS, the position of the surgical wound needed to be tracked. The chosen solution was to identify a single heat source (simulating a wound) through its thermal signature by using thermal imaging cameras, and then to track the wound's position in 3D space using optical cameras with stereo vision. This will not be the case in a real-world scenario, however, and the thermal identification of the wound will have to be combined with other object-identification algorithms to improve the wound-tracking algorithm. It also has to be borne in mind that the wound-identification algorithm must be able to adapt as the surgical wound changes throughout the surgery. The position or 3D coordinates of the heat source were then used to calculate the location of the heat source in 2D space on the workspace. This information was then sent to the SLS surrogate to perform the appropriate LA. The LA was divided into two movements, namely arm translation and head rotation. The SLS surrogate arms translate to one of the regions (positions) on the workspace where the heat source is located. Thereafter, the surgical head would rotate until the light beam is pointing directly at the heat source. If the heat source is adjusted within this current position, the head would continue to rotate to ensure that the light beam is always pointing at the heat source. If the heat source moves out of the current position and into another position, the assembly would first translate to the new position and thereafter the head rotation would take over again, and so it carries on.

This study achieved its three objectives of (1) designing a control system that was able to track a heat source in 3D space, (2) designing an SLS surrogate (mechatronic system) that is analogous to the articulating arms of a standard SLS, and (3) designing a communication protocol (system communication) to manipulate the SLS surrogate to ensure that the light head of the SLS surrogate

pointed at the heat source at all times. The heat source here, however, was only adjusted and tested in 2D space by moving it along the level workspace.

It therefore can be concluded that it is possible to use thermal imaging and optical techniques to automate an SLS. This provides a foundation for future work in achieving full automation of an SLS to assist surgeons in surgical procedures.

6.2 Limitations identified during the course of the study

The aim of this project was to demonstrate that optical and thermal image tracking can be used to automate LA during surgery, although the next iteration would benefit from better quality (and therefore more expensive) components. The most critical improvement would be using thermal cameras with greater temperature resolution, since the poor resolution of the cameras necessitated tracking the highest temperature in the workspace. Since there are numerous heat sources with higher temperatures than the wound in an OR, the greater resolution would enable more specific thresholding. Further, it is suggested that the following are used: optical cameras with better lenses, increased field of view and higher resolution (which will improve depth estimation), stepper motors with increased torque (for faster arm movement), and a more precise gimbal (improved accuracy with head rotation). Also, a sturdier construction is required for better stability of the assembly.

6.3 Challenges in realising fully automated SLS

Although this project showed that optical and thermal image processing could be used for SLS automation, several challenges need to be addressed. These challenges include:

Wound identification
Since the tracking algorithm currently identifies and tracks a single heat source (simulating a wound) based only on its temperature, it is vulnerable to losing track of the wound if another object within the same temperature range enters the field of view. Therefore, it is absolutely crucial that this identification algorithm is combined with current object-identification algorithms, as mentioned in section 2.4.3.

Detection of cavity orientation
Not all deep cavities are perpendicular to the workspace and they will therefore not always be parallel to the light beam. A system therefore needs to be designed that will assist the SLS to detect cavity orientation to better illuminate this cavity.

Collision avoidance

ORs contain numerous other items of OR equipment, such as viewing screens and monitors. Current SLSs already cause disruptive and potentially painful collisions. Therefore, an automated SLS must avoid colliding with the OR equipment and surgeons/OR personnel. This will require adding sensors to the automated SLS and developing an algorithm to avoid other objects in the OR.

Compensating for beam interruption

Given the complexity of surgical workflows and the number of personnel involved, there may be times when someone steps between the light head and the wound. Therefore, the system must be able to reposition the SLS to again illuminate the wound.

6.4 Conclusion

This study set out to demonstrate that the combination of optical and thermal cameras with stereo image-processing techniques could be used to identify and track a single heat source (simulating a wound), and that it could further be used to guide an articulated assembly and gimbal (simulating an SLS) to keep a light beam pointed at the heat source. This approach is a step forward in achieving full automation of SLSs in the future, although there are still numerous changes and improvements that will have to be made to ensure that it is practically and economically viable.

7 REFERENCES

[1] Knulst AJ, Mooijweer R, Jansen FW, Stassen LP, Dankelman J, "Indicating shortcomings in surgical lighting systems," *Minimally invasive therapy & allied technologie,* vol. 20, no. 5, pp. 267-275, 2011.

[2] Knulst A.J., Stassen L.P., Grimbergen C.A. and Dankelman J., "Choosing Surgical Lighting in the LED era," *Surgical innovation,* vol. 16, no. 4, pp. 317-323, 2009.

[3] "Polaris 5xx/7xx," 2016. [Online]. Available: http://www.draeger.com/sites/en_aunz/Pages/Hospital/Polaris-5xx-7xx.aspx.

[4] Anonymous, "Lighting the Way with LED's," vol. 90, no. 3, May 2014.

[5] Matern U. and Koneczny S., "Safety, hazards and ergonomics in the operating room," *Surgical endoscopy 21,* vol. 21, no. 11, pp. 1965-1969, 2007.

[6] J. Herbert, Interviewee, *Group Procurement Executive at Mediclinic South Africa.* [Interview]. 16 02 2016.

[7] Hartmann F. and Schlaefer A., "Feasibility of touch-less control of operating room lights," *International Journal of Computer Assisted Radiology and Surgery,* vol. 8, no. 2, pp. 259-268, 2013.

[8] K. G.M., "Automated surgical illumination system". United States of America Patent US8945149B2, 11 10 2012.

[9] van As A.B., Brey Z. and Numanoglu A., "Improving operating theatre efficiency in South Africa," vol. 101, no. 7, July 2011.

[10] Kirkley A., Birmingham T.B., Litchfield R.B., Giffin J.R., Willits K.R., Wong C.J., Feagan B.G., Donner A., Griffin S.H., D'ascanio L.M. and Pope J.E, "A Randomized Trial of Arthroscopic Surgery for Osteoarthritis of the Knee," *The New England Journal of Medicine,* vol. 359, no. 11, pp. 1097-1107, 2009.

[11] Paz J.C. and West M.P., Acute Care Handbook for Physical Therapists, North Canton: Elsevier, 2014.

[12] Long M. and Rack H.J., "Titanium alloys in total joint replacement—a materials science perspective," *Biomaterials,* vol. 19, no. 18, pp. 1621-1639, 1998.

[13] "Fractures (Borken Bones)," OrthoInfo, October 2012. [Online]. Available: https://orthoinfo.aaos.org/en/diseases--conditions/fractures-broken-bones. [Accessed 26 January 2019].

[14] Wright J.M., Crockett H.C., Delgado S., Lyman S., Madsen M. and Sculco T.P., "Mini-incision for total hip arthroplasty: A prospective, controlled investigation with 5-year follow-up evaluation," *The Journal of arthroplasty,* vol. 19, no. 5, pp. 538-545, 2004.

[15] Hao L., Jia-Kuo Y., Ao Y.F., Yu C.L., Peng L.B., Lin C.Y., Zhang J.Y. and Xin F.U., "Relationship between different skin incisions and the injury of the infrapatellar branch of the saphenous nerve during anterior cruciate ligament reconstruction," *Chinese medical journal,* vol. 120, no. 13, pp. 1127-1130, 2007.

[16] Murray M.M., Spindler K.P., Abreu E., Muller J.A., Nedder A., Kelly M., Frino J., Zurakowski D., Valenza M., Snyder B.D. and Connolly S.A., "Collagen-platelet rich plasma hydrogel enhances primary repair of the porcine anterior cruciate ligament," *Journal of Orthopaedic Research,* vol. 25, no. 1, pp. 81-91, 2007.

[17] Marx R.G. and Hetsroni I., "Surgical technique: medial collateral ligament reconstruction using Achilles allograft for combined knee ligament injury," *Clinical Orthopaedics and Related Research,* vol. 470, no. 3, pp. 798-805, 2012.

[18] Hata Y, Saitoh S, Murakami N, Seki H, Nakatsuchi Y, and Takaoka K, "A less invasive surgery for rotator cuff tear: mini-open repair," *Journal of shoulder and elbow surgery,* vol. 10, no. 1, pp. 11-16, 2001.

[19] Ghodadra N.S., Provencher M.T., Verma N.N., Wilk K.E. and Romeo A.A, "Open, mini-open, and all-arthroscopic rotator cuff repair surgery: indications and implications for rehabilitation," *Journal of orthopaedic & sports physical therapy,* vol. 39, no. 2, pp. 81-89, 2009.

[20] Gigante A., Moschini A., Verdenelli A., Del Torto M., Ulisse S. and De Palma L., "Open versus percutaneous repair in the treatment of acute Achilles tendon rupture: a randomized prospective study," *Knee Surgery, Sports Traumatology, Arthroscopy,* vol. 16, no. 2, pp. 204-209, 2008.

[21] Henríquez H., Muñoz R., Carcuro G. and Bastías C., "Is percutaneous repair better than open repair in acute Achilles tendon rupture?," *Clinical Orthopaedics and Related Research,* vol. 470, no. 4, pp. 998-1003, 2012.

[22] Freedman B.A., Javernick M.A., O'Brien F.P., Ross A.E. and Doukas W.C., "Arthroscopic versus open distal clavicle excision: comparative results at six months and one year from a randomized, prospective clinical trial," *Journal of shoulder and elbow surgery,* vol. 16, no. 4, pp. 413-418, 2007.

[23] Robertson W.J., Griffith M.H., Carroll K., O'Donnell T. and Gill T.J., "Arthroscopic versus open distal clavicle excision: a comparative assessment at intermediate-term follow-up," *The American journal of sports medicine,* vol. 39, no. 11, pp. 2415-2420, 2011.

[24] de Beer J., Petruccelli D., Zalzal P. and Winemaker M.J., "Single-incision, minimally invasive total hip arthroplasty: length doesn't matter," *The Journal of arthroplasty,* vol. 19, no. 8, pp. 945-950, 2004.

[25] O'brien D.A. and Rorabeck C.H, "The mini-incision direct lateral approach in primary total hip arthroplasty," *Clinical Orthopaedics and Related Research,* vol. 441, pp. 99-103, 2005.

[26] Laskin R.S, "Minimally invasive total knee arthroplasty: the results justify its use," *Clinical Orthopaedics and Related Research,* vol. 440, pp. 54-59, 2005.

[27] Haas S.B., Cook S. and Beksac B., "Minimally invasive total knee replacement through a mini midvastus approach: a comparative study," *Clinical Orthopaedics and Related Research,* vol. 428, pp. 68-73, 2004.

[28] Vacchetti L., Lepetit V. and Fua P., "Combining edge and texture information for real-time accurate 3d camera tracking," *In Proceedings of the 3rd IEEE/ACM International Symposium on Mixed and Augmented Reality,* pp. 48-57, 2004.

[29] Pressigout M. and Marchand E., "Real-time hybrid tracking using edge and texture information," *The International Journal of Robotics Research,* vol. 26, no. 7, pp. 689-713, 2007.

[30] Ozyildiz E., Krahnstöver N. and Sharma R., "Adaptive texture and color segmentation for tracking moving objects," *Pattern recognition,* vol. 35, no. 10, pp. 2013-2029, 2002.

[31] Ning J., Zhang L., Zhang D. and Wu C., "Robust object tracking using joint color-texture histogram," *International Journal of Pattern Recognition and Artificial Intelligence,* vol. 23, no. 7, pp. 1245-1263, 2009.

[32] Zoon W.A.C., van der Hiejden M.G.M., Loomans M.G.L.C., Hensen J.L.M., "On the applicability of the laminar flow index when selecting surgical lighting," *Building and Environment,* vol. 45, no. 9, pp. 1976-1983, 2010.

[33] "OT-LIGHTS LED 5 AND LED 5," MACh, 2016. [Online]. Available: https://dr-mach.de/en/led-5-led-5.html. [Accessed 17 July 2016].

[34] "H LED Surgical light," MAQUET, 2017. [Online]. Available: https://www.maquet.com/int/products/h-led/. [Accessed 2017].

[35] "VOLISTA," MAQUET, 2017. [Online]. Available: https://www.maquet.com/int/products/volista/. [Accessed 2017].

[36] "Luvis Surgical Lights," Dentis, 2017. [Online]. [Accessed 2017].

[37] "Drager Polaris 600," Drager, 2017. [Online]. Available: https://www.draeger.com/en_uk/Hospital/Products/Medical-Lights-and-Videosystems/Operating-Lights/Polaris-600. [Accessed 2017].

[38] D. S. Erasmus, Interviewee, *Orthopaedic Surgeon - Knee Specialist.* [Interview]. 25 02 2016.

[39] D. J. Joubert, Interviewee, *Orthopaedic Surgeon - Hip Specialist.* [Interview]. 25 03 2016.

[40] Kpodonu, M.D.J., "Hybrid Cardiovascular Suite: The operating room of the future," *Journal of cardiac surgery,* vol. 25, no. 6, pp. 704-709, 2010.

[41] Lodriguss J., "How Digital Cameras Work," [Online]. Available: http://www.astropix.com/HTML/I_ASTROP/HOW.HTM. [Accessed 21 February 2017].

[42] "Microbus," [Online]. Available: http://www.microscope-microscope.org/imaging/image-resolution.htm. [Accessed 21 February 2017].

[43] "Purpose of IR Filter in Color Cameras," [Online]. [Accessed 21 Feburary 2017].

[44] Blake A., "IR Illuminators - For Better Night Vision," [Online]. Available: https://irilluminators.wordpress.com/2014/10/17/how-does-an-ir-illuminator-work/. [Accessed 21 February 2017].

[45] "IR Illuminator," [Online]. Available: http://www.camerasecuritydirect.com/tag/ir-illuminator/. [Accessed 21 February 2017].

[46] Wahl P., "The Evolution of thermal Imaging Cameras," May 2007. [Online]. Available: http://instrumentation.com/PDFS/EvolutionThermalImagingCameras.pdf. [Accessed 21 Feburary 2017].

[47] "Camera Elements," Axis Communications, 2015 December 2015. [Online]. Available: https://www.axis.com/my/en/learning/web-articles/technical-guide-to-network-video/lenses-for-thermal-cameras. [Accessed 21 Feburary 2017].

[48] "Multi Spectral Dynamic Imaging," FLIR, 2017. [Online]. Available: https://www.blue-panther.cz/data/files/funkce-msx-flir-t60-738.pdf. [Accessed January 2018].

[49] "The World's Sixth Sense," FLIR, 2018. [Online]. Available: https://www.flir.com/promotions/instruments/bfcm2018/. [Accessed January 2018].

[50] V. Karneichyk, "Infrared And Thermal Imaging Design," 23 October 2015. [Online]. Available: http://www.opticsforhire.com/blog/2015/7/15/design-of-ir-lenses. [Accessed 14 February 2017].

[51] Ghajar, Yunus A., Cengel and Afshin J., "Radiation," in *Heat and Mass Transfer*, New York, McGraw-Hill Education, 2015.

[52] Yang H. and Koyuncu S.H., "A Survey of Indoor Positioning and Object Locating Systems," vol. 10, no. 5, 2010.

[53] Ojha S. and Sakhare S., "Image Processing Techniques for Object Tracking in Video Surveillance - A Survey," vol. In Pervasive Computing (ICPC), no. 2015 International Conference on pp. 1-6, 2015.

[54] Patel M.J. and Bhatt B., "A Comparative Study of Object Tracking Techniques," vol. 4, no. 3, March 2015.

[55] Parekh H.S., Thakore D.G. and Jaliya U.K., "A Survey on Object Detection and Tracking Methods," vol. 2, no. 2, Feb 2014.

[56] Yilmar A., Javed O. and Shah M., “Object Tracking: A Survey,” vol. 38, no. 4, 2006.

[57] Hartley R. and Zisserman A., Multiple View Geometry in Computer Vision (Second Edition), Cambridge, United Kingdom: Press Syndicate of the University of Cambridge, 2003.

[58] Starr J.W. and Lattimer B.Y. , “Application of Thermal Infrared Stereo Vision in Fire Environments,” *IEEE/ASME International Conference on Advanced Intelligent Mechatronics ,* pp. 1675-1680, 2013.

[59] Prakash S., Lee P.Y. and Caelli T., “3D mapping of surface temperature using thermal stereo. In Control, Automation, Robotics and Vision,” *ICARCV'06. 9th International Conference,* pp. 1-4, 2006.

[60] Yu Z., Lincheng S., Dianle Z., Daibing Z. and Chengping Y., “Camera calibration of thermal-infrared stereo vision system. In Intelligent Systems Design and Engineering Applications,” *2013 Fourth International Conference,* pp. 197-201, 2013.

[61] Kim S.H., Jun S. and Park J., “Thermal Stereo System for Visible Range Extension of Disaster Robot,” *In 2018 IEEE International Symposium on Safety, Security, and Rescue Robotics (SSRR),* pp. 1-2, 2018.

[62] “ OpenNI documentation,” OpenNI organization , 2012. [Online]. Available: http://openni.org/Documentation. [Accessed March 2017].

[63] J. A. Girbau, “Lamp and plenum for laminar air flow ceiling”. United States Patent US20150184839A1, 2 July 2015.

[64] News Medical and Life Sciences, “Telstar develops new version of automatic surgical lighting system for laminar flow operating theatres,” 20 March 2017. [Online]. Available: https://www.news-medical.net/news/20170320/Telstar-develops-new-version-of-automatic-surgical-lighting-system-for-laminar-flow-operating-theatres.aspx. [Accessed 21 February 2019].

[65] Azbil Telstar, “Telstar incorporates a double light beam to the lighting system FlexInLight, designed for laminar flow operating theatres.,” 1 March 2017. [Online]. Available: https://www.telstar.com/readinsite/19472?language=en. [Accessed 21 February 2019].

[66] L. K.P, “Surgical lighting system”. United States of America Patent US5093769A, 03 03 1992.

[67] D. W.D., “Lighting system for medical procedures”. United States of America Patent US5526245A, 11 06 1996.

[68] Fryar C.D., Kruszon-Moran D., Gu Q., and Ogden C.L., “National Center for Health Statistics,” 20 Dec 2018. [Online]. Available: https://www.cdc.gov/nchs/data/nhsr/nhsr122-508.pdf. [Accessed 21 Feb 2019].

[69] “Powerful thermal imaging cameras designed for your smartphone,” Seek Thermal, 2017. [Online]. Available: https://www.thermal.com/compact-series.html. [Accessed 2017].

[70] FLIR, “FLIR Home,” FLIR Sytems, 2016. [Online]. Available: http://www.flir.eu/home/. [Accessed 26 07 2016].

[71] “Visual Studio Code,” Microsoft , 2018. [Online]. Available: https://code.visualstudio.com/. [Accessed 20 March 2018].

[72] G. v. Rossum, “Welcome to Python,” Python, 2018. [Online]. Available: https://www.python.org/. [Accessed 20 March 2018].

[73] “About,” OpenCV, 2018. [Online]. Available: https://opencv.org/about.html. [Accessed 14 March 2018].

[74] “Releases,” Opencv, 2018. [Online]. Available: https://opencv.org/. [Accessed 23 December 2016].

[75] O. d. Team, “OpenCV Documentation,” 10 11 2014. [Online]. Available: https://docs.opencv.org/3.0-beta/. [Accessed 11 2016].

[76] Ibraheem N.A., Hasan M.M., Khan R.Z. and Mishra P.K., “Understanding Color Models: A Review,” vol. 2, no. 3, April 2012.

[77] FLIR Systems, Inc., “FLIRONE for Android / iOS,” July 2015. [Online]. Available: https://www.flirmedia.com/MMC/THG/Brochures/IND_036/IND_036_EN.pdf. [Accessed 22 January 2017].

[78] K. Schreve, “pyMultiCam User Guide,” Stellenbosch, July 19, 2016.

[79] K. Schreve, Interviewee, *Chairman and Professor: Design and Mechatronics Division.* [Interview]. 26 March 2017.

[80] A. Salnikov, “TkInter,” Python, 17 November 2017. [Online]. Available: https://wiki.python.org/moin/TkInter. [Accessed 12 March 2018].

[81] “AutoCAD,” Autodesk , 2016. [Online]. Available: https://www.autodesk.com/education/free-software/autocad. [Accessed 30 01 2016].

[82] “Inventor,” Autodesk, 2016. [Online]. Available: https://www.autodesk.com/education/free-software/inventor-professional. [Accessed 30 01 2016].

[83] “Frequently Asked Questions,” Arduino , 2016. [Online]. Available: https://www.arduino.cc/en/Main/FAQ. [Accessed 30 06 2016].

[84] L. Badea, “Stepper Driver,” Github, 13 November 2017. [Online]. Available: https://github.com/laurb9/StepperDriver. [Accessed 9 December 2017].

[85] K. Shirriff, “Secrets of Arduino PWM,” Righto, July 2009. [Online]. Available: http://www.righto.com/2009/07/secrets-of-arduino-pwm.html. [Accessed 8 March 2018].

[86] OlliW, “Pins and Connectors,” STorM32, 6 March 2016. [Online]. Available: http://www.olliw.eu/storm32bgc-v1-wiki/Pins_and_Connectors. [Accessed 8 March 2018].

[87] “ATmega48P/88P/168P/328P,” 2017. [Online]. Available: https://www.sparkfun.com/datasheets/Components/SMD/ATMega328.pdf. [Accessed 30 06 2017].

[88] “RASPBERRY PI 3 MODEL B,” 2016. [Online]. Available: https://www.raspberrypi.org/products/raspberry-pi-3-model-b/. [Accessed 20 11 2016].

[89] “RASPBERRY PI 3 MODEL B,” Raspberry Pi, Febuary 2016. [Online]. Available: https://www.raspberrypi.org/products/raspberry-pi-3-model-b/. [Accessed March 2018].

[90] Cynfab and Thomas123, “Question about FLIR One for Android,” EEVblog, 2017. [Online]. Available: http://www.eevblog.com/forum/thermal-imaging/question-about-flir-one-for-android/?all. [Accessed 04 April 2018].

[91] “Arduino Nano,” Arduino, 2018. [Online]. Available: https://store.arduino.cc/arduino-nano. [Accessed 12 March 2018].

[92] “Download,” 02 June 2016. [Online]. Available: http://fritzing.org/home/. [Accessed 06 September 2017].

[93] “A4988 Stepper Motor Driver Carrier,” Pololu Corporation, 2018. [Online]. Available: https://www.pololu.com/product/1182. [Accessed 2018 March 12].

[94] OlliW, “Boards,” STorM32, 6 March 2016. [Online]. Available: http://www.olliw.eu/storm32bgc-v1-wiki/Boards. [Accessed 8 March 2018].

[95] L. Vorvick, “Body temperature norms,” 26 01 2017. [Online]. Available: https://medlineplus.gov/ency/article/001982.htm. [Accessed 24 10 2017].

[96] "High Power Resistors," Tyco Electronics, [Online]. Available: https://datasheet.octopart.com/1623773-2-Tyco-Electronics-datasheet-13537997.pdf. [Accessed 20 06 2017].

[97] W. Brink, "Stereo vision for simultaneous localization and mapping," Master in Engineering at Stellenbosch University, Stellenbosch, 2012.

[98] "Camera Calibration and 3D Reconstruction," OpenCV, 2014. [Online]. Available: https://docs.opencv.org/2.4/modules/calib3d/doc/camera_calibration_and_3d_reconstruction.html#getoptimalnewcameramatrix. [Accessed 2018 March 21].

[99] D. v. Heesch, "Camera Calibration," 18 12 2015. [Online]. Available: https://docs.opencv.org/3.1.0/dc/dbb/tutorial_py_calibration.html. [Accessed 20 11 2016].

[100] OlliW, "STorM32-BGC," STorM32, 6 March 2016. [Online]. Available: http://www.olliw.eu/2013/storm32bgc/. [Accessed 8 March 2018].

[101] OlliW, "Getting Started," STorM32, 6 March 2016. [Online]. Available: http://www.olliw.eu/storm32bgc-v1-wiki/Getting_Started. [Accessed 8 March 2018].

[102] OlliW, "Downloads," STorM32, 6 March 2016. [Online]. Available: http://www.olliw.eu/storm32bgc-wiki/Downloads. [Accessed 8 March 2018].

[103] OlliW, "Calibration," STorM32, 6 March 2016. [Online]. Available: http://www.olliw.eu/storm32bgc-v1-wiki/Calibration. [Accessed 8 March 2018].

[104] OlliW, "Tuning Recipe," STorM32, 6 March 2016. [Online]. Available: http://www.olliw.eu/storm32bgc-v1-wiki/Tuning_Recipe. [Accessed 8 March 2018].

[105] Kyto M., Nuutinen M. and Oittinen P., "Method for measuring stereo camera depth accuracy based on stereoscopic vision.," Espoo, Finland, 2011.

[106] A. J. Burger, "Occupancy Grid Mapping using Stereo Vision," Master of Engineering at Stellenbosch University, Stellenbosch, 2015.

[107] Alex P, J. Ball L, "Eye Tracking in HCI and Usability Research," in *Encyclopedia of Human Computer Interaction*, Liverpool John Moores University, UK, Idea Group Reference, 2006, pp. 211-218.

[108] Goldberg H.J, Wichansky A.M., "Eye Tracking in Usability Evaluation: A Practitioner's Guide.," in *The Mind's Eye: Cognitive and Applied Aspects of Eye Movement Research*, Amsterdam, Elsevier, 2003, pp. 493-516.

[109] M. Kazmeyer, "Kinds of Tracking Technology," 2017. [Online]. Available: http://smallbusiness.chron.com/kinds-tracking-technology-27692.html. [Accessed 13 March 2017].

[110] L. Turner, "An Introduction to Particle Filtering," England, 2013.

[111] K. Shirriff, "Secrets of Arduino PWM," Arduino, July 2009. [Online]. Available: https://www.arduino.cc/en/Tutorial/SecretsOfArduinoPWM. [Accessed 8 March 2018].

[112] J. P. S. Bogustaw Cyganek, An Introduction to 3D Computer Vision Techniques and Algorithms, West Sussex, United Kingdom: John Wiley & Sons Ltd, 2009.

[113] M. K. A. Centanni.

[114] S. Dhinde, S. Khedkar, A. Shaikh, A. Nadaph , "Wi Fi Based Indoor Positioning System," vol. 7, no. 5, 2017.

[115] Z. Farid, R. Nordin, M. Ismail, "Recent Advances in Wireless Indoor Localization Techniques," 2013.

[116] M. Kusner, "Method and apparatus for electronic adjustment of illuminance of surgical lamp". United State Patent US8172751B2, 8 May 2012.

[117] C. Hiltl, “Control system and method to operate an operating room lamp”. United States Patent US8817085B2, 26 October 2014.

[118] Wang J.T., “Pupil Dilation and Eye-tracking,” in *Handbook of Process-Tracing Methods*, Taipei, Psychology Press, 2009.

[119] Miller H.J., Societies and Cities in the Age of Instant Access, Utah: Springer, 2007.

[120] Eren, Webster J.G. and Halit, Measurement Instrumentation and Sensors Handbook, Florida: CRC Press, 2014.

[121] Welch G. and Bishop G., An Introduction to the Kalman Filter, Los Angeles: SIGGRAPH, 2001.

[122] Ristic B., Arulampalam S. and Gordon N., Beyond the Kalman Filter, London: Artech House, 2004.

[123] Ballard D. and Brown C., Computer Vision, New York: Prentice Hall, 1982.

[124] Chow T.T., Lin Z. and Bai W., “The intergrated effect of medical lamp position and diffuser discharge velocity on ultra-clean ventilation performance in an operating theatre,” vol. 15, no. 4, 2006.

[125] Meier C., Terzis A. and Lindenmeier S., “A robust 3D high precision radio location system,” *IEEE/MTT-S International,* pp. 397-400, 2007.

[126] Hopper A. and Hazas M., “Broadband Ultrasonic Location Systems for Improved Indoor Positioning,” *IEEE Transactions on mobile Computing,* vol. 5, pp. 536-547, 2006.

[127] Priyantha N.B., “The Cricket Indoor Location System,” *Doctoral dissertation, Massachusetts Institute of Technology,* 2005.

[128] Fukuju Y., Minami M., Morikawa H. and Aoyama T., “DOLPHIN: An Autonomous Indoor Positioning System in Ubiquitous Computing Environment,” *WSTFES,* vol. 3, p. 53, 2003.

Appendix A Research

A.1 Stereo Vision

In the following appendix, the equations used to mathematically model a single image, do corrections for radial distortion, calibrate single and stereo cameras, calculate epipolar geometry, perform image rectification and finally calculate 3D coordinates using triangulation will be provided, based on work done by Hartley and Zisserman [26].

Single camera modelling

A camera captures a single viewpoint in a 3D space (world) and projects it onto a 2D image. Here the model of a single camera is explained, and a method described to calculate this model's parameters. These parameters will differ from camera to camera [26].

The basic pinhole model is the camera model used to mathematically explain the relationship between points of an object in a 3D space and the projection of the points onto a 2D image plane. The accuracy of the basic pinhole model depends greatly on the camera used. The basic pinhole camera model and its geometry can be seen in Figure 3 [26].

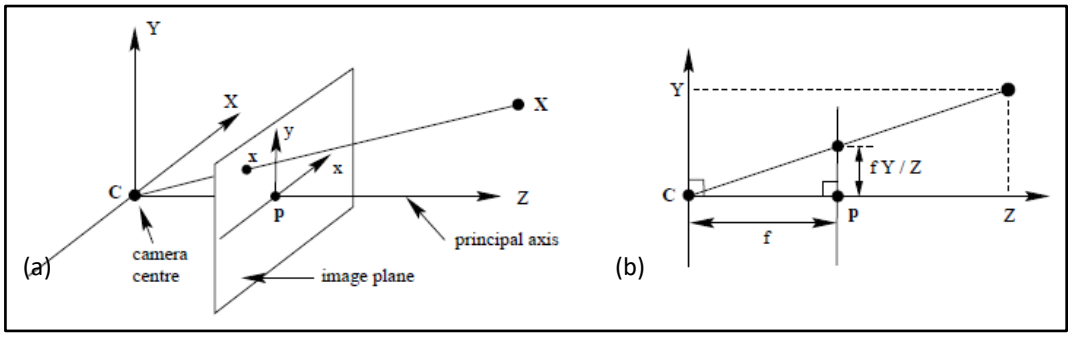

Figure 51: Pinhole camera model, (a) view of the basic model and (b) Y_c-Z_c plane of the basic model [26]

The centre of projection on the camera model is the camera/optical centre and the coordinate system at the camera centre will be denoted with a subscript c. The z-axis projected from the camera centre, that is perpendicular to the image plane, is known as the principal axis and the point where this axis intersects the image plane is known as the principal point. This principal point is in the centre of the image plane. The $Y_c - X_c$ plane through the camera centre and parallel to the image plane is known as the principal plane of the camera. The distance between

the principal plane and the image plane is known as the focal length and is denoted f [26].

When a point (X_{image}) from an object in 3D space is captured on the image plane, a line can be drawn from the camera centre to the point on the object (X), as in Figure 51. This point on an object in 3D space can be given as $X = (x_c, y_c, z_c)^T$. Using the similar triangles seen in Figure 51b one can calculate the image coordinates from the camera coordinates. The image coordinates are given as follows $X_{image} = (\frac{fx_c}{z_c} + P_x,\ \frac{fy_c}{z_c} + P_y,\ f)^T$. By ignoring the final coordinate (f), the following equation was found:

$$X_{image} = (\frac{fx_c}{z_c} + P_x,\ \frac{fy_c}{z_c} + P_y)^T \tag{A.1.1}$$

can describe a linear mapping from the world coordinates to the image coordinates where P_x and P_y are the coordinates of the principal point. The principal coordinates are equal to zero when the principal point is exactly in the centre of the image plane [26].

Homogeneous vectors were used to simplify the mapping from the world coordinates to the image coordinates. Equation A.1.1 can be expressed in homogeneous coordinates as

$$\begin{pmatrix} f_x x_c + z_c P_x \\ f_y y_c + z_c P_y \\ z_c \end{pmatrix} = \begin{bmatrix} f_x & 0 & P_x & 0 \\ 0 & f_y & P_y & 0 \\ 0 & 0 & 1 & 0 \end{bmatrix} \begin{pmatrix} x_c \\ y_c \\ z_c \\ 1 \end{pmatrix} \tag{A.1.2}$$

Let:

$$K = \begin{bmatrix} f_x & 0 & P_x \\ 0 & f_y & P_y \\ 0 & 0 & 1 \end{bmatrix} \tag{A.1.3}$$

where K is called the camera calibration matrix. Therefore, the transformation equation is described as follows

$$X_{image} = K[I|0]X_c \tag{A.1.4}$$

With this, the assumption is made that the camera is located at the centre of the Euclidean coordinate system, that the camera's principal axis is pointing exactly down the z-axis and, that X_{image} is expressed in the same coordinate system as the camera and can be known as the camera coordinate frame [26]. The following will have an influence on the final projection matrix:

Rotation and Translation

The world coordinate frame/system will be expressed in a different Euclidean coordinate frame than that of the camera coordinate frame. To fit the camera coordinate frame to the world coordinate frame rotation and translation may be required. The world coordinate frame is denoted with a subscript w. Rotating and translating a point (X_c) in the form of Euclidean coordinate gives $X_c = R(X_w - C)$, where R is a 3 X 3 matrix representing the orientation of the camera coordinate frame and C represents the camera centre's coordinates in the world coordinate frame. The equation can also be expressed in the homogeneous coordinates as

$$\begin{pmatrix} x_c \\ y_c \\ z_c \\ 1 \end{pmatrix} = \begin{bmatrix} R & -RC \\ 0 & 1 \end{bmatrix} \begin{pmatrix} x_w \\ y_w \\ z_w \\ 1 \end{pmatrix} \tag{A.1.5}$$

Scaling

The underlying assumption of the pinhole camera model presupposes that the image coordinates have equal scales in both axial directions. However, when using CCD (charge-coupled device) cameras there is a possibility of having non-square pixels. To adjust non-square pixels in the image coordinates, scaling factors are introduced for the X_{image} and Y_{image} directions. To overcome this, the calibration matrix is adjusted by multiplying the scaling factors (m_x and m_y) as follows

$$K = \begin{bmatrix} m_x & 0 & 0 \\ 0 & m_y & 0 \\ 0 & 0 & 1 \end{bmatrix} \begin{bmatrix} f_x & 0 & P_x \\ 0 & f_y & P_y \\ 0 & 0 & 1 \end{bmatrix} = \begin{bmatrix} \alpha_x & 0 & x_0 \\ 0 & \alpha_y & y_0 \\ 0 & 0 & 1 \end{bmatrix} \tag{A.1.6}$$

where $\alpha_x = f_x m_x$, $\alpha_y = f_y m_y$, $x_0 = P_x m_x$, and $y_0 = P_y m_y$.

Skew Parameter

The skew parameter (s) will be zero for most normal cameras but is non-zero when allowing for slightly skew pixels. The skew parameter is added into the calibration matrix as follows

$$K = \begin{bmatrix} \alpha_x & s & x_0 \\ 0 & \alpha_y & y_0 \\ 0 & 0 & 1 \end{bmatrix} \tag{A.1.7}$$

Finally, after taking the above-mentioned points into consideration the transformation equation of a point on an object to an image plane can be described as follows in homogeneous coordinates

$$\begin{pmatrix} x_{image} \\ y_{image} \\ 1 \end{pmatrix} = P \begin{pmatrix} x_w \\ y_w \\ z_w \\ 1 \end{pmatrix} \tag{A.1.8}$$

where

$$P = KR[I|-C] \tag{A.1.9}$$

P is known as the camera projection matrix [26].

Single camera calibration

In this subsection, the camera projection matrix (P) is found through a calibration process for a specific camera. The P matrix can be estimated if several 2D image coordinates and their corresponding 3D world coordinates are known [26]. Let $i = 1,2,\dots,n$ equal to the number of points. Then ith number of image coordinates are $X_{i,image} = (x_{i,image} \quad y_{i,image} \quad 1)^T$ and the corresponding world coordinates are $X_{i,w} = (x_{i,w} \quad y_{i,w} \quad z_{i,w} \quad 1)^T$. If the j-th row of the camera projection matrix is denoted by p^{jT}, then the transform equation is described as follows

$$X_{i,image} = PX_{i,w} = \begin{pmatrix} p^{1T}X_{i,w} \\ p^{2T}X_{i,w} \\ p^{3T}X_{i,w} \end{pmatrix} \tag{A.1.10}$$

This equation involves homogeneous vectors and therefore the vectors $X_{i,image}$ and $PX_{i,w}$ are not strictly equal because their direction is the same, but they can differ in magnitude. By expressing equation A.1.10 as a vector cross product $X_{i,image} \times PX_{i,w} = 0$, this form will allow for a linear solution for P. Since $p^{jT}X_{i,w} = X_{i,w}^T p^j$ for $j = 1,2,3$ … this will lead to three sets of equations in the entries of P and can be described as follows

$$\begin{bmatrix} 0^T & -X_{i,w}^T & y_{i,image}X_{i,w}^T \\ X_{i,w}^T & 0^T & -x_{i,image}X_{i,w}^T \\ -y_{i,image}X_{i,w}^T & x_{i,image}X_{i,w}^T & 0^T \end{bmatrix} \begin{pmatrix} p^1 \\ p^2 \\ p^3 \end{pmatrix} = 0 \tag{A.1.11}$$

Equation 2.11 has the from $M_i P = 0$ and since one of the three equations in this equation is not linearly independent, this equation can reduce to

$$\begin{bmatrix} 0^T & -X_{i,w}^T & y_{i,image}X_{i,w}^T \\ X_{i,w}^T & 0^T & -x_{i,image}X_{i,w}^T \end{bmatrix} \begin{pmatrix} p^1 \\ p^2 \\ p^3 \end{pmatrix} = 0 \tag{A.1.12}$$

Since the camera projection matrix (P) has 11 degrees of freedom, 11 equations are required to solve this matrix. Each point correspondence can solve two equations, therefore, a minimum of 6 correspondences are required to solve for the P matrix [26].

Radial distortion

Radial distortion is visible in images of objects containing vertical lines and consequently, the vertical lines appear distorted (see Figure 52). This is caused when light travels through the lens since it bends (distorts) due to refraction. In the camera model used, it was assumed that light travels in a straight line; therefore this distortion of the light needs to be accounted for [26].

To overcome distortion the correct image measurements must be used as obtained from a perfect linear camera action. With pixel coordinates, the following equation is used to compute the corrected image coordinates

$$\begin{pmatrix} x_{image} \\ y_{image} \end{pmatrix} = \begin{pmatrix} x_c \\ y_c \end{pmatrix} + L(r) \begin{pmatrix} x_m - x_c \\ y_m - y_c \end{pmatrix} \quad \text{(A.1.13)}$$

Where X_{image} is the corrected image coordinates, X_c is the centre of the radial distortion and X_m is the measured coordinates. $L(r)$ is a distortion factor with $r^2 = (x_m - x_c)^2 + (y_m - y_c)^2$ which is the distance to the centre of radial distortion [26].

Figure 52: Example photograph before (a) and after (b) radial distortion correction [26]

The distortion function is described with a Taylor expansion $L(r) = 1 + k_1 r + k_2 r + k_3 r + \cdots$. The coefficients of this distortion function $(k_1, k_1, k_1, \ldots, x_c, y_c)$ are part of the internal calibration of the camera. The principle point is often used as the distortion point [26].

Stereo camera modelling

With two cameras, the world coordinates (x, y, z) of a point on an object can be located if image coordinates (x, y) of this point from both cameras are known. This section describes epipolar geometry, how to calibrate two cameras to locate

world coordinates from triangulating image coordinates, and with image rectification. In this section, L and R subscripts will indicate the left and right cameras respectively [26].

Stereo camera calibration

Calibrating stereo cameras requires finding the camera's projection matrices P_L and P_R. These matrices and their values depend on the type of cameras used and their setup geometries relative to each other. These projection matrices can be obtained when both cameras simultaneously capture an image of a single object of known geometry [26].

Epipolar geometry

Epipolar geometry (stereo vision geometry) is the geometry of a single point in 3D space view by two images (Figure 53). This epipolar geometry is used to search for correspondence points in stereo matching [26].

In Figure 53 X_r is a single point in 3D space and is mapped onto the two image planes as x_R and x_L, also c_R and c_L are the camera centres. The line connecting the camera centres is known as the baseline and is denoted with a a. Point e_R and e_L are points on the image planes where the baseline intersects – this is called the epipole. An epipolar plane is a plane drawn from the camera centres to the point X. l_R, the epipolar line, is the intersection of the epipolar plane on the image plane. This epipolar geometry acts as epipolar constraints that minimize the search for the corresponding points in the images from the entire image plane to one single line [26].

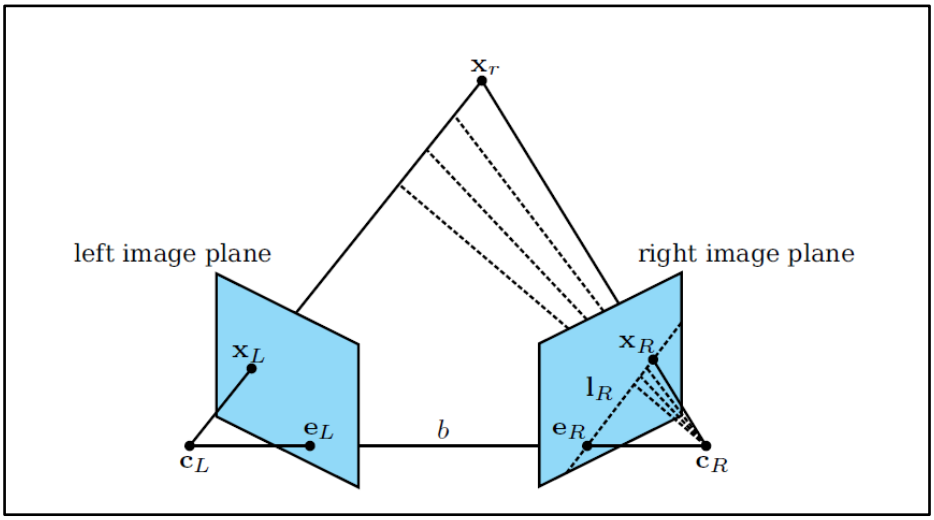

Figure 53: Epipolar geometry with image (a) demonstrating the epipolar plane and image (b) the epipolar line from x [92]

The following equation describes the correspondence search of two image points

$$x^T{}_L F x = 0 \tag{2.14}$$

where F is called the fundamental matrix and it is the algebraic representation of the epipolar geometry. Searching for image correspondence pairs and then calculating their 3D coordinates in 3D space using triangulation can be simplified through image rectification [26].

Image rectification

Image rectification is the process of resampling 2D image pairs of stereo images to achieve a better image pair where the epipolar lines run parallel with the x-axis (baseline) and so the disparity is only in the x-direction (Figure 54) [26]. The cameras are physically not always exactly aligned or tilted the same therefore the image pairs need to be rectified.

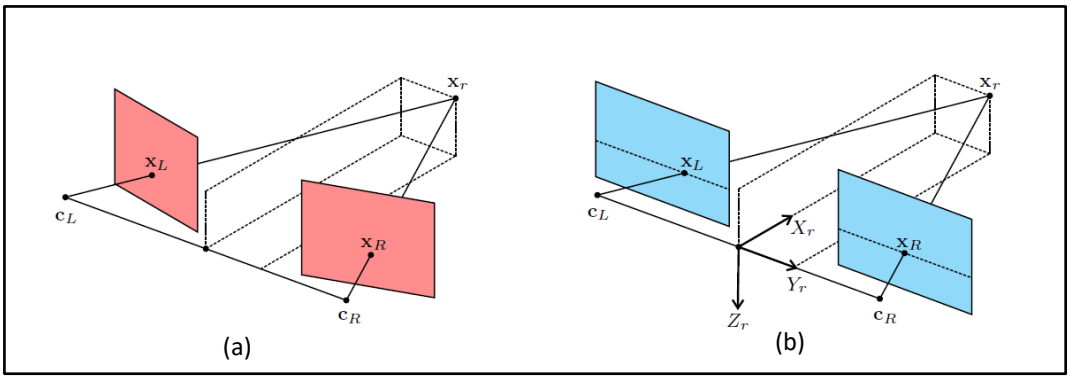

Figure 54: Image rectification of image pair, showing (a) unrectified image pair and (b) the rectified image pair [92]

The unrectified camera projection matrices (equation 2.9) pairs are described as follows for both the left and right cameras

$$P_R = K_R R_R [I|-C_R] \tag{A.1.15}$$

$$P_L = K_L R_L [I|-C_L] \tag{A.1.16}$$

The new rectified camera projection matrices can be described as

$$P_{nR} = K_{nR} R_{nR} [I|-C_R] \tag{A.1.17}$$

$$P_{nL} = K_{nL} R_{nL} [I| - C_L] \tag{A.1.18}$$

With both the rectified and unrectified camera projection matrices the calibration matrices (K_n) and the orientation matrix (R_n) relative to the world coordinate frame remains unchanged. The only difference between the two camera projection matrices is the camera centres (C). The new calibration matrix is chosen as an average $K_n = 0.5(K_R + K_L)$, and the new rotation matrix is chosen so that it is aligned with the vector between the camera centres [92, 101].

This result of image rectification is that any point in 3D space that is projected onto two rectified image planes will have the same y_{image} coordinates and two different x_{image} coordinates. The difference in the two x_{image} coordinates along with the single y_{image} coordinate can be triangulated to calculate the coordinates of the point in 3D space [92, 101]. This image rectification improves correspondence matching accuracy and computational speed [27, 29].

Triangulation

Triangulation is used to calculate the desired 3D coordinates of a point in 3D space $[x_r\ y_r\ z_r]^T$, from a known pair of corresponding 2D image coordinates pairs. $[x_L\ y_L]^T$, $[x_R\ y_R]^T$ for the left and right image respectively. Let $y_L = y_R = y$ because after image rectification the y_{image} coordinates will remain constant. Once image rectification has been done, similar triangles can be used to triangulate the desired 3D coordinate [92, 101]. The geometry of this triangulation is shown in Figure 55.

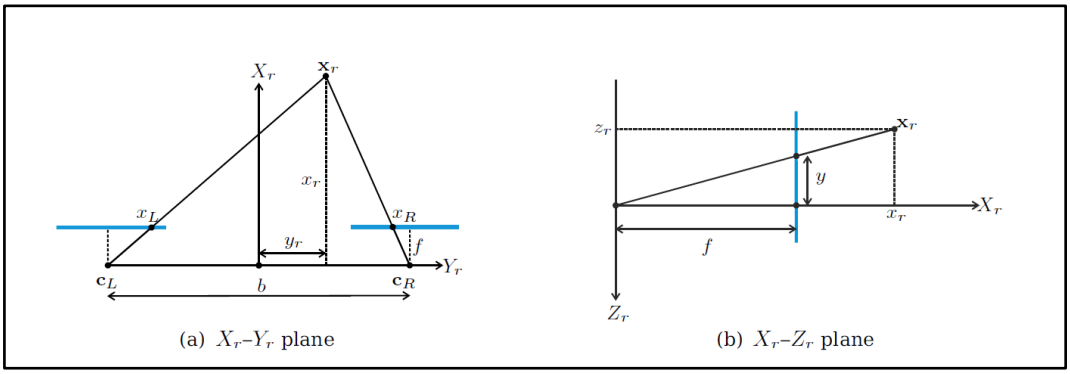

Figure 55: Triangular geometry using corresponding image coordinates to calculate the projected point in 3D space [92]

Using the geometry depicted in Figure 55a and similar triangles, the following equations can be formulated

$$\frac{f}{x_L} = \frac{x_r}{\frac{b}{2}+y_r} \text{ and } \frac{f}{x_R} = \frac{x_r}{-\frac{b}{2}+y_r} \qquad \text{(A.1.19)}$$

Introducing the principal point, the above equations can be rewritten as

$$x_r = \frac{(x_L - P_x)b}{x_L - x_R} - \frac{b}{2} \text{ and } y_r = \frac{(y - P_y)b}{x_L - x_R} \quad \text{(A.1.20)}$$

where b is the length of the baseline and f is the focal length of the cameras. Using the geometry depicted in Figure 55b and similar triangles, the same can be done to calculate the z coordinate [92, 101].

$$z_r = \frac{fb}{x_L - x_R} \quad \text{(A.1.21)}$$

A.2 3D Positioning Technologies

A.2.1 Radio frequency position tracking

Radio frequency (RF) is positioning technology used in short, medium and long-range object identification and navigation for both indoor and outdoor applications. The radio wave spectrum is part of the electromagnetic (EM) spectrum (Figure 8). The radio wave spectrum is large, and the behaviour of these waves depends on their wavelengths and corresponding frequencies [19]. Various positioning systems make use of RF in the radio wave spectrum.

Global positioning system (GPS)

Global position systems (GPS) make use of the time differences of signals sent from four or more satellites in the Earth's orbit. The GPS device will receive signals emitted by the GPS satellite. The satellites send very accurate time delay signals that the GPS device can use to calculate, through trilateration, the global position of the GPS device [20]. GPS is commonly used because of its high accuracy from 1-5 m, with a global range. The cost, however, is quite high and the limitation to GPS is that it does not work well indoors. However, high sensitivity GPS can be used for some indoor applications, but signal accuracy is lost due to signal reflections caused by, for example, buildings [11].

Radio frequency identification (RFID)

RF identification is a positioning system that consists of an antenna able to send and receive radio signals and a chip that receives and stores the broadcast information. RIFD tags in known positions receive radio waves to pinpoint and track the RFID emitter attached to objects being tracked. Direction and range of the object being tracked can be determined [21]. The limitation to RFID is that inaccuracy can be caused by signal propagation and the surrounding environment. These limitations can be overcome by using integrating systems improving the positioning accuracy. The accuracy of RFID is 1-2 m. It can be used indoor and costs vary from low to moderate depending on the specific system used [11].

Ultrawideband (UWB)

Ultrawideband is a positioning system ideal for indoor tracking application since the surrounding environment does not affect the accuracy. UWB systems transmit signals sequentially in short impulses and receivers placed in known positions receive these signals. Then a system will evaluate these signals and estimate the time of arrival of the impulse signals to calculate the transmitter's position. This system can be used in real-time applications with a data rate of 1 Hz, is accurate up to 10 cm, it has a 15 m range and moderate cost [11].

Radar

Radar navigation is another RF-based positioning system that makes use of emitted RF pulses from a known position and the echo of the pulses returning from a target to calculate the distance between the emitted source and the target [20]. Radar is mostly used in long-range outdoor applications but can also be adapted to be used for short-range indoor applications. For instance, a system could locate an object by processing the signal strength received from three or more emitters through triangulation. A system like this will have an accuracy of 2-3 m and the cost of the system is moderate [11].

Other radio frequency positioning systems

Other positioning systems that make use of RF were not considered because their accuracies were greater than 3 m which make them unsuitable for tracking applications in an OR [11].

A.2.2 Ultrasonic position tracking

Active bat

The active bat is an ultrasonic location system used for indoor applications. The target object is equipped with a badge/tag that periodically emits an ultrasonic signal to several network receivers attached to the ceiling of the environment [11, 22]. This system, alongside the receivers' known orientation and position, can calculate the emitter's/object's three-dimensional position through the pulses' time of flight to a great accuracy of 3-7 cm. The limitation to this method is the number of receivers required and the positioning of these receivers. The cost involved for this system is moderate, it can be used in real-time tracking with a data rate of 75 Hz [11, 22].

Cricket

The cricket is another ultrasonic positioning system used in indoor applications [11, 23]. It is a sensor that can either act as a stationary or mobile beacon. The beacons emit and receive periodical ultrasonic signals containing beacon-specific information. A beacon uses information from stationary beacons within the

surrounding environment and uses these known distances to calculate its position [23]. The cricket system can be used for three-dimensional positioning in a real-time application with a data rate 1 Hz, has a high accuracy of 1-2 cm, a good range of 10 m and low cost [11].

Dolphin

Distributed object locating system for physical-space internetworking (Dolphin) is an ultrasonic positioning system. This system makes use of distributed wireless sensors that emit and receive RF and ultrasonic signals to determine the distance between the sensors. These sensors are distributed in the surrounding environment. A few of these sensors are required to be preconfigured at known positions as reference stations. Other sensors are located through an iterative positioning algorithm [11, 24]. The dolphin system can be used for tracking objects indoor in real-time with a data rate of 20 Hz, with high accuracy of up to 2 cm, with a moderate range of about 4 m and moderate cost [11].

A.2.3 Wi-fi position tracking

Wi-Fi signals can be used to calculate the distance between the transmitter (like a wi-fi router) and the receiver (like a mobile phone). If a wi-fi enabled mobile device receives more than three wi-fi signals from wi-fi routers in known positions, the mobile device can be located through a triangulation algorithm. This triangulation algorithm uses the wi-fi signal's angle of arrival (AOA), time of arrival (TOA) and the received signal strength (RSS) to calculate the distance from the device to the router [25]. This method has an accuracy up to 1 m, with a range of about 10 m and low cost [26].

Appendix B Documents

B.1 Positioning survey

THEATRE LIGHT POSITIONING SURVEY

Survey Date: _____

SURVEY DONE BY: ____JARRYD_BURGER____

LIGHT POSITIONING SURVEY

1. Light Positioning Survey Description

The following is observation survey on light positioning during an operation. In this survey the light positioning done during an operation by the surgeon or medical personal will be observed and documented. The purpose of the survey is to discover current problems and hazards of surgical lighting systems.

Type of operation: _____

Operation duration: _____

2. Light Positioning

2.1 Diagram

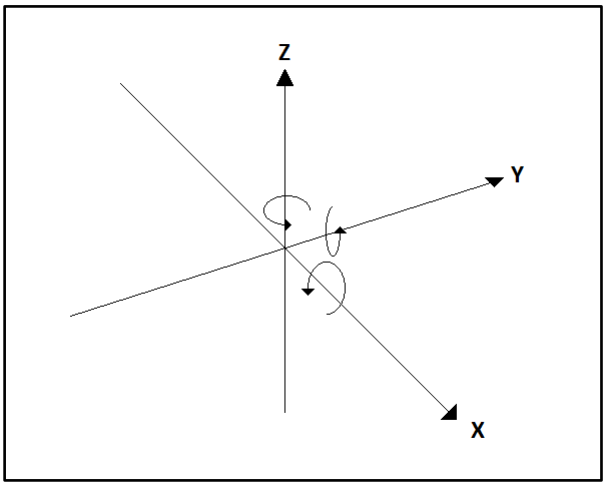

Figure 56: Position axis of theatre light

Diagram above represents the directions that the theatre light can move. The length of the bed will be in the x-axis direction during the survey.

2.2 Positioning

	Surgeon:		Medical Personal:	
	Single:	Combination:	Single:	Combination:
Translation:				
Along x-axis				
Along y-axis				
Along z-axis				
Along horizontal plane (x- and y-axis)				
Along vertical plane (x and z-axis)				
Along vertical plane (y and z-axis)				
Rotation:				
Around x-axis				
Around y-axis				
Around z-axis				

2.3 Light Positioning Time:

Positioning time duration: _____ Positioning time duration: _____

Positioning time duration: _____ Positioning time duration: _____

Positioning time duration: _____ Positioning time duration: _____

Positioning time duration: _____ Positioning time duration: _____

Positioning time duration: _____ Positioning time duration: _____

Positioning time duration: _____ Positioning time duration: _____

Positioning time duration: _____ Positioning time duration: _____

Positioning time duration: _____ Positioning time duration: _____

3. Notes

_____

_____

_____

_____

_____

_____

_____

_____

APPROVAL OF SURGEON

Surgeon who approved authorization for theatre visit.

Name	Title	Date

_____ _____

Complete by: Date:

Appendix C Algorithm Design

C.1 Thermal and optical stereo camera setup calculations

Thermal and Optical Camera Setup:

Setup Diagram:

Thermal and Optical Camera Setup:

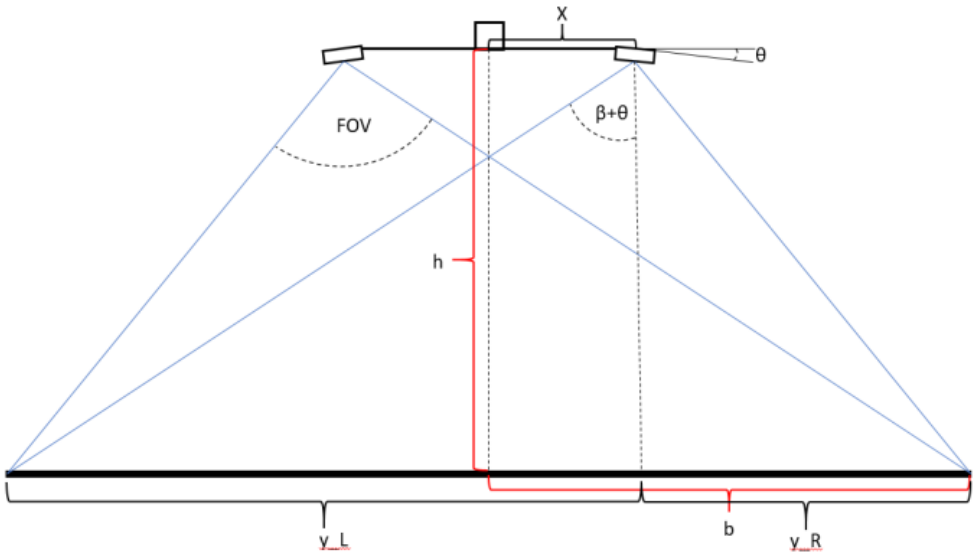

Field of wiew: $FOV := 53\ deg$

Base: $b := 500\ mm$

Height: $h := 1000\ mm$

Take θ as: $\theta := 5\ deg$

$\beta := \frac{FOV}{2} = 26,5\ deg$

$\alpha\_L := \beta + \theta = 31,5\ deg$

$\alpha\_R := \beta - \theta = 21,5\ deg$

$y\_L := h \cdot \tan(\alpha\_L) = 612,8\ mm$

$y\_R := h \cdot \tan(\alpha\_R) = 393,9\ mm$

$x := y\_L - b = 112,8\ mm$

Answer should be as close to zero as possible: $zero := b - y\_R - x = -6,7\ mm$

Therefor take: x = 100 mm

θ = 5 degrees

C.2 Camera bracket drawing

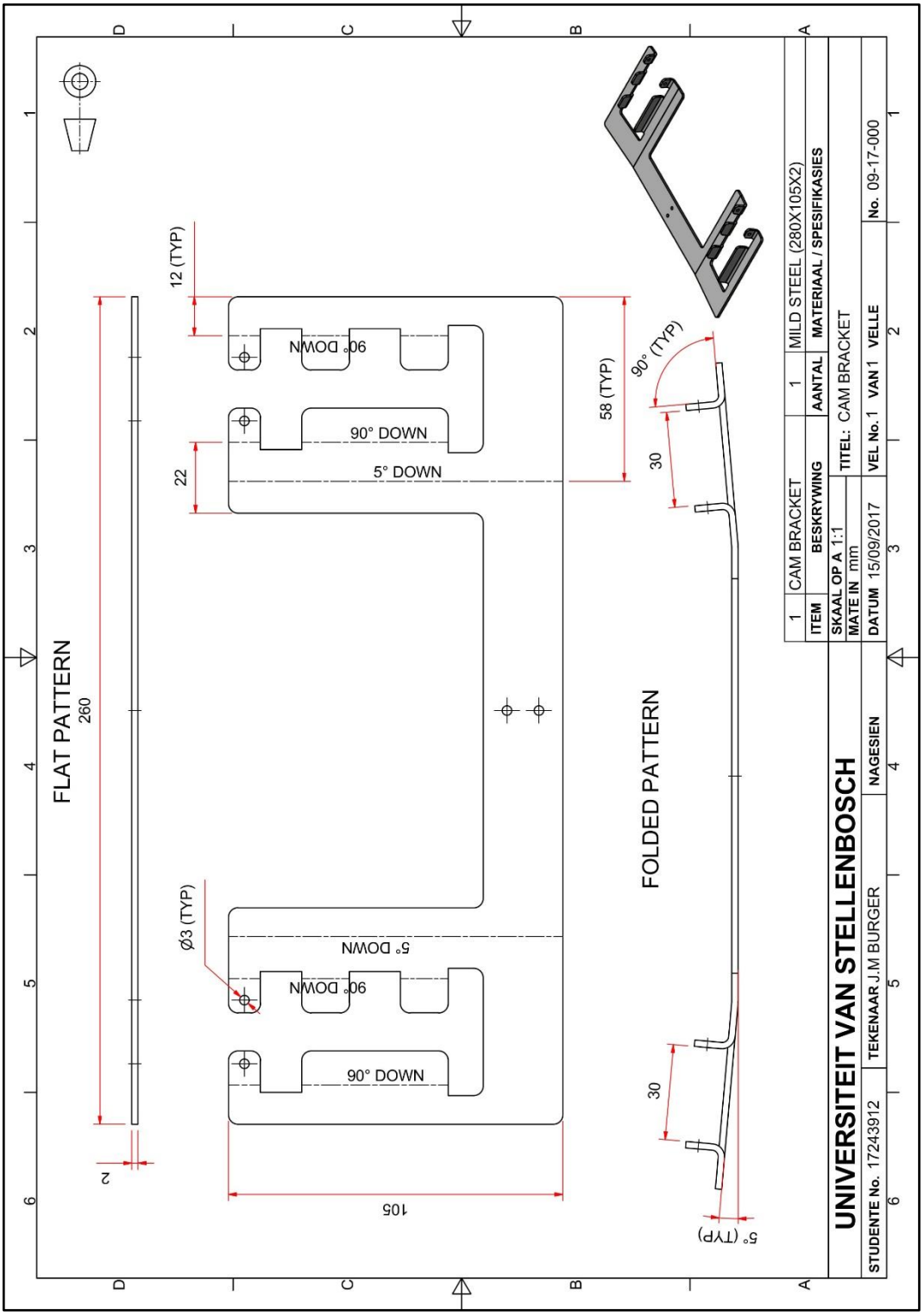

C.3 Single camera calibration results

Right camera calibration results:

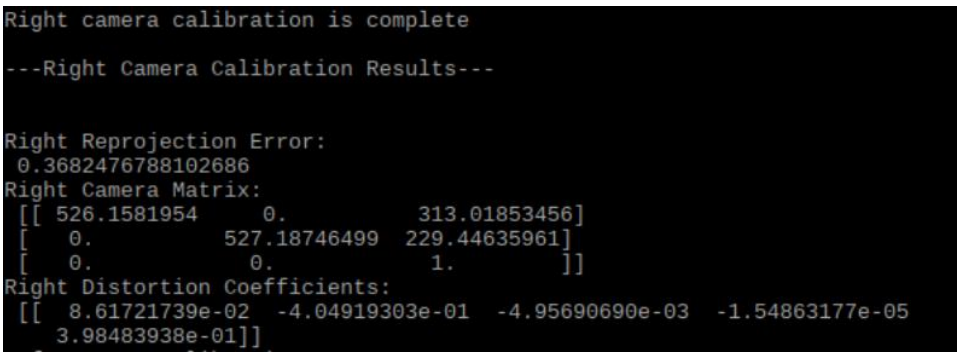

Left camera calibration results:

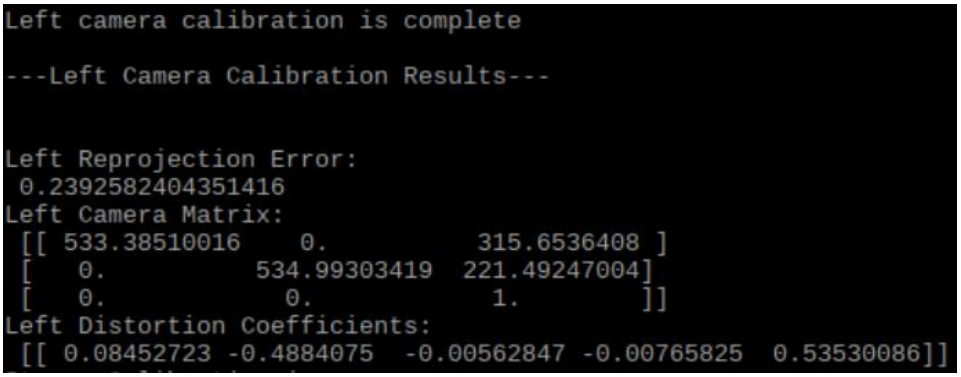

C.4 Stereo camera calibration results

```
---Stereo Camera Calibration Results---


Left Camera Matrix:
 [[ 533.38510016    0.          315.6536408 ]
 [   0.          534.99303419  221.49247004]
 [   0.            0.            1.        ]]
Right Camera Matrix:
 [[ 526.1581954     0.          313.01853456]
 [   0.          527.18746499  229.44635961]
 [   0.            0.            1.        ]]
Rotation Matrix:
 [[  8.79640680e-01   2.06140187e-02  -4.75191893e-01]
 [ -2.31378135e-02   9.99732140e-01   5.37751262e-04]
 [  4.75075694e-01   1.05218735e-02   8.79882024e-01]]
Translation Vector:
 [[ 259.48273334]
 [  -2.24879965]
 [  79.15010616]]
Essential matrix:
 [[   0.76301034  -79.15256663   -2.02124145]
 [ -53.65028632   -1.09864273 -265.92568129]
 [  -4.02572744  259.45958518   -0.92907419]]
Fundamental Matrix:
 [[ -8.06847922e-08   8.35367406e-06  -1.77900486e-03]
 [  5.65621692e-06   1.15601046e-07   1.29542865e-02]
 [ -1.00027794e-03  -1.72681975e-02   1.00000000e+00]]
Rotation matrix for right camera:
 [[  9.80134895e-01   1.44993057e-02  -1.97801307e-01]
 [ -1.48776977e-02   9.99889230e-01  -4.26948864e-04]
 [  1.97773206e-01   3.36129553e-03   9.80242042e-01]]
Rotation matrix for left camera:
 [[  9.56458993e-01  -8.28912436e-03   2.91749011e-01]
 [  7.72758980e-03   9.99965408e-01   3.07701081e-03]
 [ -2.91764424e-01  -6.88517984e-04   9.56489962e-01]]
Projection matrix for right camera:
 [[ 527.18746499    0.          271.09367085    0.        ]
 [   0.          527.18746499  220.65770912    0.        ]
 [   0.            0.            1.            0.        ]]
Projection matrix for left camera:
 [[  5.27187465e+02   0.00000000e+00   2.71093671e+02   1.43023429e+05]
 [  0.00000000e+00   5.27187465e+02   2.20657709e+02   0.00000000e+00]
 [  0.00000000e+00   0.00000000e+00   1.00000000e+00   0.00000000e+00]]
ROI for right camera:
 (0, 9, 466, 438)
ROI for left camera:
 (147, 29, 493, 420)
Stereo camera calibration is complete
```

Appendix D SLS surrogate design

D.1 SLS's surrogate drawings

These engineering drawings are the drawings of the translation assembly of the SLS surrogate.

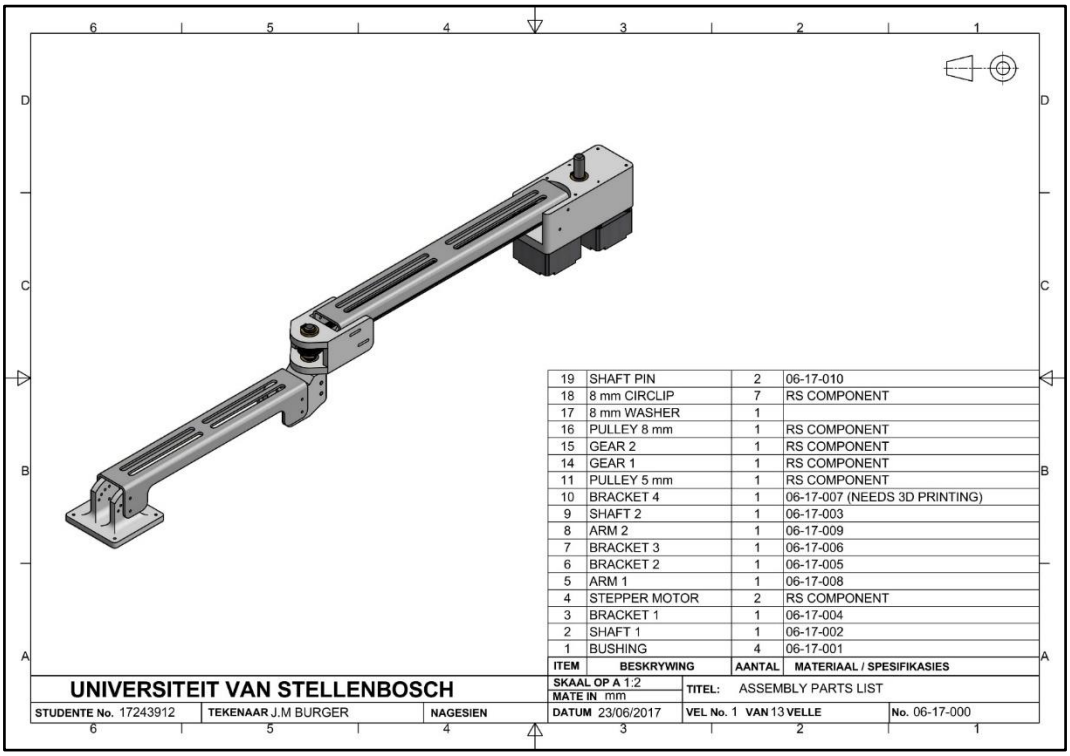

Figure 57: Assembly parts list

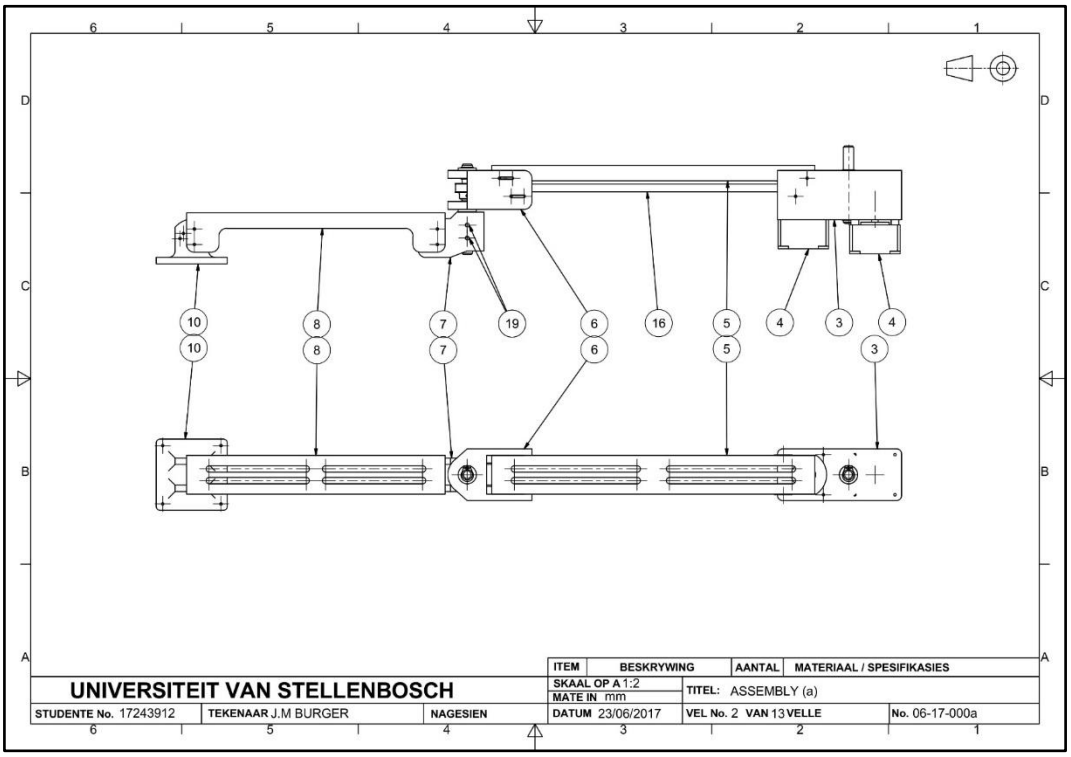

Figure 58: Assembly (a)

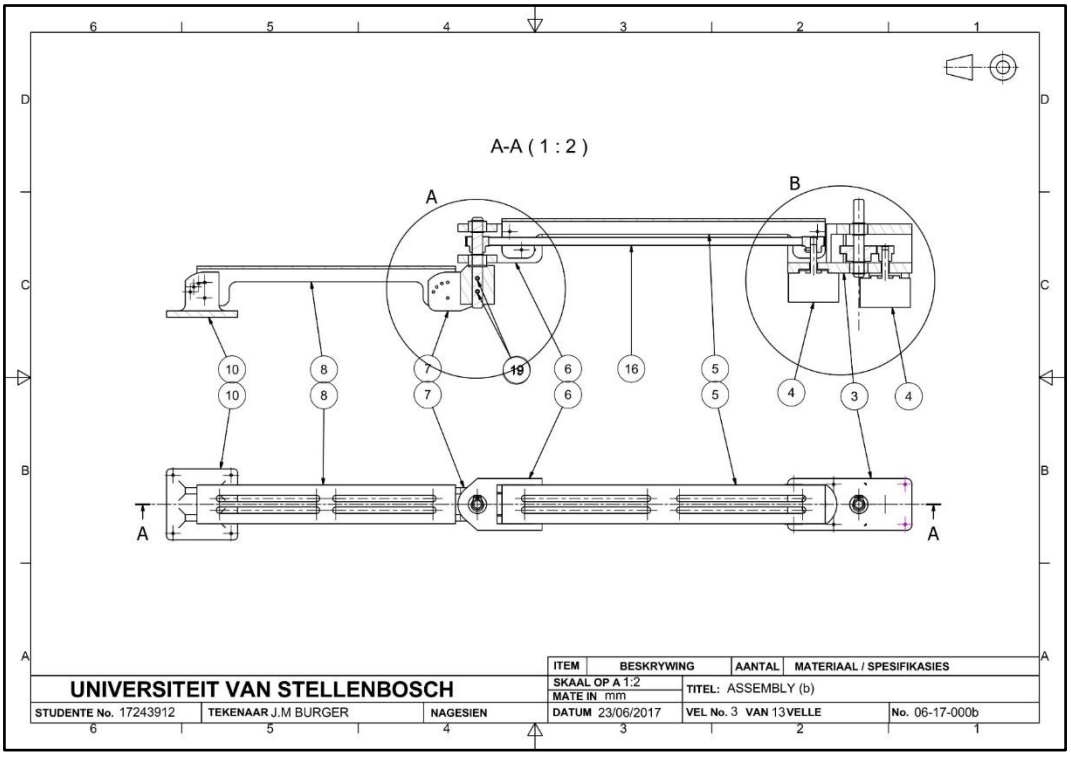

Figure 59: Assembly (b)

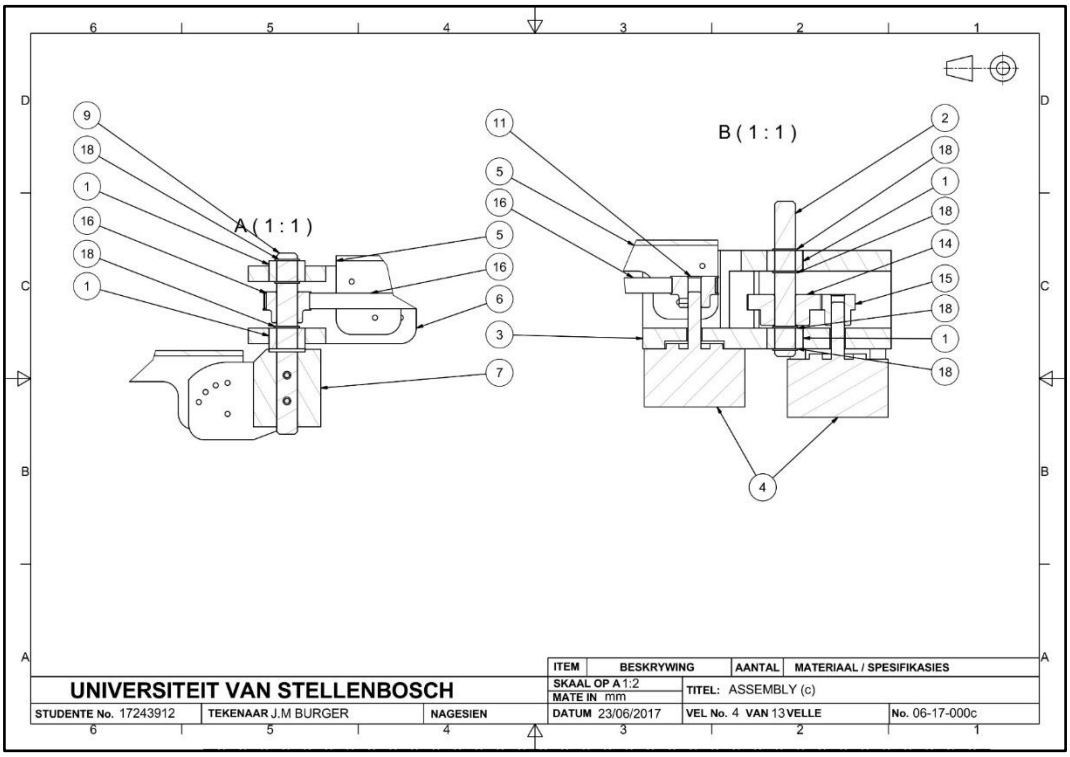

Figure 60: Assembly (c)

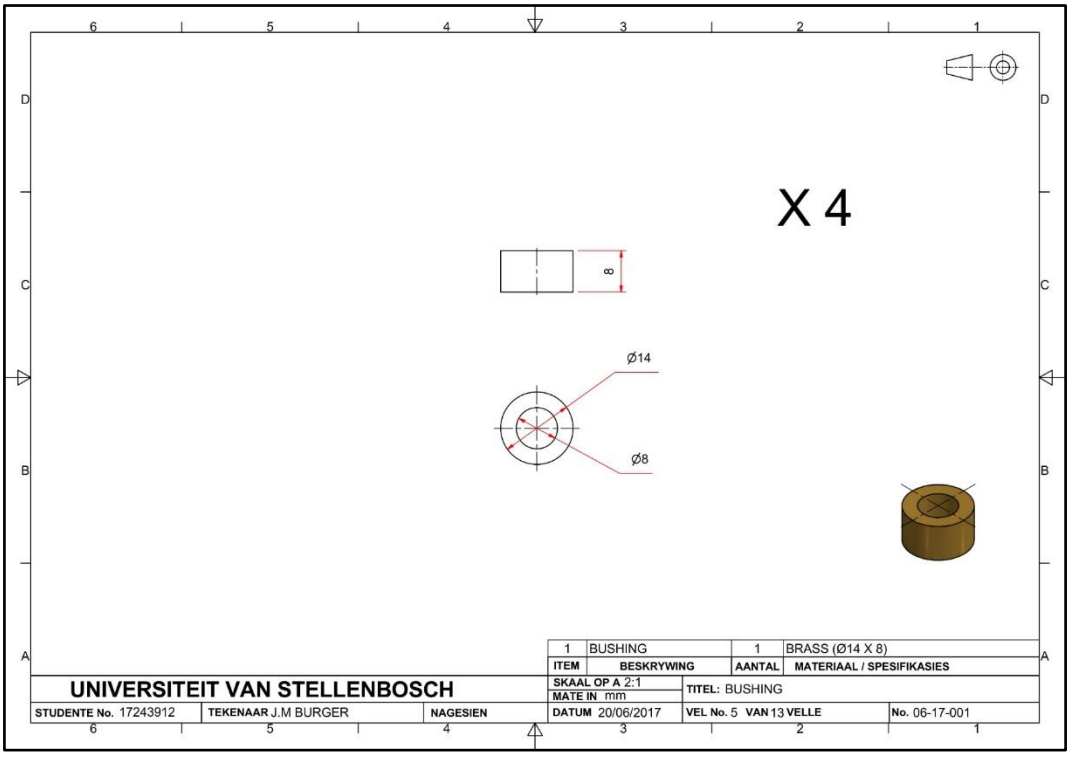

Figure 61: Bushing

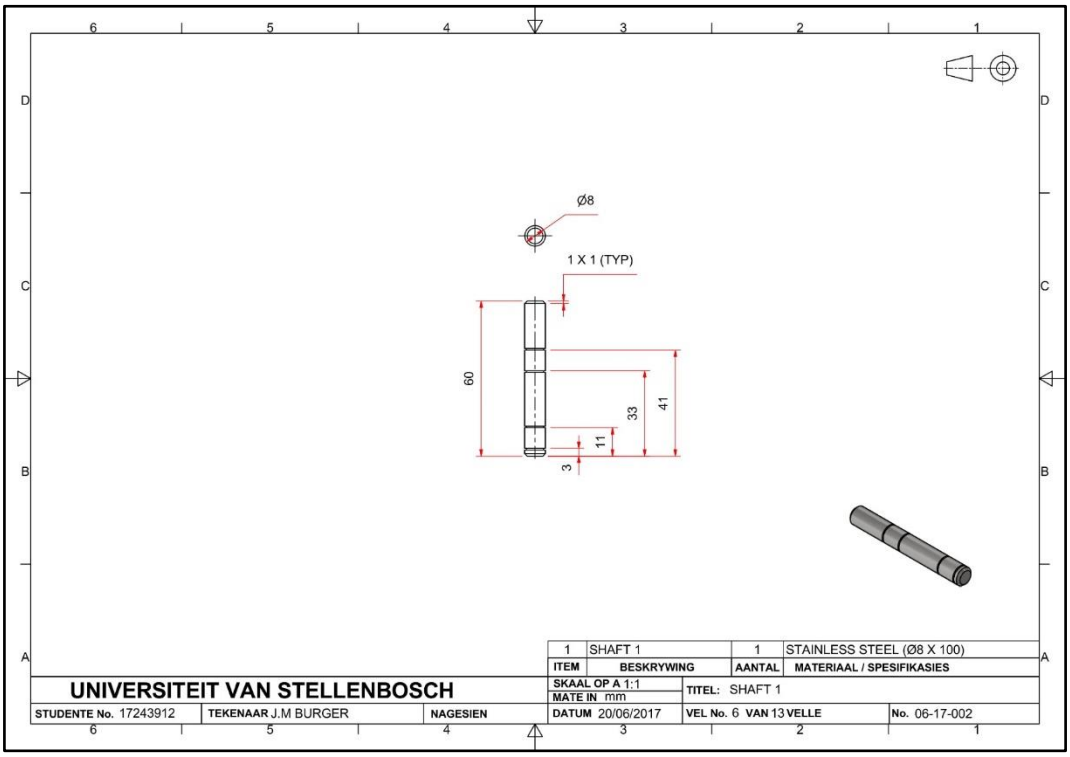

Figure 62: Shaft 1

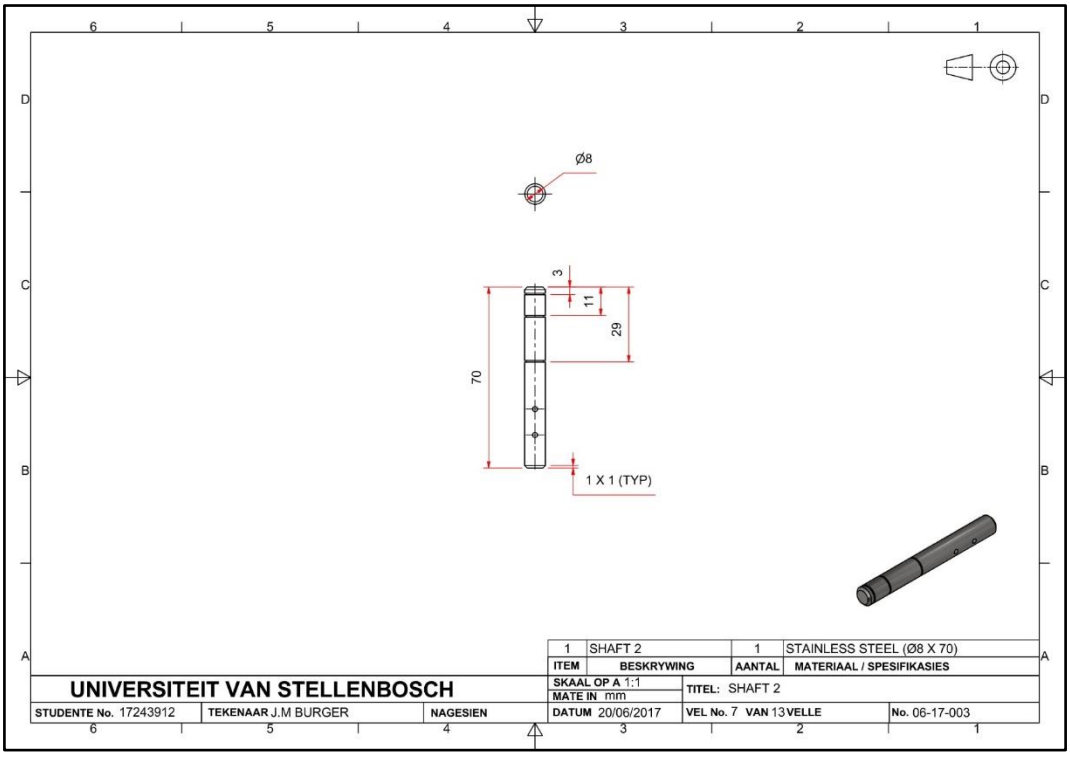

Figure 63: Shaft 2

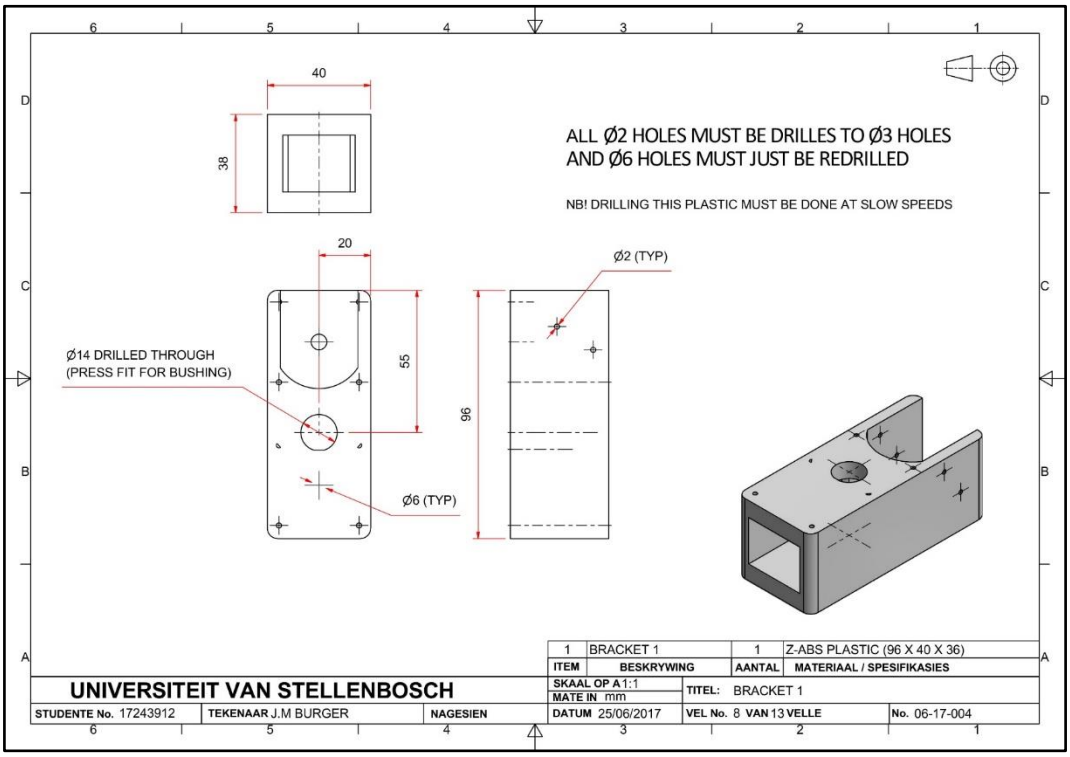

Figure 64: Bracket 1

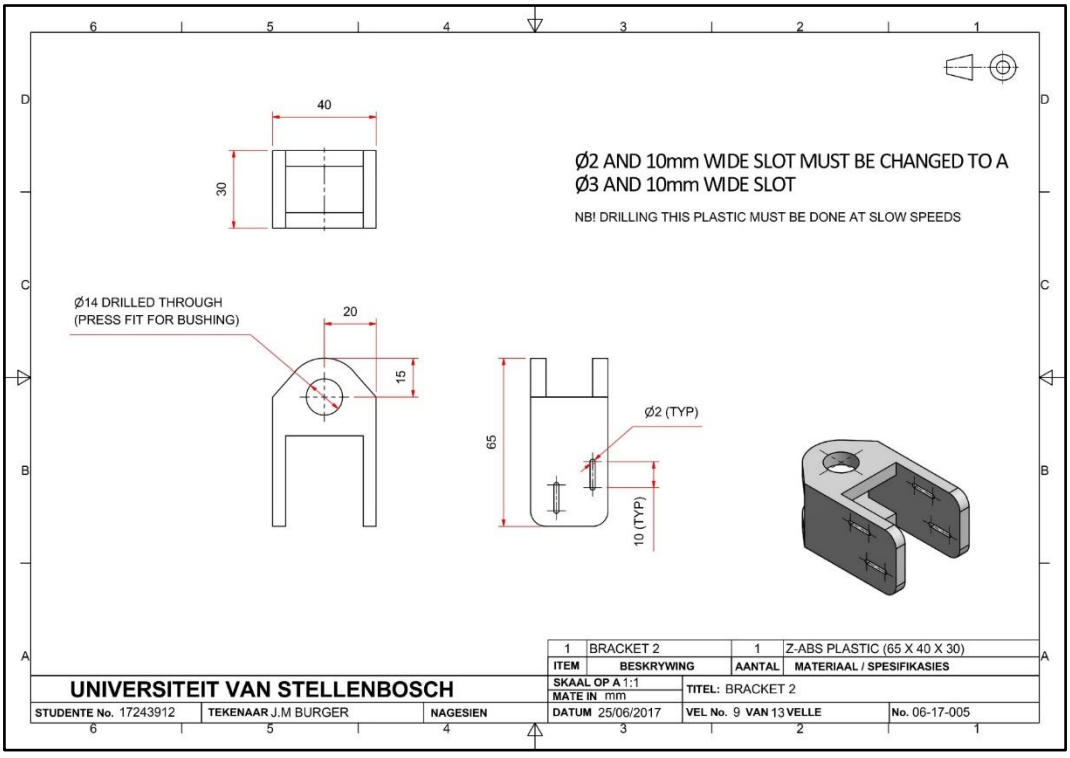

Figure 65: Bracket 2

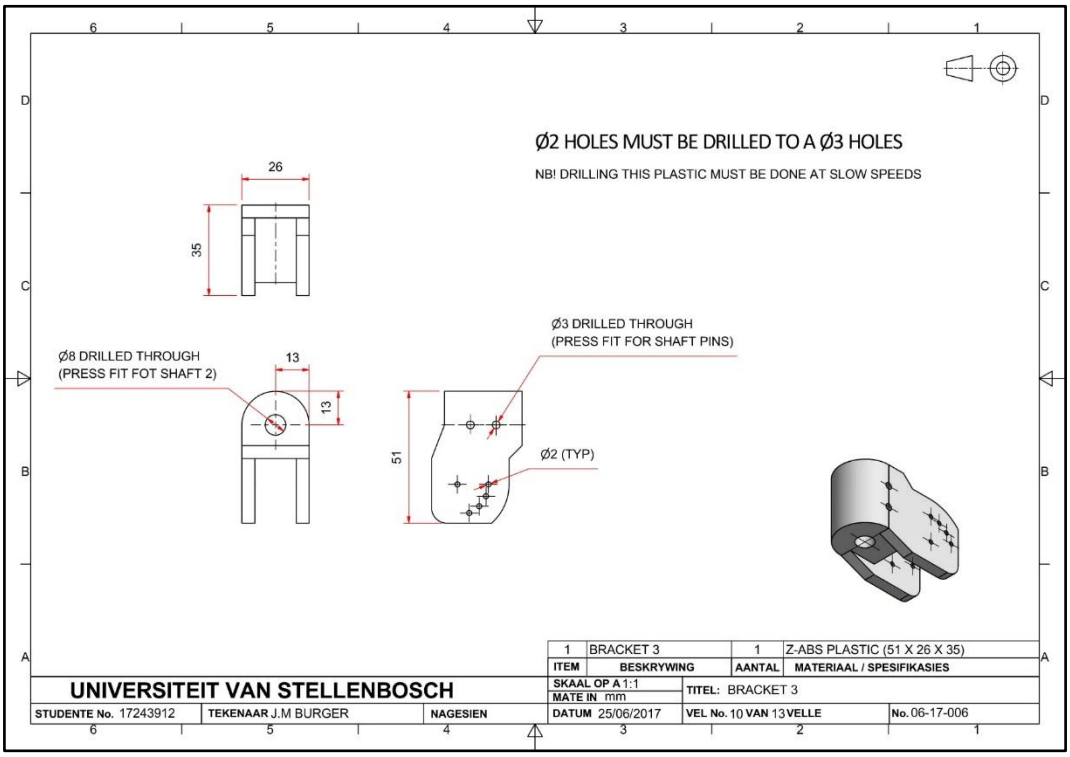

Figure 66: Bracket 3

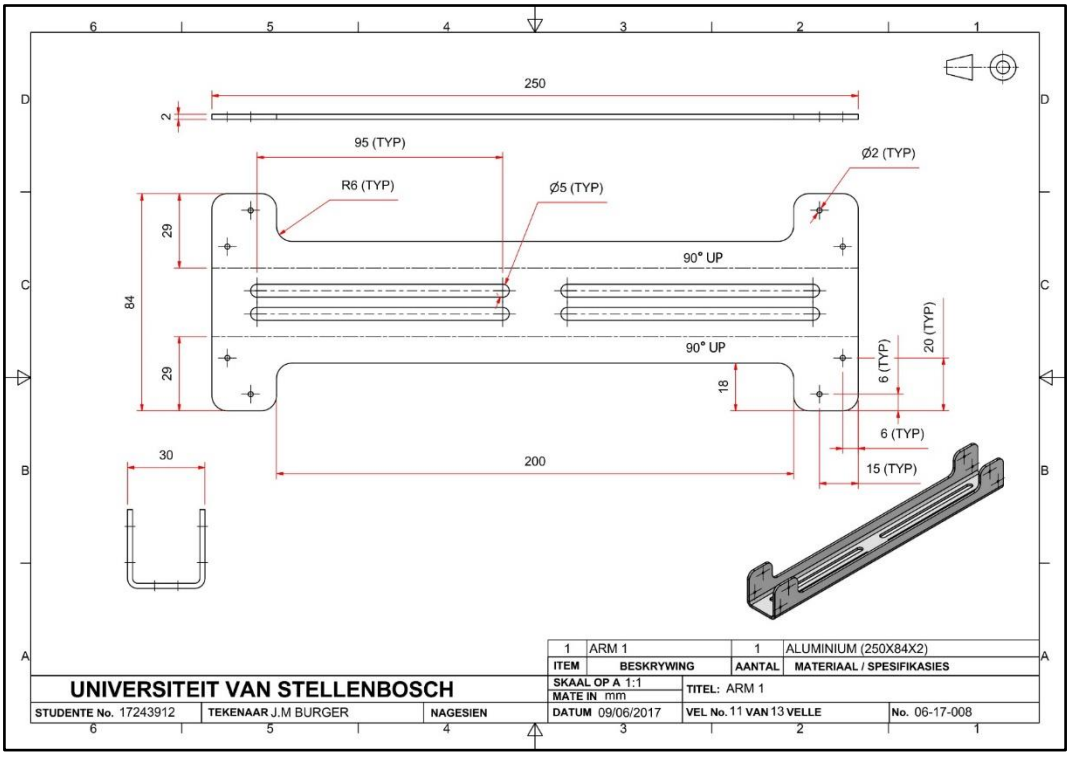

Figure 67: Arm 1

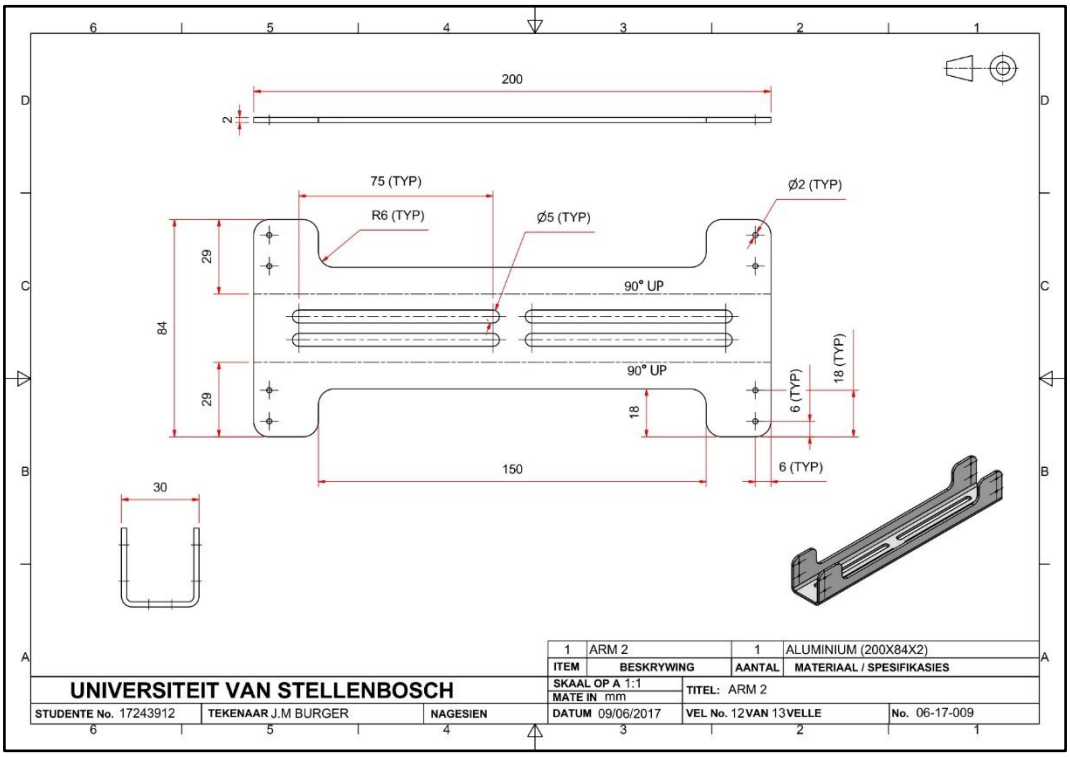

Figure 68: Arm 2

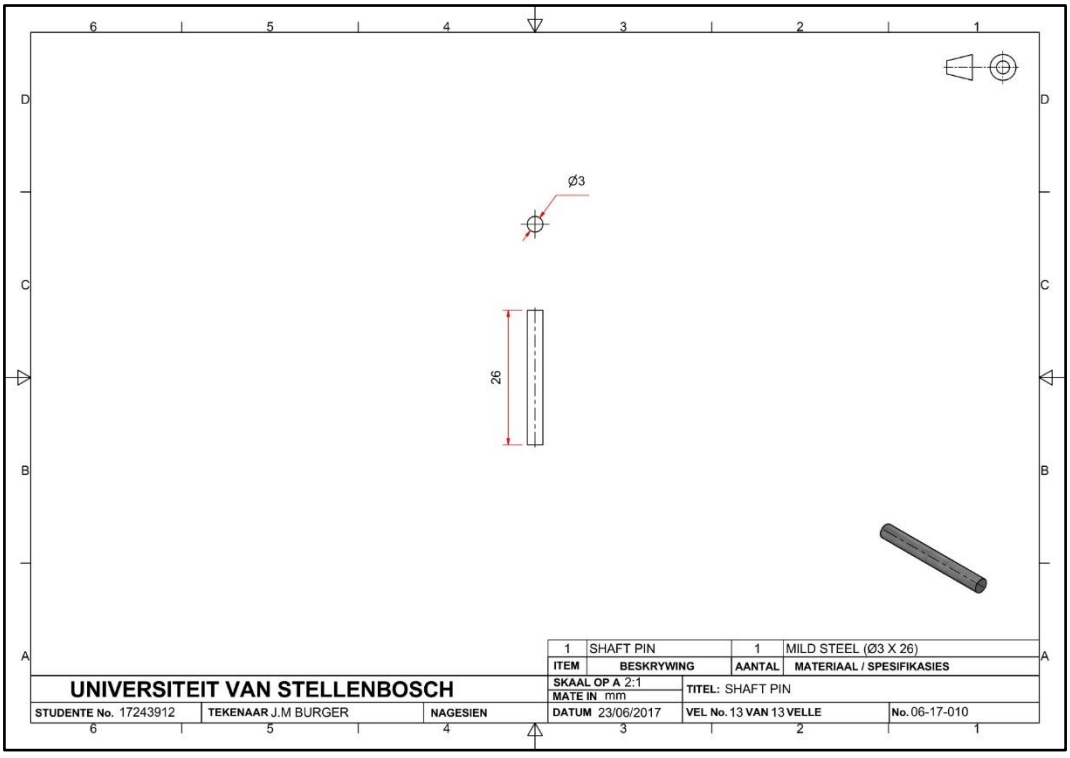

Figure 69: Shaft pin

D.2 Motor calculations

19 Jun 2018 21:05:02 - Prototype_calculations.sm

Mass Calculation:

Plastic Density: (Z-ABS) $\rho\_p := 1,05 \frac{g}{cm^3} = 1050 \frac{kg}{m^3}$

Aluminium Density: $\rho\_a := 2,7 \frac{g}{cm^3} = 2700 \frac{kg}{m^3}$

Steel Density: $\rho\_s := 8,05 \frac{g}{cm^3} = 8050 \frac{kg}{m^3}$

Brass Density: $\rho\_b := 8,7 \frac{g}{cm^3} = 8700 \frac{kg}{m^3}$

Plastic volume:

$p1 := (40\,mm \cdot 10\,mm \cdot 8\,mm) + (30\,mm \cdot 40\,mm \cdot 37\,mm) = 4,76 \cdot 10^{-5}\,m^3$

$p2 := (60\,mm \cdot 40\,mm \cdot 30\,mm) - (18\,mm \cdot 60\,mm \cdot 30\,mm) = \frac{99\,m^3}{2500000}$

$p3 := (26\,mm \cdot 30\,mm \cdot 50\,mm) - (25\,mm \cdot 30\,mm \cdot 16\,mm) = \frac{27\,m^3}{1000000}$

$p4 := (5\,mm \cdot 130\,mm \cdot 130\,mm) + (26\,mm \cdot 30\,mm \cdot 26\,mm) - (30\,mm \cdot 26\,mm \cdot 16\,mm) = \frac{923\,m^3}{10000000}$

Therefor: $V\_p := p1 + p2 + p3 + p4 = 0,0002\,m^3$

Plastic mass: $m\_p := V\_p \cdot \rho\_p = 0,2168\,kg$

Aluminium volume:

$a1 := (250\,mm \cdot 2\,mm \cdot 84\,mm) - (20\,mm \cdot 2\,mm \cdot 200\,mm) = 3,4 \cdot 10^{-5}\,m^3$

$a2 := (200\,mm \cdot 2\,mm \cdot 84\,mm) - (20\,mm \cdot 2\,mm \cdot 150\,mm) = 2,76 \cdot 10^{-5}\,m^3$

Therefor: $V\_a := a1 + a2 = 6,16 \cdot 10^{-5}\,m^3$

Aluminium mass: $m\_a := V\_a \cdot \rho\_a = 0,1663\,kg$

Shaft volume:

$s1 := \pi \cdot (4\,mm)^2 \cdot 100\,mm = 5,0265 \cdot 10^{-6}\,m^3$

$s2 := \pi \cdot (4\,mm)^2 \cdot 80\,mm = 4,0212 \cdot 10^{-6}\,m^3$

Therefor: $V\_s := s1 + s2 = 9,0478 \cdot 10^{-6}\,m^3$

Shaft mass: $m\_s := V\_s \cdot \rho\_s = 0,0728\,kg$

Bush volume:

$b1 := \left(\pi \cdot (7\,mm)^2 \cdot 10\,mm\right) - \left(\pi \cdot (4\,mm)^2 \cdot 10\,mm\right) = 1,0367 \cdot 10^{-6}\,m^3$

Therefor: $V\_b := 4 \cdot b1 = 4,1469 \cdot 10^{-6}\,m^3$

Bush mass: $m\_b := V\_b \cdot \rho\_b = 0,0361\,kg$

Gimbal mass: $m\_g := 0,3\,kg$

Stepper motor mass: $m\_step := (0,2 + 0,24)\,kg$

1 / 7

TOTAL MASS: $Tot\_mass := m\_p + m\_a + m\_s + m\_b + m\_g + m\_step = 1,2321\ kg$

Inertia and Torque Calculations:

Diagram:

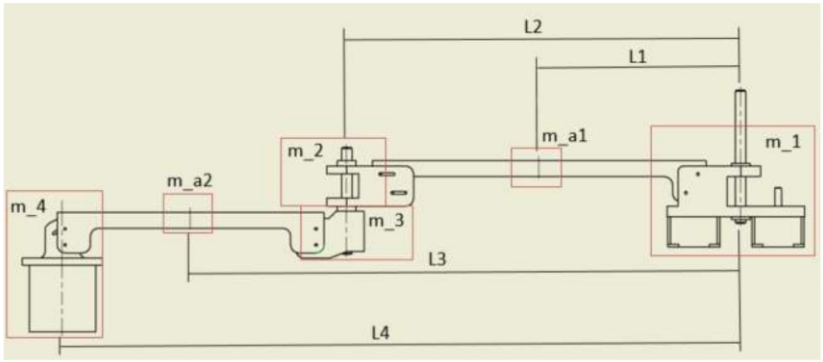

Lengths:

$L1 := 150\ mm$
$L2 := 300\ mm$
$L3 := 420\ mm$
$L4 := 510\ mm$

Mass:

$m\_1 := p1 \cdot \rho\_p + m\_step = 0,49\ kg$

$m\_2 := p2 \cdot \rho\_p = 0,0416\ kg$

$m\_3 := p3 \cdot \rho\_p = 0,0283\ kg$

$m\_4 := p4 \cdot \rho\_p + m\_g = 0,3969\ kg$

$m\_23 := m\_2 + m\_3 + s2 \cdot \rho\_s = 0,1023\ kg$

$m\_a1 := a1 \cdot \rho\_a = 0,0918\ kg$

$m\_a2 := a2 \cdot \rho\_a = 0,0745\ kg$

Inertia:

$$J\_1 := \frac{1}{12} \cdot (m\_1) \cdot \left((40\ mm)^2 + (100\ mm)^2 \right) = 0,0005\ kg\ m^2$$

$$J\_a1 := \frac{1}{12} \cdot (m\_a1) \cdot \left((30\ mm)^2 + (250\ mm)^2 \right) = 0,0005\ kg\ m^2$$

$$J\_23 := \frac{1}{12} \cdot (m\_23) \cdot \left((40\ mm)^2 + (88\ mm)^2 \right) = 7,9658 \cdot 10^{-5}\ kg\ m^2$$

$$J\_a2 := \frac{1}{12} \cdot (m\_a2) \cdot \left((30\ mm)^2 + (200\ mm)^2 \right) = 0,0003\ kg\ m^2$$

$$J\_4 := \frac{1}{12} \cdot (m\_4) \cdot \left((60\ mm)^2 + (60\ mm)^2 \right) = 0,0002\ kg\ m^2$$

Inertia:

$$J\_motor1 := (J\_1) + \left(J\_a1 + m\_a1 \cdot \left(L1^2 \right) \right) + \left(J\_23 + m\_23 \cdot \left(L2^2 \right) \right) + \left(J\_a2 + m\_a2 \cdot \left(L3^2 \right) \right) + \left(J\_4 + m\_4 \cdot \left(L4^2 \right) \right)$$

$J\_motor1 = 0,1292\ kg\ m^2$

$J\_motor2 := (J\_23) + \left(J\_a2 + m\_a2 \cdot (L3 - L2)^2\right) + \left(J\_4 + m\_4 \cdot (L4 - L3)^2\right) = 0,0049\ kg\ m^2$

Motor Inertia:

$J\_rotor := 0,011\ kg\ cm^2 = 1,1 \cdot 10^{-6}\ kg\ m^2$

Torque:

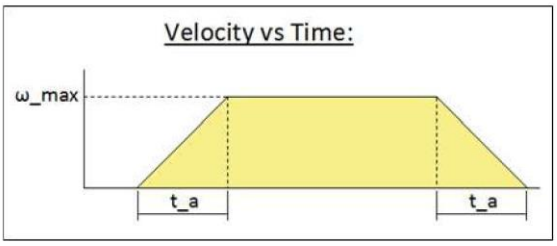

Motor 1:

Load Torque: $T\_L\_1 := 0$

$RPM1 := 5\ rpm$

Maximum operating angular velocity: $\omega\_max := RPM1 = 0,5236 \frac{rad}{s}$

Maximum acceration time to achieve max velocity: $t\_a := 0,3\ s$

Therefor maximum angular acceration: $a\_max := \frac{\omega\_max}{t\_a} = 1,7453 \cdot \frac{1}{s^2}$

Acceleration Torque: $T\_a\_1 := (J\_motor1 + J\_rotor) \cdot a\_max = 0,2255\ J$

Safety Factor: $S\_f := 1,5$

Required Torque: $T\_M\_1 := (T\_L\_1 + T\_a\_1) \cdot S\_f = 0,3382\ N\ m$

Motor 2:

Load Torque: $T\_L\_2 := 0$

$RPM2 := 5\ rpm$

Maximum operating angular velocity: $\omega\_max := RPM2 = 0,5236 \frac{rad}{s}$

Maximum acceration time to achieve max velocity: $t\_a := 0,015\ s$

Therefor maximum angular acceration: $a\_max := \frac{\omega\_max}{t\_a} = 34,9066 \cdot \frac{1}{s^2}$

Acceleration Torque: $T\_a\_2 := (J\_motor2 + J\_rotor) \cdot a\_max = 0,1697\ J$

Safety Factor: $S\_f := 1,5$

Required Torque: $T\_M := (T\_L\_2 + T\_a\_2) \cdot S\_f = 0,2545\ N\ m$

Pulley Calculation:

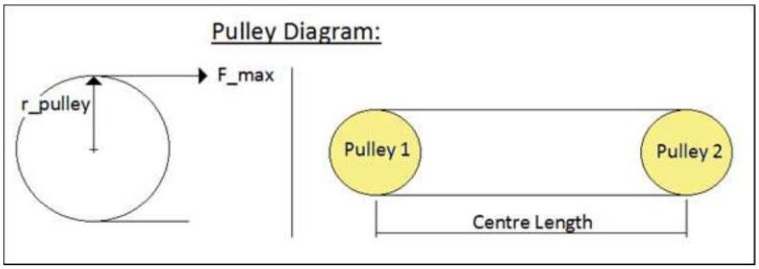

Centre length: $C\_l := 262\ mm$

Pulley 1 = pulley 2

Number of pulley teeth: $n\_p := 24$

Pulley Pitch: $p\_p := 2,5\ mm$

Pulley Radius: $r\_pulley := \frac{18,55}{2}\ mm = 0,0093\ m$

Required timming belt width: $b\_wid := 6\ mm$

Maximum operating torque: $T\_max := 0,08\ N\ m$

Maximum operating angular velocity of pulley: $\omega\_p\_max := 2 \cdot \pi \frac{rad}{s}$

Pulley safety factor: $S\_f := 1,5$

Required pulley power: $P\_req := S\_f \cdot \omega\_p\_max \cdot T\_max = 0,754\ W$

Pulley Product Details:

Product Details

Metric Pitch Timing Belt Pulleys

Aluminium timing pulleys to suit all polyurethane timing belts
Except for 48 and 60 tooth, all pulleys have flanges and all have standard pilot bores

☐ Add product to Compare

Specification

Not what you're looking for? Select the attributes you require, then click the button below.

☐ Number of Teeth	24
☐ Pitch	2.5mm
☐ To Suit Belt Width	6mm
☐ Bore	4mm
☐ Maximum Bore Diameter	11mm
☐ Outside Diameter	18.55mm
☐ Hub Diameter	12mm
☐ Material	Aluminium

Timing Belt Product Details:

Product Details

Metric Pitch Timing Belts – Contitech Syncroflex®

Wear-resistant polyurethane contilan belt with high grade wire tension members. Resulting bond gives high flank load capacity combined with low elastic elongation. Suitable for all kinds of drives because of flexibility of belt material and high flexural strength of the steel tension members.

- Belt speed up to 80m/s
- Up to 40000rpm
- Temperature range -30°C to +80°C
- Efficient up to 98%
- Maintenance-free
- Resistant to oils, grease and petrol
- Power rating 0.5kW (2.5mm pitch)
- Power rating 5.0kW (5mm pitch)

Dimensions (mm)				
Pitch	Length	Width	Thickness (B)	Tooth Height (T)
2.5	120 - 1300	6	1.3	0.7
5	150 - 1500	10	2.2	1.2
5	165 - 1500	16	2.2	1.2

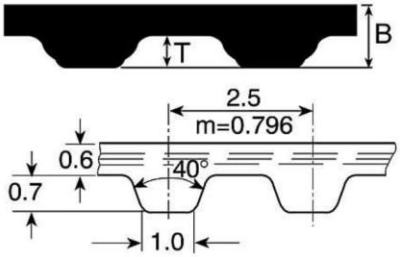

Gear Calculation:

Assume that stress due to bending is considered and that the compression due to the radial component of the force is neglected.

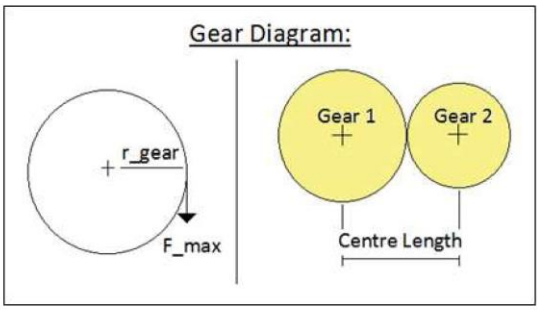

Calculations was done from the Shigley's Mechanical textbook spur gear design Page 733-740 Chapter 14

Maximum operating torque of motor 1: $T_{max} := 0,4\ N\,m$

Gear 2:

Gear 2 is run by the motor 1 and drives the first gear that is attached to the shaft:

Number of teeth: $n\_g2 := 16$

Face width: $F\_wid2 := 6\ mm$

Pitch diameter: $d\_p2 := 12,8\ mm$

Radius of gear (pitch diameter/2): $r\_gear2 := \frac{d\_p2}{2} = 0,0064\ m$

Diametral pitch: $P2 := \frac{n\_g2}{d\_p2} = 1250 \cdot \frac{1}{m}$

Maximum operating force: $F\_max2 := \frac{T\_max}{r\_gear2} = 62,5\ N$

Find the values for the Lewis Form Factor (Y) table 14.2 pg 738 and is for a pressure angle of 20 degrees

Lewis Form Factor: $Y2 := 0,296$

Required tensile strength: $\sigma := \frac{(F\_max2 \cdot P2)}{(F\_wid2 \cdot Y2)} = 4,3989 \cdot 10^{7}\ Pa$

Rated tensile strength of gear 2: $569 \frac{N}{mm^2} = 5,69 \cdot 10^{8}\ Pa$

Gear 1:

Gear 1 is attached to the shaft:

Number of teeth: $n\_g1 := 35$

Face width: $F\_wid1 := 6\ mm$

Pitch diameter: $d\_p1 := 28\ mm$

Radius of gear (pitch diameter/2): $r\_gear1 := \frac{d\_p1}{2} = 0,014\ m$

Diametral pitch: $P1 := \frac{n\_g1}{d\_p1} = 1250 \cdot \frac{1}{m}$

Maximum operating force: $F\_max1 := \frac{T\_max}{r\_gear1} = 28,5714\ N$

Find the values for the Lewis Form Factor (Y) table 14.2 pg 738 and is for a pressure angle of 20 degrees

Lewis Form Factor: $Y1 := 0,371$

Required tensile strength: $\sigma := \frac{(F\_max1 \cdot P1)}{(F\_wid1 \cdot Y1)} = 1,6044 \cdot 10^{7}\ Pa$

Rated tensile strength of gear 1: $569 \frac{N}{mm^2} = 5,69 \cdot 10^{8}\ Pa$

D.3 Surrogate stand's engineering drawings

These are the engineering drawings of the stand used to hold the SLS surrogate above the workspace.

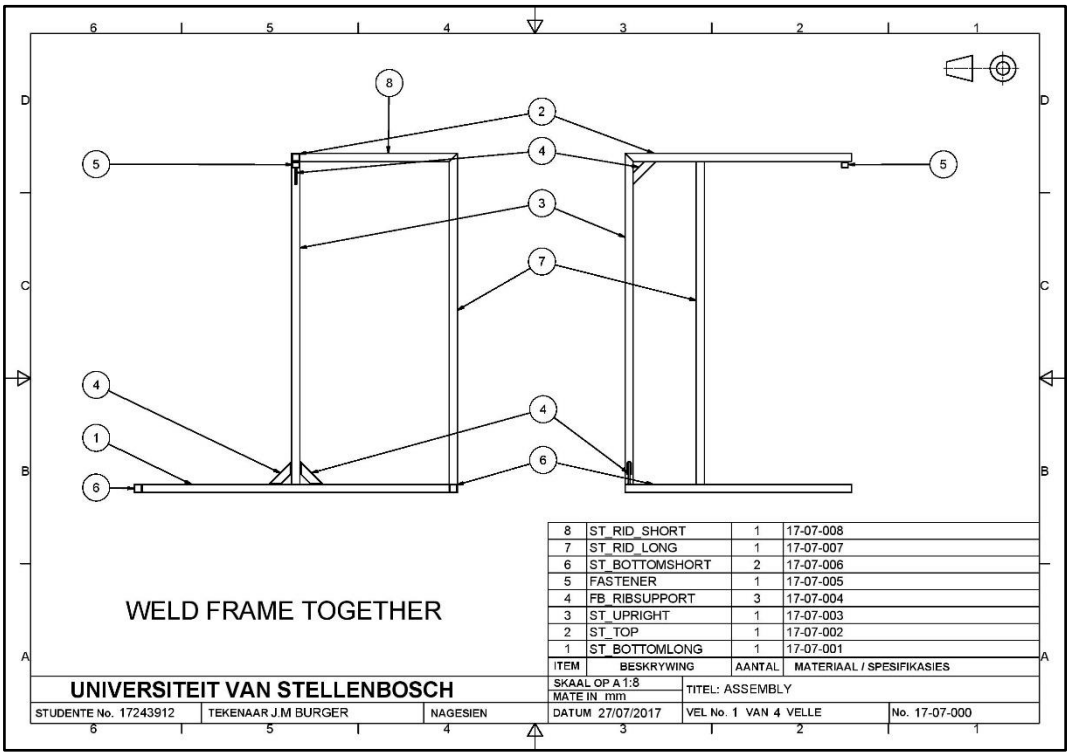

Figure 70: Assembly

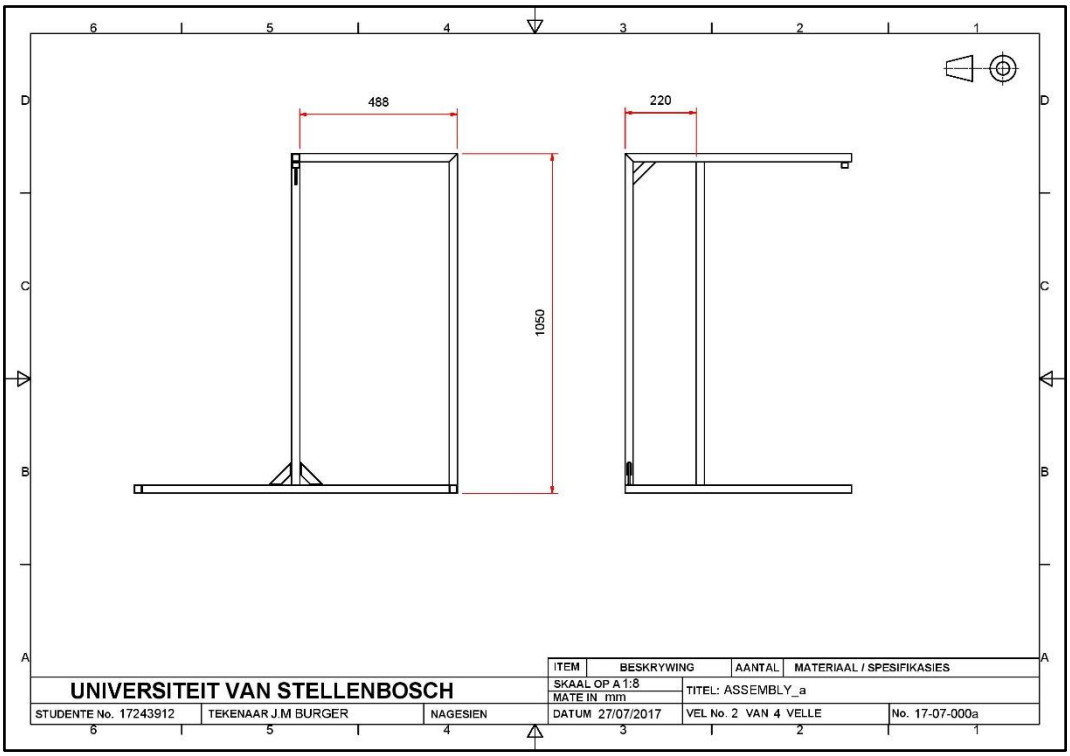

Figure 71: Asesembly_A

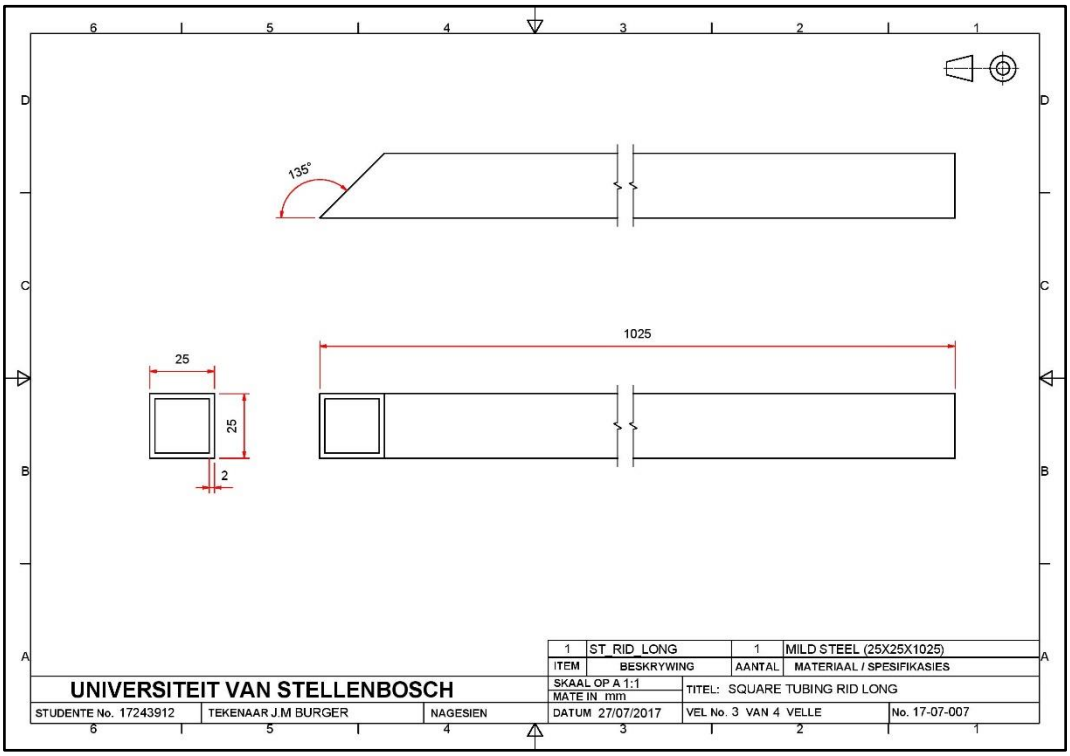

Figure 72: Square tubing rib long

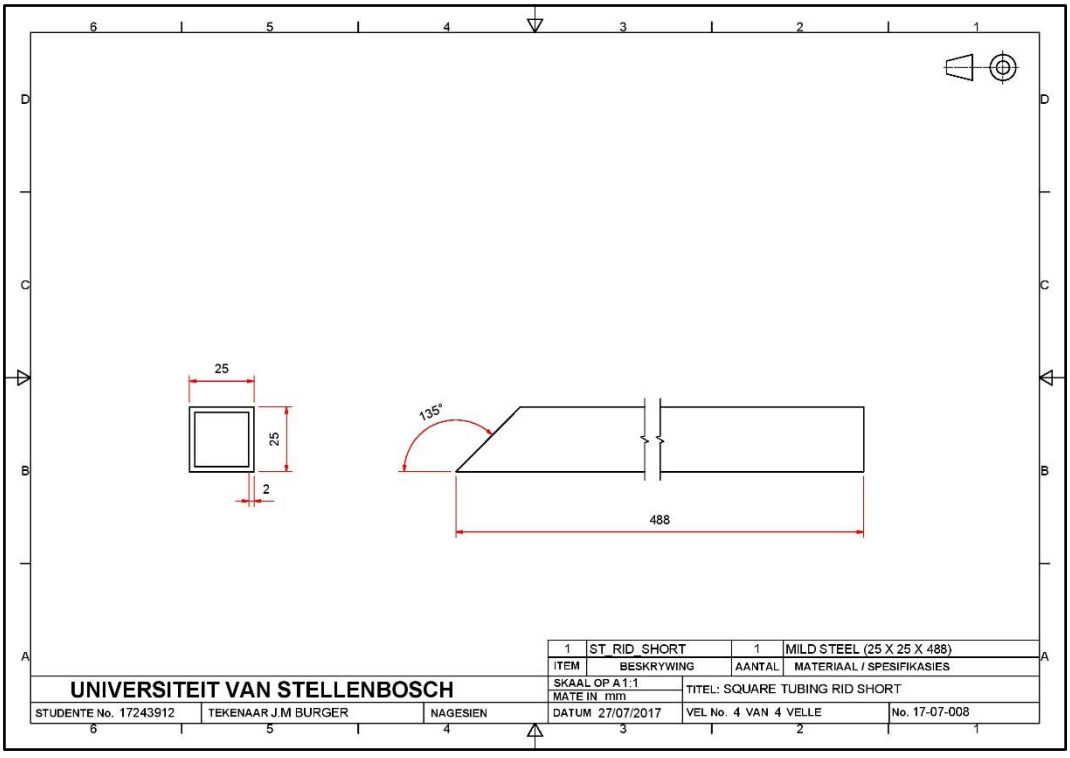

Figure 73: Square tubing rib short

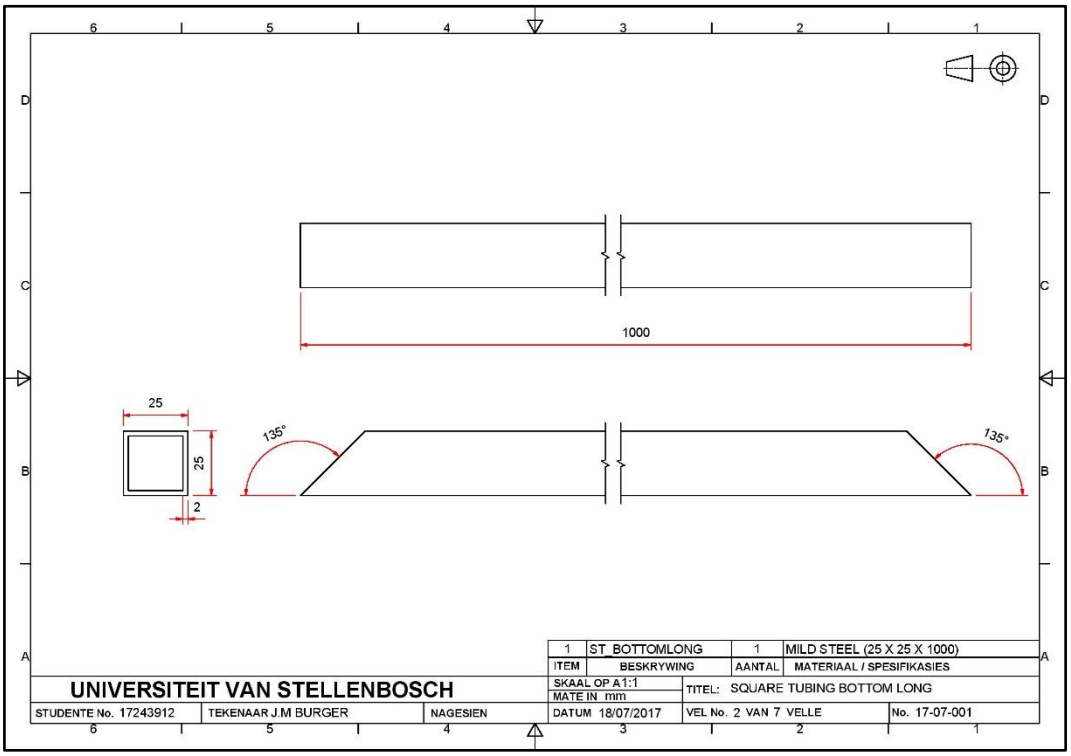

Figure 74: Square tubing bottom long

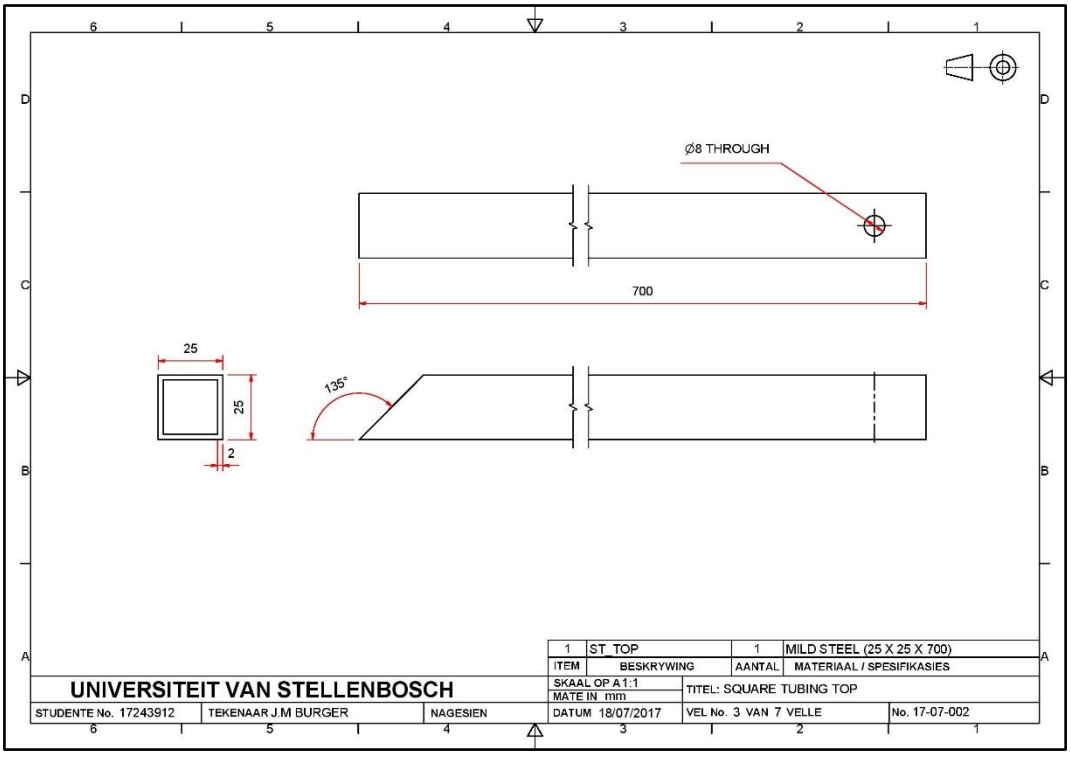

Figure 75: Square tubing top

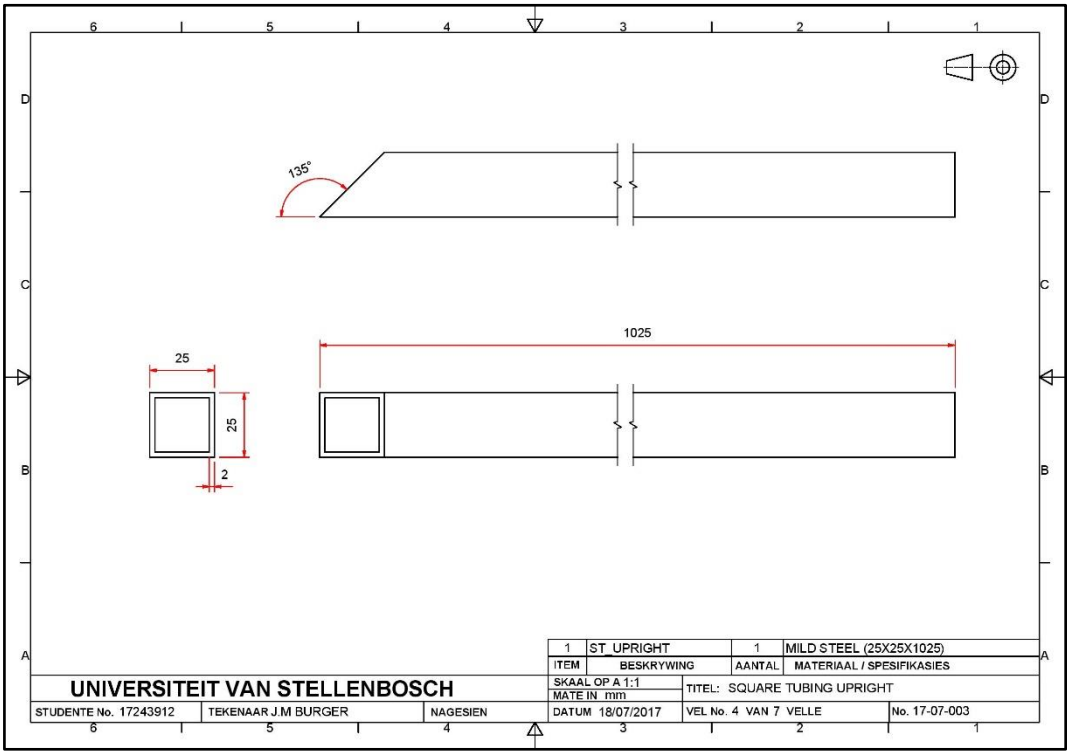

Figure 76: Square tubing upright

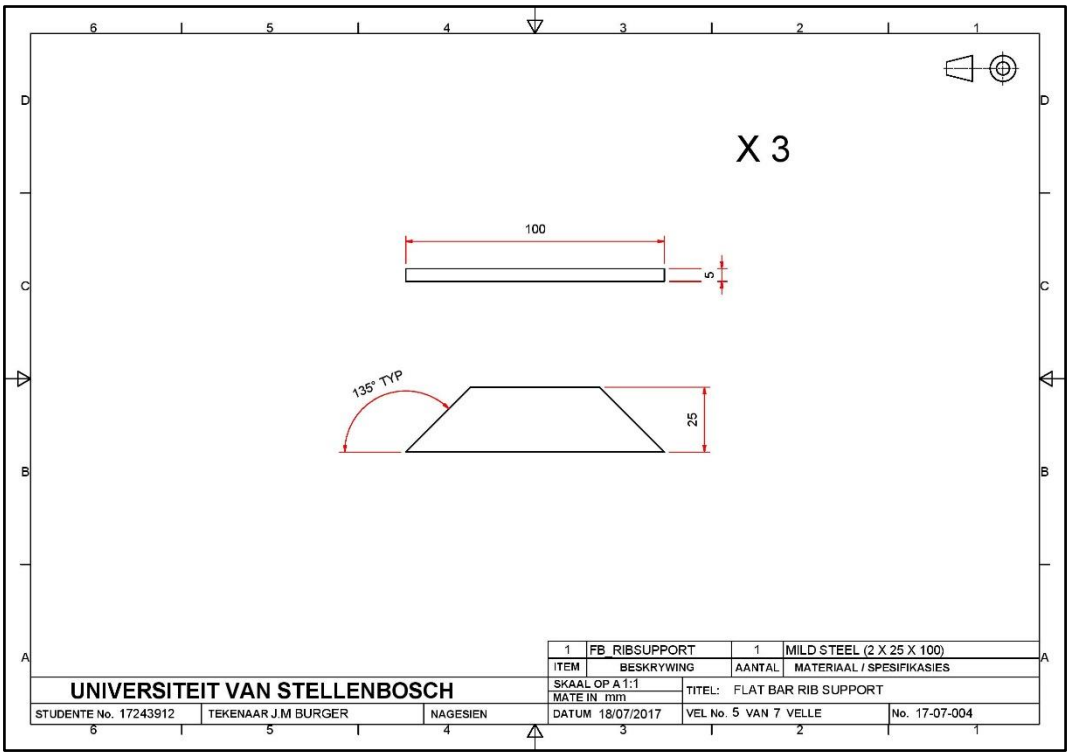

Figure 77: Flat bar rib support

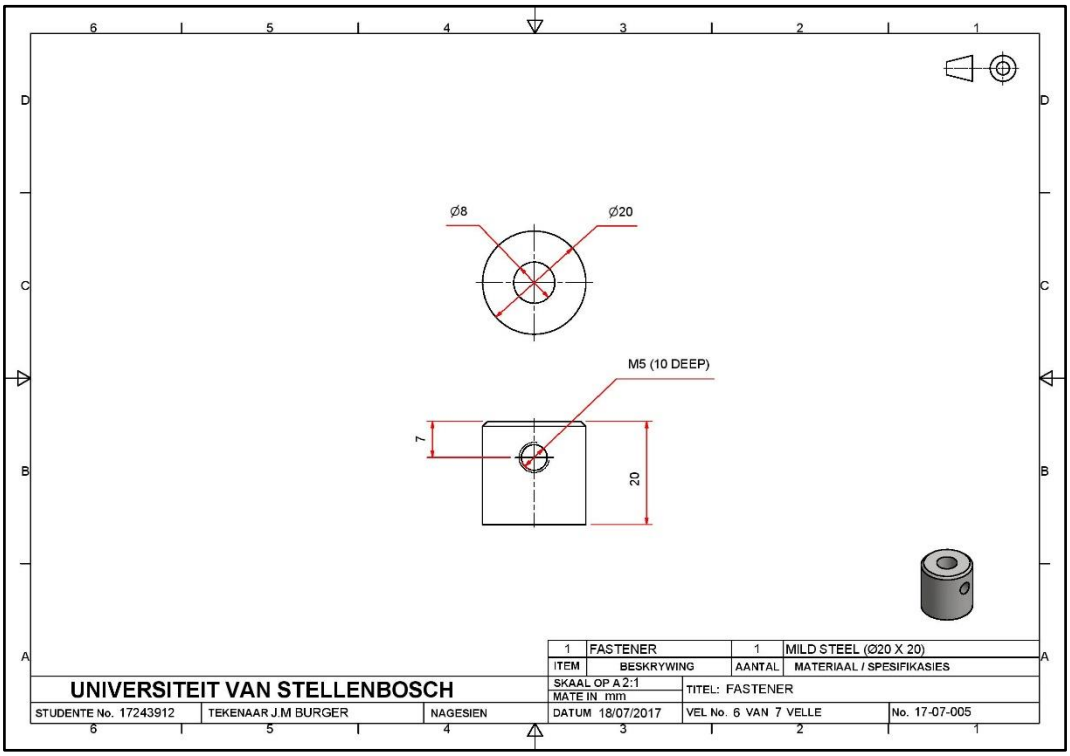

Figure 78: Fastener

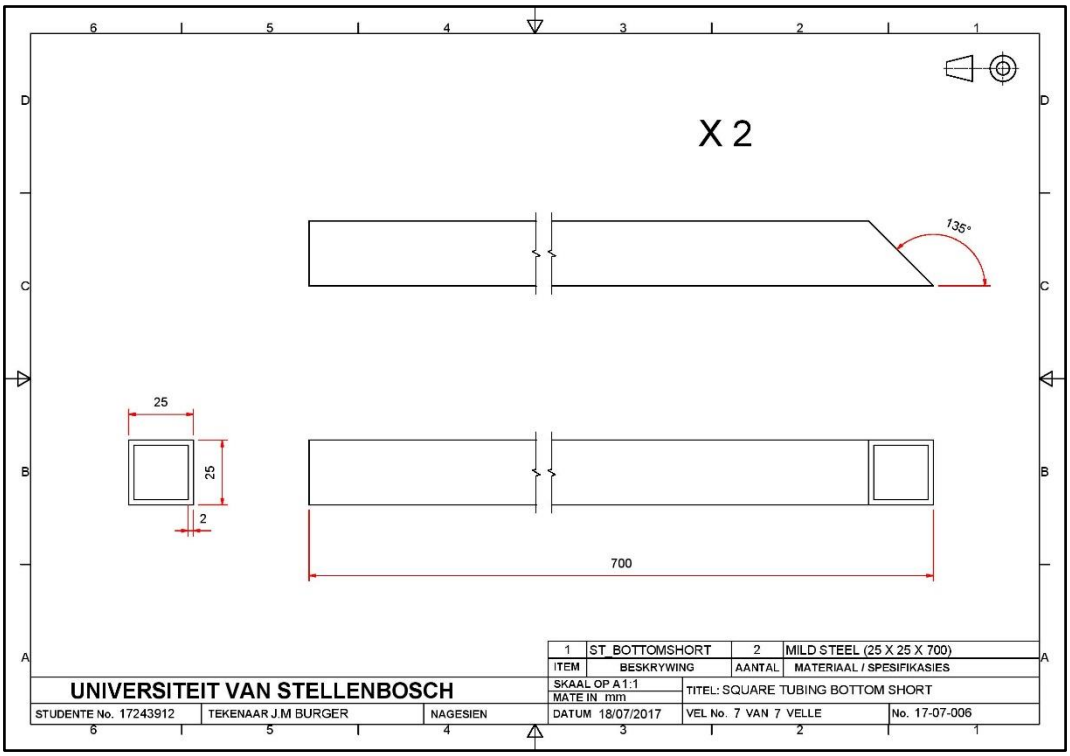

Figure 79: Square tubing bottom short

Appendix E Combine algorithm and SLS surrogate

E.1 Workspace grid calculation

Grid Calculation:

Calculating grid size to ensure that the surgeon does not cause a shadow over the wound.

Worse case scenario:

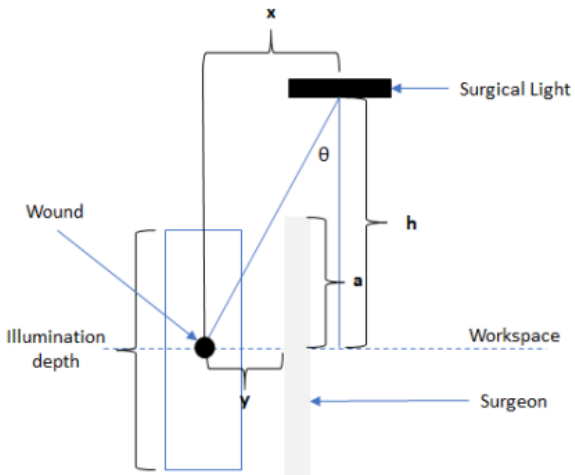

Grid_square_block_size := 250 mm

Prototype_scale := 3 Scale of prototype

Average_male_height := 1,8 m Surgeon's height

y := 150 mm Distance of surgeon from

Illumination_depth := 1000 mm

Hieght_of_SL := 1 m Height of surgical light above the illumination depth.

Workspace_height := 1200 mm Hieght of workspace from floor

$h := \frac{Illumination\_depth}{2} + Hieght\_of\_SL = 1,5\ m$

$x := \frac{Grid\_square\_block\_size}{2} \cdot Prototype\_scale = 0,375\ m$

a := Average_male_height − Workspace_height = 0,6 m Remaining height of surgeon

$New\_a := \frac{h \cdot y}{x} = 0,6\ m$ The new a should not exceed a, because if it does the surgeon will be infront of the surgical light.

Workspace_length := Grid_square_block_size · 4 · Prototype_scale = 3 m

$Workspace\_area := Workspace\_length^{2} = 9\ m^{2}$ Actual workspace area

$Theta := \tanh\left(\frac{y}{h}\right) = 5,7106\ deg$

Appendix F Testing

F.1 Stereo vision accuracy

Table 9: Stereo Vision Accuracy

Actual:													
Distance (mm):	Negative axis:							Positive axis:					
	300	250	200	150	100	50	0	50	100	150	200	250	300
Measured Distances:													
X-Direction: (mm)	292	251	203	150	102	54	0	50	99	147	191	243	289
	290	243	196	153	102	54	0	53	104	156	198	250	284
	286	244	198	150	104	51	0	53	104	149	201	243	287
	292	243	195	149	102	51	0	53	104	153	199	243	286
	294	246	198	154	105	54	0	54	105	152	198	242	284
	293	248	199	153	103	51	0	52	103	150	199	242	284
	294	243	195	152	103	49	0	53	101	151	201	243	286
	295	248	201	153	102	50	0	54	102	152	199	245	283
	300	248	200	154	100	49	0	51	103	148	198	243	284
	292	246	198	151	104	54	0	52	104	153	200	249	290
Y-Direction: (mm)	299	247	198	152	99	50	0	48	100	149	198	242	291
	308	254	202	153	104	51	0	53	102	152	207	255	310
	301	256	204	154	105	49	0	54	101	153	204	253	308
	307	254	206	152	102	50	0	53	100	154	206	254	302
	308	253	205	153	103	52	0	52	103	155	200	255	306
	313	253	202	154	102	51	0	52	104	154	202	260	304
	302	252	203	155	101	50	0	53	103	155	198	255	313
	300	253	201	152	101	52	0	51	99	156	199	257	308
	307	255	199	151	102	53	0	52	104	154	200	253	311
	303	256	203	153	101	51	0	53	100	154	198	252	309
Z-Direction: (mm)	313	248	211	154	101	53	0						
	302	253	204	158	110	43	0						
	305	241	206	149	98	52	0						
	292	241	193	150	95	53	0						
	305	253	203	160	100	52	0						
	291	250	205	156	110	43	0						
	299	244	195	150	108	56	0						
	303	255	202	158	110	52	0						
	308	248	193	160	100	53	0						
	295	255	206	149	95	53	0						

F.2 Arm translation

Table 10: Arm translation accuracy and repeatability

Actual:	**Measured:**								
Positions:	After 1 movement (mm):			After 3 movements (mm):			After 5 movements (mm):		
2 X:	-8	-7	-8	9	8	10	10	7	8
Y:	-2	-7	-10	12	-11	-11	-14	-10	-8
Δt:	9.7’s	9.8’s	9.4’s						
3 X:	2	5	4	-2	0	-1	1	-2	2
Y:	-1	5	8	-10	-9	-7	-14	-11	-8
Δt:	8.3’s	8.1’s	7.9’s						
5 X:	-5	-8	-8	-8	-10	-6	-5	-9	-8
Y:	-12	-13	-12	-20	-10	-8	-18	-12	-6
Δt:	7.3’s	7.6’s	7.8’s						
6 X:	-5	-2	-1	-2	-5	-2	-1	2	-1
Y:	-8	-10	-8	-10	-15	-14	-8	-16	-15
Δt:	6.2’s	5.8’s	5.5’s						
7 X:	-13	-10	-8	-10	-8	-8	-9	-9	-8
Y:	3	2	4	1	5	6	0	4	3
Δt:	5.2’s	5.1’s	5.4’s						
8 X:	-10	-8	-10	-7	-11	-15	-8	-10	-16
Y:	2	-4	0	-3	-2	-20	-5	-1	-18
Δt:	6.2’s	6.5’s	6.1’s						
9 X:	9	-8	-10	-7	-8	-11	-2	-7	-9
Y:	-2	4	-3	-3	2	-5	-5	1	-4
Δt:	6.4’s	6.2’s	6.7’s						
10 X:	5	-4	-2	-6	-3	1	-5	-10	2
Y:	-8	-11	0	-5	-12	-5	-10	-10	-6
Δt:	3.9’s	4’s	3.5’s						
11 X:	2	-2	-3	5	-4	0	3	3	2
Y:	-2	1	2	-1	-1	-4	2	-3	-5
Δt:	2.1’s	1.9’s	1.8’s						
12 X:	-9	-5	-8	-10	-4	-9	8	5	-9
Y:	8	10	7	5	3	7	3	7	9
Δt:	5.3’s	5.2’s	5.4’s						
14 X:	-7	-10	-8	-4	-9	-7	-2	-8	-7
Y:	-2	-5	-10	-8	-9	-11	-10	-10	-13
Δt:	4.2’s	3.9’s	4.3’s						
15 X:	2	0	-2	2	3	-1	10	8	0
Y:	-4	-8	-9	-5	-11	-12	-6	-13	-14
Δt:	3.9’s	3.8’s	4.1’s						

F.3 Head rotation

Table 11: Head rotation accuracy and repeatability

Actual:	**Measured:**		
Number of tests:	After 1 movement (mm):	After 3 movements (mm):	After 5 movements (mm) :
1. X:	-2	0	15
Y:	10	4	5
2. X:	0	6	-5
Y:	-5	8	15
3. X:	6	-5	-5
Y:	6	19	-15
4. X:	-5	-10	-7
Y:	-14	-9	-12
5. X:	2	-2	4
Y:	-8	-5	8
6. X:	-2	0	0
Y:	4	-3	15
7. X:	-2	-7	-8
Y:	-7	18	6
8. X:	-1	6	2
Y:	-3	9	2
9. X:	-13	-3	-2
Y:	0	-2	-5
10. X:	-1	-6	1
Y:	-8	-4	-10

F.4 Combined arm translation and head rotation

Table 12: Arm translation and Head rotation accuracy and repeatability

Actual:	**Measured:**								
Positions:	After 1 movement (mm):			After 3 movements (mm):			After 5 movements (mm):		
2 X:	2	18	18	5	16	8	19	18	15
Y:	2	22	18	15	18	-2	20	19	22
Δt:	12.1’s	12.5’s	13.2’s						
3 X:	-10	2	-12	-6	8	5	10	7	6
Y:	10	3	8	5	9	13	-12	-2	13
Δt:	11.0’s	11.5’s	11.3’s						
5 X:	18	1	15	22	4	3	20	5	8
Y:	-5	-13	-8	-12	-14	4	-8	-2	-2
Δt:	12.3’s	12.0’s	12.7’s						
6 X:	12	6	-10	-3	-8	-8	4	5	-5
Y:	-10	-12	-4	-16	-2	-3	-11	2	-4
Δt:	8.2’s	7.9	7.6						
7 X:	-8	-7	-3	-10	-9	-9	-11	-8	-10
Y:	16	18	12	10	22	24	18	17	20
Δt:	9.8’s	9.1’s	9.4’s						
8 X:	-18	-19	-2	-17	-15	-10	-15	-11	-9
Y:	-2	10	4	10	21	10	8	2	9
Δt:	8.8’s	9.1’s	9.3’s						
9 X:	18	19	8	5	13	3	10	8	3
Y:	-18	-13	17	-22	-16	-15	-15	-12	-14
Δt:	9.5’s	9.8’s	9.7’s						
10 X:	-4	-2	10	3	8	9	-1	0	8
Y:	-8	-12	-11	-13	-8	-14	-14	-16	-10
Δt:	6.7’s	7.1’s	7.5’s						
11 X:	-2	-8	-10	-8	-1	0	-6	-4	-8
Y:	6	5	8	7	2	6	2	4	8
Δt:	3.2’s	3.5’s	3.1’s						
12 X:	-15	-8	-15	-14	-10	-18	-10	-16	-19
Y:	8	12	9	5	11	13	11	4	12
Δt:	8.8’s	7.9’s	8.7’s						
14 X:	18	17	19	16	10	12	20	12	16
Y:	-6	-10	-16	-14	-9	-22	-2	-5	-18
Δt:	7.9’s	8.3’s	8.5’s						
15 X:	0	-5	-8	-6	-12	-4	-2	-5	5
Y:	-22	-18	-15	-21	-20	-5	-24	-18	-8
Δt:	6.9’s	7.2’s	7.4’s						